

*New signatures on dissipation at small deformations  
from studies of fission induced by peripheral heavy-  
ion collisions at relativistic energies*

**Beatriz Jurado Apruzzese**

June 2002

# INDEX

<b>1. Introduction</b>	<b>1</b>
<b>2. Theoretical view on dissipation in nuclei</b>	<b>5</b>
2.1. Theoretical approaches to determine the magnitude of nuclear dissipation	5
2.1.1. A quantal transport theory	5
2.1.2. One-body dissipation, the wall and window formula	6
2.1.3. Dissipative diabatic dynamics	7
2.2. The Fokker-Planck equation	8
2.3. Fission as a diffusion process	9
<b>3. Review on previous experimental results on nuclear dissipation</b>	<b>15</b>
3.1. Standard observables sensitive to dissipation in fission	15
3.1.1. Even-odd structure in fission fragment yields	15
3.1.2. Kinetic energy of fission residues	15
3.1.3. Particle and $\gamma$ -ray multiplicities	17
3.1.4. Angular, mass and charge distributions	19
3.1.5. Fission and evaporation residue cross sections	19
3.1.6. The crystal blocking technique	20
3.2. Reaction mechanisms to induce fission	22
3.2.1. Fusion-fission and quasifission reactions	23
3.2.2. Antiproton annihilation	26
3.2.3. Very peripheral transfer reactions	27
3.2.4. Spallation reactions	28
<b>4. New experimental approach</b>	<b>29</b>
4.1. Peripheral heavy-ion collisions at relativistic energies	29
4.2. Experimental set-up	31

4.2.1. Set-up for fission studies in inverse kinematics	32
<b>4.3 New observables sensitive to dissipation at small deformation</b>	<b>34</b>
<b>5. Data analysis</b> <span style="float: right;">39</span>	
5.1. Total fission cross sections	39
5.1.1. Determination of the fission events	39
5.1.1.1. The fragmentation background	40
5.1.1.2. Number of fission events	45
5.1.2. Corrections applied to the total fission cross sections	46
5.1.2.1. Losses of projectiles due to the beam attenuation inside the target	47
5.1.2.2. Contribution to fission from secondary reactions inside the target	48
5.1.2.3. Losses of fission fragments due to central collisions	49
5.1.3. Results	50
5.2. Partial fission cross sections	52
5.2.1. Charge calibration	52
5.2.2. Secondary reactions	54
5.2.3. Results	57
5.3. Width of the charge distribution of the fission fragments	60
<b>6. Interpretation of the experimental results</b> <span style="float: right;">63</span>	
6.1. The Abrasion-Ablation model	63
6.1.1. Abrasion stage	63
6.1.2. Simultaneous break-up	64
6.1.3 Ablation stage	64
6.2. Modelling of the effects of dissipation in fission	65
6.2.1. Critical view on the exponential like in-growth function	65
6.2.2 New analytical description for $\Gamma_f(t)$	69
6.3. Comparison of the experimental data with model calculations	72
6.4. Discussion	77

<b>7. Conclusion</b>	<b>83</b>
<b>Appendix: Treatment of fission as a dissipative process in ABRABLA</b>	<b>85</b>
A.1. Description of $\Gamma_f(t)$ by a step function	86
A.2. Description of $\Gamma_f(t)$ by an exponential in-growth function	87
A.3. Description of $\Gamma_f(t)$ by the analytical solution of the FPE for a parabolic nuclear potential	87
<b>Resumen</b>	<b>89</b>
<b>Bibliography</b>	<b>97</b>
<b>Acknowledgements</b>	<b>105</b>

# Chapter 1: Introduction

In their transition-state model, Bohr and Wheeler [BoW39] described the fission competition in the deexcitation process of an excited heavy nucleus according to a purely statistical point of view where the evolution of the system is exclusively ruled by phase-space considerations. However, it was found by different groups in the 80's [GaB81, HiH81] that measured pre-scission neutron multiplicities were much larger than the transition-state model predictions. This discrepancy was interpreted as an indication that the deexcitation process of a highly excited heavy nucleus requires a dynamical description where the system needs time to populate the available phase space and reach equilibrium. A dynamical description of the deexcitation process in terms of a purely microscopic theory is not possible to the present day due to the large number of degrees of freedom involved. For this reason, most of the current theoretical models are transport theories [Wei80] that try to portray the process using a small number of variables. In these theories one distinguishes between collective or macroscopic and intrinsic or microscopic degrees of freedom, and the latter are not considered in detail but in some average sense as a heat bath. The collective degrees of freedom of the nucleus correspond to the coordinate motion of part or all the nucleons, e.g. vibrations, rotations and all kind of deformations. The intrinsic degrees of freedom are the individual states of the nucleons. Here, one is faced with a self-consistency problem since the collective degrees of freedom are "made up" of the individual nucleons. The fundamental idea underlying the concept of dissipation is that the collective degrees of freedom and the heat bath are coupled, that is, excitation energy can be transferred between them. The process of transfer of energy between the collective degrees of freedom and the heat bath is denominated dissipation. Dissipation is quantified by the reduced dissipation coefficient  $\beta$ , which is defined by the equation:

$$\frac{dE_{coll}}{dt} = \beta [E_{coll}^{eq} - E_{coll}] \quad (1.1)$$

where  $E_{coll}$  is the average excitation energy in the collective degree of freedom at a given time  $t$  and  $E_{coll}^{eq}$  is the average excitation energy of the collective degree of freedom at thermal equilibrium. From equation (1.1) it follows that the reduced dissipation coefficient measures the relative rate with which the excitation energy of the collective degree of freedom changes. Since  $\beta$  is a positive quantity, if  $E_{coll}^{eq} > E_{coll}$  then  $dE_{coll}/dt > 0$ , meaning that the excitation energy is transferred from the heat bath to the collective degree of freedom. Here, the time evolution of the excitation energy of the collective degree of freedom is given by an exponential-like in-growth from the initial value  $E_{coll}(t_0)$  to the value at equilibrium. On the other hand, if  $E_{coll}^{eq} < E_{coll}$  then  $dE_{coll}/dt < 0$  and the excitation energy is transferred from the collective degree of freedom to the heat bath. In this case, the solution of the differential equation (1.1) is an exponential decay from the initial value  $E_{coll}(t_0)$  to the equilibrium value. In both cases, the time constant is the inverse of  $\beta$ . Thus, dissipation rules the relaxation of the collective degrees of freedom.

According to a semi-classical picture, the time evolution of a collective degree of freedom is described by the appropriate equation of motion where the reduced dissipation coefficient appears as a parameter. In an ideal situation the experimentalist would then compare the

measured trajectory of the selected degree of freedom with the predicted one and from this infer the value of the dissipation coefficient. However, in reality it is not possible to obtain such straight information experimentally because it is not possible to directly follow the evolution of the collective degree of freedom. Instead, the experimentalist has to keep track of the “finger prints” left by the collective degree of freedom on the way to equilibrium. With this information and an appropriate theoretical model, the trajectory of the collective degree of freedom can be reconstructed.

The fission process represents the clearest example of large-scale collective motion. For this reason, theoreticians and experimentalists based their dissipation studies on the investigation of the collective degrees of freedom that describe the fission process. Intense work has been performed during the last three decades to understand the process of dissipation in nuclei. Nonetheless, the current theories on dissipation give rather contradictory results [HiG94]. The predicted magnitude for dissipation varies drastically from one theory to the other, as well as its dependence with deformation. Regarding the temperature dependence of the reduced dissipation coefficient, the divergence between the various theories is even more evident. While the formalism based on the linear response theory [Hof97] predicts an increase of the reduced dissipation coefficient  $\beta$  with the temperature, the model of Nörenberg [Nör81] predicts a decrease of the dissipation coefficient with temperature and the one-body dissipation mechanism [BIB78] a constant behaviour. A similar controversial situation is found from the experimental side [HiR92]. In our opinion, this is due to the existence of a large number of side effects that increase the complexity of the models required for the interpretation of the experimental observables and to the difficulty for determining additional observables sensitive to dissipation. Moreover, one should be cautious when contrasting the different results because there might be cases where the outcomes obtained from different techniques are not comparable. Nevertheless, according to recent experimental results, a certain agreement in terms of the deformation dependence of  $\beta$  seems to emerge. It has been found that dissipation increases on the way to the scission configuration. Strong dissipative effects have been observed within the large-deformation regime from the saddle point to scission [HiH92, VeM99, KaN01], while in the small-deformation regime from the ground state to the saddle point the effects of dissipation are rather weaker. However, in the small-deformation regime the concrete magnitude of the dissipation effects is rather uncertain. Some works point to clear effects [DiS01, BeA02], whereas others observe no deviation from the transition-state model predictions [HuB00, Dio01].

The aim of this work is to put some light in the knowledge of dissipation in this small-deformation regime. Our contribution has different aspects. We introduce an experimental approach to induce fission based on peripheral heavy-ion collisions at relativistic energies. This method leads to very specific and well-defined initial conditions of the fissioning nucleus, namely, small shape distortion and low angular momentum [Joi97]. Under these conditions, the theoretical description of the process can be considerably simplified, and the relevant information can be better extracted. In addition, this experimental approach induces very high excitation energies. This condition is necessary since, in the small deformation regime, the dynamical delay introduced by dissipation is expected to be very short. Thus, the statistical decay of the nucleus has to be very fast in order to observe the effects of the dynamical time. The use of an experimental set-up especially conceived for fission studies in inverse kinematics allowed us to introduce two new observables sensitive to dissipation at small deformations, the fission cross sections as a function of the fissioning element and the widths of the charge distributions of the fission fragments. The equation of motion that we use to reconstruct the evolution of the fission collective degree of freedom is the Fokker-Planck equation [Ris89]. Grangé and Weidenmüller

[GrJ83] solved numerically this equation for a fissioning nucleus with similar initial conditions as the ones induced by our experimental approach. The result was a time-dependent fission decay width. We have made special efforts in understanding what is the influence of widely used approximate formulations for this fission decay width on the deduced value of the reduced dissipation coefficient.

This work is organized as follows. In chapter 2 the main features of several theoretical models devoted to determine the magnitude of the reduced dissipation coefficient  $\beta$  are illustrated. In addition, the physical concepts underlying the Fokker-Planck equation are described. Chapter 3 shows the most relevant experimental techniques applied up to now to the investigation of dissipation and reports on recent results. The new experimental approach introduced in this work is described in chapter 4. A detailed description of the analysis of the experimental data to derive the observables sensitive to dissipation can be found in chapter 5. Finally, the comparison of the experimental data with a nuclear reaction code is discussed in chapter 6.



# Chapter 2: Theoretical view on dissipation in nuclei

As was mentioned in the introduction, a full microscopic theory that describes the dynamic of heavy nuclei does not exist up to now. A first step in this direction is the time-dependent Hartree-Fock method [RiS80, KeK76] with inclusion of two-body residual interaction. In the frame of a microscopic theory, the concept of dissipation is not needed. This concept appears in mixed theories where a set of collective coordinates is introduced that interact with the heat bath constituted by the microscopic coordinates. There exist a whole spectrum of these mixed or transport theories, see for example the review article accomplished by Weidenmüller [Wei80]. We have selected three examples of these theories whose main features are briefly explained in section 2.1. The quantitative results on the reduced dissipation coefficient  $\beta$  that these theories deliver are also discussed. Provided the magnitude of the dissipation coefficient is known, the evolution of the nuclear collective degrees of freedom is well understood in terms of the evolution of a collective variable in the field of a stochastic force. Such process is described by the Langevin and Fokker-Planck equations. These ideas are explained in section 2.2. The application of the Fokker-Planck equation to describe the fission process is treated in section 2.3.

## 2.1. Theoretical approaches to determine the magnitude of nuclear dissipation

There exist several theories from which the magnitude of the reduced dissipation coefficient can be derived. In this section we will illustrate briefly the main considerations of three of these theories. As we will see, no agreement is found between them neither in the magnitude of the reduced dissipation coefficient  $\beta$  nor in its deformation or temperature dependence. In the view of this strong controversy, the need of clear experimental information becomes more evident.

### 2.1.1. A quantal transport theory

Hofmann and co-workers [Hof97, Hof98, Hof01] extended the pioneering transport theory for large-scale collective motion of Kramers (see section 2.3) into the quantum regime. As in Kramers picture, this model assumes that the time needed for the collective degree of freedom to experience remarkable changes is much larger than the time needed for the nucleonic degrees of freedom to relax. This allows performing numerical calculations within the linear response theory and the locally harmonic approximation. The latter means that the residual part of the Hamiltonian is supposed to be proportional to the variation of the collective degree of freedom. Thus, the evolution of the collective degree of freedom in phase space is derived considering macroscopically small time intervals in which the nuclear potential as a function of the collective degree of freedom is approximated by a parabola. Consequently, for each time step the collective degree of freedom follows the equation of motion:

$$M \frac{d^2x}{dt^2} + \eta \frac{dx}{dt} + Cx(t) = 0 \quad (2.1)$$

where  $x=X-X_0$  measures the deviation of the collective variable  $X$  from some fixed value  $X_0$  and the quantities  $M$ ,  $\eta$  and  $C$  are the transport coefficients of inertia, friction and stiffness, respectively.

This theoretical approach permits one to calculate the transport coefficients as a function of the deformation and the temperature. The authors of this model stress the importance of the variation of the inertia  $M$  with the deformation and the temperature, which is generally disregarded in other works. Moreover, in the overdamped regime (see section 2.3) the inertia does not affect anymore the evolution of the collective degree of freedom.

Due to the complexity of this method most of the computations have been done for particular nuclei. As shown in reference [Hof98], for the nucleus  $^{224}\text{Th}$  this model predicts a rather soft dependence of the reduced dissipation coefficient with the deformation, especially for temperatures larger than 1 MeV. However, in reference [Hoi01] more generic expressions that can be extended to a wider class of nuclear systems are suggested for the temperature dependence of the transport coefficients. The following approximation for the dependence of the reduced dissipation coefficient  $\beta=\eta/M$  with the temperature is proposed:

$$\beta(T) \approx \frac{0.6 \cdot T^2}{1 + T^2/40} \quad (2.2)$$

with  $T$  in MeV and  $\beta$  in units of MeV/h. Thus this formalism predicts a rather strong increase of the reduced dissipation coefficient with the temperature. We will see later that it is a big challenge to deduce any information of the temperature dependence of  $\beta$  from experimental results.

### 2.1.2. One-body dissipation, the wall and window formula

Among the different theoretical formalisms, the one described in this section represents the more phenomenological side. In a cold nucleus the number of interacting nucleons decreases and consequently, the mean free path of the nucleons increases. In the case of a system of non-interacting nucleons, dissipation is explained by means of the one-body mechanism, that is, by the interaction of the nucleons with a moving wall that represents the nuclear potential. This is the basic physical idea of the “piston model” of Gross [Gro75]. The concept of one-body dissipation also includes the collective energy transfer caused by the difference of the velocity distributions of two nuclei in contact. Analytical expressions for the rate of energy exchange [BLB78] between the nucleons and moving walls in this long mean free-path regime exist for two limiting cases. The wall formula that describes dissipation in a mononucleus and the window formula that is suited for a dinuclear shape with a neck. These two formulas are qualitatively explained in the following lines.

The energy dissipated into the nucleon heat bath by a surface or nuclear wall moving with a normal velocity  $\dot{n}$  is given by

$$\left( \frac{dE}{dt} \right)_{\text{wall}} = k_s \rho_m \bar{v} \oint dS (\dot{n} - D)^2 \quad (2.3)$$

where  $\rho_m$  is the mass density of nucleons,  $\bar{v}=3/4v_F$  is the mean velocity of the nucleons in a Fermi gas,  $dS$  is the nuclear surface element,  $D$  the overall drift of the nucleon gas, and  $k_s$  is a scaling factor. The quadratic term of the effective wall velocity indicates that the transference of energy is irreversible. The full one-body dissipation corresponds to  $\beta = 22 \cdot 10^{21} \text{s}^{-1}$ , according to [HiR92]. The scaling factor  $k_s$  accounts for a general reduction of the one-body dissipation that is discussed below.

For the case of colliding ions or nascent fission fragments where a neck is formed, we can consider the system as two almost separated fragments connected by a small window. If the two systems are in relative motion, any particle passing through the window will damp the motion because of the momentum transferred between the fragments. In this case, to determine the total energy dissipated we have to add to the two wall terms a window term:

$$\left( \frac{dE}{dt} \right)_{\text{window}} = \frac{1}{4} \rho_m \bar{v} S_w (u_{\perp}^2 + 2u_{\parallel}^2) \quad (2.4)$$

where  $S_w$  is the area of the window and  $u_{\perp}$  and  $u_{\parallel}$  are the components of the velocity of the particles perpendicular and parallel to the window, respectively. Notice that, according to equations (2.3) and (2.4), dissipation is not expected to vary with temperature in the one-body dissipation regime. The central assumption in the derivation of these formulas is that the nucleons constitute a randomised gas at any time. If the particles are assumed to be strictly independent, the randomisation has to rely on the collisions of the particles with the boundary. We may expect this hypothesis to be satisfied if this boundary and its motion are sufficiently irregular. However, if the boundary is regular and symmetric, the strength of the wall formula will decrease. A scaling factor of  $k_s = 0.26$  was suggested by Nix and Sierk [NiS87] in their analysis of mean fragment kinetic energy data. In the same way, a recent work [ChP01] proposes a modified form of the wall friction. In this new formulation only the chaotic (non-periodic) trajectories, which give rise to irreversible energy transfer, contribute to the wall dissipation. The result is a strong suppression of the wall friction to  $\beta \approx 2 \cdot 10^{21} \text{s}^{-1}$  for near-spherical shapes of the nucleus. As the shape becomes more oblate and approaches the scission configuration, the friction increases. However, the full wall formula is not reached even at the scission configuration.

Quantal effects also set a limit to the applicability of the macroscopic formulas (2.3) and (2.4). In reference [AbR01] Abal et al. discuss the apparent paradox of suppression of the dissipated energy when the quantum version of the wall formula is considered. Their calculations show that this suppression disappears when the interaction of the system with the environment, for instance in the form of neutron emission, is considered.

Finally, it is interesting to remark that apart from the parameter  $k_s$ , there is still an ambiguity in the description of the transition from a mononucleus shape to a system with two walls plus a window. Some examples on the choice for this transition can be found in references [VeM99, ChP02].

### 2.1.3. Dissipative diabatic dynamics

This model was conceived to describe dissipation in heavy-ion reactions with energies typically a few MeV per nucleon above the interaction barrier. The one-body interaction is expected to be

realistic only at the initial stage of a heavy-ion collision. In subsequent stages of the reaction the temperature increases and the mean free path of the nucleons becomes much shorter than the size of the nucleus. In such situation the damping of the collective motion is dominated by the (two-body) interactions between the nucleons.

According to dissipative diabatic dynamics (DDD) [Nör83], energy dissipation is the result of diabatic excitations of particles and holes and subsequent equilibration by two-body collisions. The basic ideas on which this model is based are represented in figure 2.1. In the first stage of the heavy-ion collision the two nuclei approach with the ground-state distributions for the single-particle occupation probabilities. The collective motion is directly coupled to the diabatic shift of single-particle levels. If the collective velocity is not too small, a nucleon occupying the lower level before the crossing of an unoccupied level will stay in the diabatic level and finds itself in the upper level after the crossing. Thus, a diabatic excitation of particle-hole states takes place. This will produce a repulsive force on the collective motion and kinetic energy is temporally stored. However, two-body collisions try to establish a new equilibrium distribution for the occupation probabilities destroying the diabatic part of the potential. The local equilibration via two-body collisions is time-irreversible and leads to the dissipation of the stored collective energy.

The concept of DDD has been treated analytically for an interacting Fermi gas within moving walls [Nör81]. From this study follows that in the stationary limit dissipation is proportional to  $1/T^2$  and considerably larger than the wall formula one-body dissipation. Hilscher et al. [HiR92] estimated that in this limit the corresponding value of  $\beta$  is  $40 \cdot 10^{21} \text{ s}^{-1}$  at  $T = 2.5 \text{ MeV}$ .

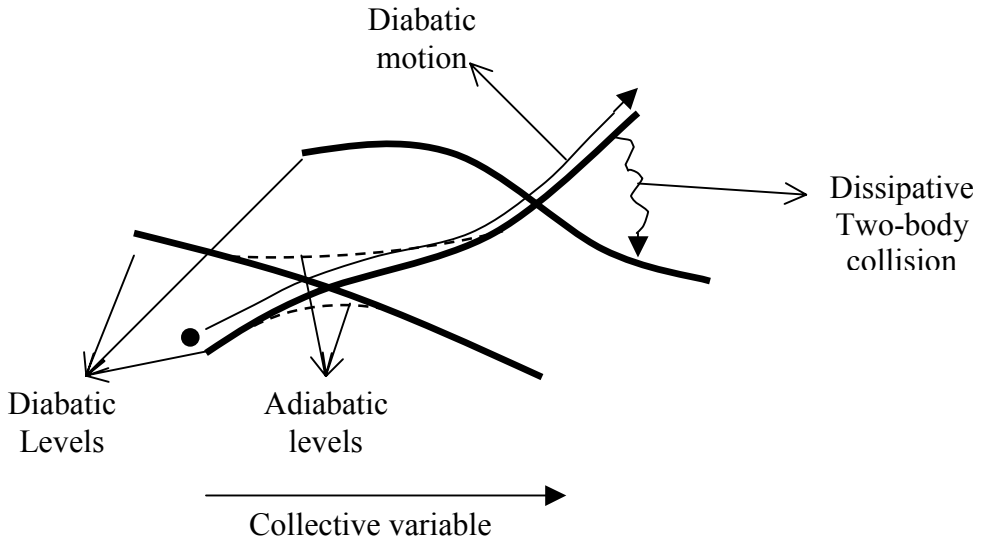


**Figure 2.1:** Schema of diabatic single-particle motion and dissipative two-body collisions as the basic elements of dissipative diabatic dynamics. The illustration was taken from reference [Nör83].

## 2.2. The Fokker-Planck equation

The Fokker-Planck equation [Ris89] (hereafter called FPE) is a powerful method for solving many problems concerning stochastic processes. It usually appears for variables describing a macroscopic but small subsystem in the field of a stochastic force. The FPE was first applied by

Fokker and Planck to describe the Brownian motion of particles. It is worthwhile to consider this process more carefully.

If a small particle of mass  $m$  moves in a fluid, its motion is determined by the collisions between the particle and the medium molecules. These collisions lead to two effects, to a damping or friction force expressed by the well known term  $-\beta v$  (Stokes' law) and to a stochastic force  $F'(t)$  that causes statistic fluctuations of the motion. Considering the more general case with an additional external force  $F$ , the equation of motion is given by the so-called Langevin equation:

$$\frac{dv}{dt} = -\beta v + \frac{F'(t)}{m} + \frac{F}{m} \quad (2.5)$$

If the mass of the particle is large so that its velocity due to thermal fluctuations in the fluid is negligible, the fluctuating force  $F'(t)$  can be disregarded and equation (2.5) transforms into a deterministic equation. However, because of the random nature of  $F'(t)$ , the equation of motion (2.5) must be treated statistically. As usually done in thermodynamics, one considers an ensemble of systems (each one formed by the particle and the fluid). Since the initial states are different for each system, the force  $F'(t)$  varies from system to system and we can only consider averages of this force for the ensemble. In the Brownian motion the average over the ensemble of the fluctuating force is zero  $\langle F'(t) \rangle = 0$  and the duration time of a collision is much smaller than the relaxation time of the velocity of the small particle given by  $(\beta)^{-1}$ . The latter implies that the time the fluid (or the heat bath) needs to recover the equilibrium after a collision is so short that the position of the particle does almost not vary in this time. In this way, the fluid is considered to be in equilibrium throughout the whole process.

One may solve equation (2.5) many times numerically with specific initial conditions at time  $t = t_0$  by generating  $F'(t)$  from a random-number generator. The result is a bundle of trajectories in phase space, all originating from the same point at  $t_0$ . Due to the statistical character of the force  $F'(t)$ , the velocity of the particle fluctuates in a stochastic way. Thus, instead of solving equation (2.5) many times, one may ask for the probability distribution  $W(v, t)$  for finding the particle in the velocity interval  $(v, v + dv)$  at a time  $t$  if at  $t_0$  the velocity of the particle was  $v_0$ . Such question can be solved applying the FPE, which is just an equation of motion for the probability distribution of fluctuating variables. This means that the Brownian motion explained by the Langevin equation (2.5) can also be described by a FPE whose variable is the probability distribution  $W(v, t)$ .

The most general form of the FPE is the FPE for N-variables:

$$\frac{\partial W}{\partial t} = \left[ - \sum_{i=1}^N \frac{\partial}{\partial x_i} D_i^1(x_1, \dots, x_N) + \sum_{i=1}^N \sum_{j=1}^N \frac{\partial^2}{\partial x_i \partial x_j} D_{ij}^2(x_1, \dots, x_N) \right] W \quad (2.6)$$

where  $D^1(x_1, \dots, x_N)$  is called the drift vector and  $D^2(x_1, \dots, x_N)$  the diffusion tensor. The diffusion term of the FPE is the result of the stochastic force  $F'(t)$ . The number of variables of the FPE and the dependence of the drift vector  $D^1$  and of the diffusion tensor  $D^2$  on the variables depends on the scenario. Usually, it is difficult to solve the FPE, in most of the cases this must be done numerically. However, we will present in section 6.2.2 a case where an analytical solution for the FPE exists.

## 2.3. Fission as a diffusion process

In order to describe the time evolution of a fission process, the shape of the nucleus is parameterised according to different variables [BrD72], for instance, the distance between the centres of the emerging fragments. These variables can be considered as nuclear collective degrees of freedom. In 1940 Kramers [Kra40] suggested describing fission as a diffusion process where one or more collective degrees of freedom behave like “a particle that moves in an external field force, but is subject to the irregular forces of a surrounding medium in temperature equilibrium (Brownian motion). The conditions are such that the particle is originally caught in a potential hole but may escape in the course of time by passing over the potential barrier.” That is, in analogy to the Brownian particle, the motion of the nuclear collective degrees of freedom is affected by the heat bath formed by the individual nucleons. The external force is given by the nuclear deformation potential. In this specific case, the corresponding Langevin equations are:

$$\begin{aligned} \frac{dv}{dt} &= -\beta v - \frac{1}{m} \frac{\partial}{\partial x} U(x) + \frac{F'(t)}{m} \\ \langle F'(t)F'(t') \rangle &= \frac{2\beta kT}{m} \delta(t-t') \end{aligned} \quad (2.7)$$

where  $U(x)$  is the nuclear potential as a function of the deformation,  $k$  is Boltzmann’s constant and  $T$  is the temperature of the heat bath. The lower part of equation (2.7) follows from the assumption that there is no correlation between the stochastic force at two different times  $t$  and  $t'$ , where the macroscopic time difference  $t_{macro} = t - t'$  is of the order of the time that the collective degree of freedom needs to change significantly. This assumption is violated if the microscopic time  $t_{micro}$  needed for the heat bath to recover the equilibrium is comparable or larger than  $t_{macro}$ . This question is of great importance and it is questionable whether the nucleus fulfils the condition  $t_{macro} \gg t_{micro}$  in all cases. In the usual terminology when this condition is satisfied the process is called Markovian. Only under the assumption [Wei80] that  $t_{macro} \gg t_{micro}$  the Langevin equations (2.7) can be transformed into a FPE. The corresponding FPE is

$$\frac{\partial W}{\partial t} = \left[ -\frac{\partial}{\partial x} v + \frac{\partial}{\partial v} \left( \beta v - \frac{1}{m} \frac{\partial}{\partial x} U(x) \right) + \frac{\beta kT}{m} \frac{\partial^2}{\partial v^2} \right] W \quad (2.8)$$

where the variable is the time-dependent probability distribution  $W(x, v, t)$  as a function of  $x$  and  $v$ . Where  $x$  is the deformation in fission direction, and  $v$  its canonically conjugate momentum divided by the mass. Kramers found that the stationary solution of equation (2.8) for a realistic nuclear potential (figure 2.2a) leads to a reduction of the fission width compared to the fission width predicted by the transition-state model of Bohr and Wheeler [BoW39] by a factor

$$K = \sqrt{1 + \gamma^2} - \gamma \quad (2.9)$$

with

$$\gamma = \frac{\beta}{2\omega_0} \quad (2.10)$$

where  $\omega_0$  is the frequency of the harmonic-oscillator potential that osculates the fission barrier at the saddle point (see figure 2.2a).

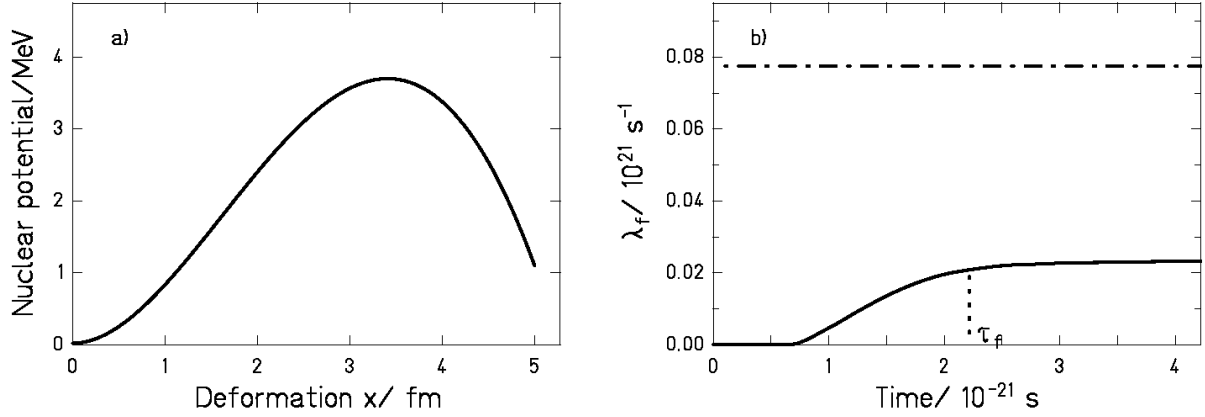


**Figure 2.2:** a) Nuclear potential as a function of the deformation. The potential is given by the expression ( $U = 8.61 \cdot 10^{-3}(x-3.41)^2 \cdot [(x-23.098)(x+1.59)] + 3.7$ ) taken from reference [BhG86]. Using the reduced mass  $A/4$  [BhG86] with  $A = 248$  leads to the ground-state frequency  $\omega_1 = 1.83 \cdot 10^{21} \text{ s}^{-1}$  in the harmonic approximation. The maximum of the potential reproduces the fission barrier with a frequency  $\omega_0 = 1.65 \cdot 10^{21} \text{ s}^{-1}$ . b) Fission rate  $\lambda_f(t) = \Gamma_f(t)/\hbar$  as a function of time. The full line was obtained from the numerical solution of the FPE [BhG86] for  $\beta = 5 \cdot 10^{21} \text{ s}^{-1}$ ,  $T = 3 \text{ MeV}$  and  $A = 248$  using the nuclear potential represent in part a).  $\tau_f$  is the corresponding transient time. The dashed-dotted line represents fission rate according to the transition-state model.

However, the success of the transition-state model prevented this idea of Kramers to establish. Approximately forty years later, experimentally observed high pre-scission neutron multiplicities [GaB81, HiH81] gave the impetus to Grangé, Jun-Qing and Weidenmüller [GrJ83] and others to theoretically investigate the influence of nuclear dissipation on the fission time scale. They solved the time-dependent FPE numerically assuming  $\beta$  to be independent of temperature and deformation, starting from a system with high intrinsic excitation energy but no excitation energy in the fission collective degree of freedom. Under such conditions, the solution of the FPE leads to a time-dependent fission decay width  $\Gamma_f(t)$  that is first suppressed, then increases and finally reaches the asymptotic value given by the Kramers factor multiplied by the Bohr and Wheeler fission width. Figure 2.2b) compares the time-dependent fission decay rate  $\lambda_f(t) = \Gamma_f(t)/\hbar$  obtained in reference [BhG86] solving numerically equation (2.8) (full line) with the transition-state fission decay rate (dashed-dotted line). The latter has been calculated dividing the stationary value that follows from the numerical calculation by the Kramers factor of equation (2.9). One sees that dissipation has not only the effect of reducing the fission rate but it also introduces transient effects, i.e., effects that occur before the stationary flow over the barrier is attained. This establishes a very important conceptual difference with respect to the transition-state model.

The time evolution of the fission width can be characterised by the transient time  $\tau_f$ , defined in [BhG86] as the time in which  $\Gamma_f(t)$  reaches 90% of the asymptotic value, see figure 2.2b). Figure 2.3a) shows three examples of the fission width in-growth function for different values of  $\beta$

calculated using the approximate solution of the FPE that will be discussed in section 6.2.2. One distinguishes between two different dissipation regimes, the underdamped regime with values of  $\beta < 2\omega_1$ , where  $\omega_1$  is the frequency that describes the curvature of the potential at the ground state, and the overdamped regime with values of  $\beta > 2\omega_1$ . The critical damping takes place for  $\beta \approx 2\omega_1$ . Figure 2.3a) depicts the fission decay-width as a function of time for these different regimes. For  $\beta = 0.5 \cdot 10^{21} \text{ s}^{-1}$  (dashed line) the fission width behaves in an oscillatory way, this is typical for an underdamped motion where the collective degree of freedom osculates several times the potential at the ground state before attaining the stationary state. The value  $\beta = 5 \cdot 10^{21} \text{ s}^{-1}$  (dashed-dotted line) belongs to the overdamped regime, the in-growth of the fission width is monotonic and its asymptotic value is considerably reduced. The case of  $\beta = 2 \cdot 10^{21} \text{ s}^{-1}$  (full line) corresponds to the critical damping. We see that within the underdamped regime  $\tau_f$  decreases with increasing  $\beta$  and that in the overdamped regime  $\tau_f$  increases with increasing  $\beta$ . This dependence can be understood recalling equation (1.1) of chapter 1. When  $\beta$  increases from zero to values below the critical damping, the transfer of excitation energy into the collective degree of freedom becomes faster and faster and so is the evolution of the collective degree of freedom in the deformation space. As  $\beta$  increases beyond  $2 \cdot 10^{21} \text{ s}^{-1}$  or so, the energy is injected very fast and the momentum of the collective degree of freedom equilibrates very rapidly. However, the drift motion in the deformation space is damped more and more effectively, increasing the time needed for the collective degree of freedom to achieve the stationary state. The critical damping represents the optimum case in which the rate of the energy transfer and the hindrance of the drift motion of the collective degree of freedom leads to the fastest possible population of the phase space and hence to the shortest transient time.

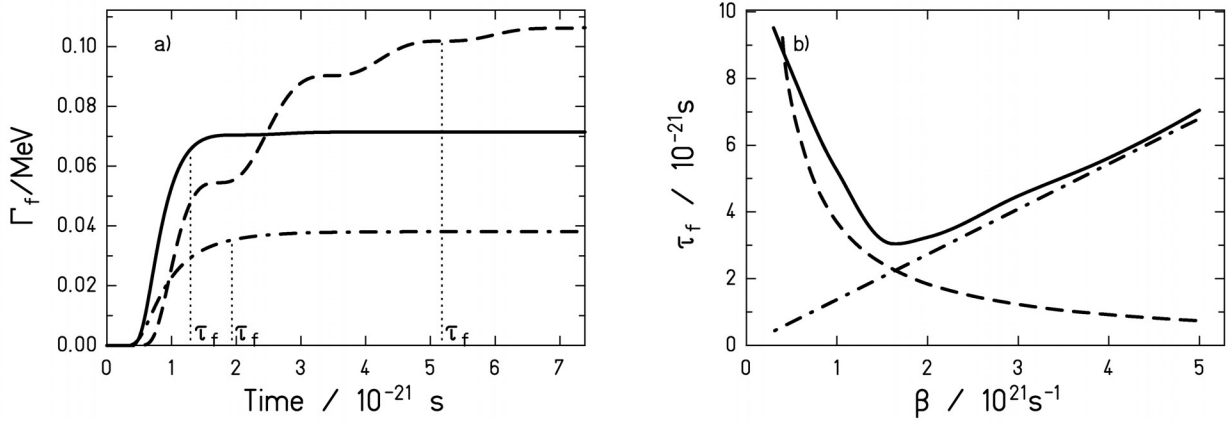


**Figure 2.3:** a) Fission decay width as a function of time for different values of  $\beta$ ,  $A = 248$  and  $T = 3 \text{ MeV}$ . The dashed line corresponds to  $\beta = 0.5 \cdot 10^{21} \text{ s}^{-1}$ , the full line to  $\beta = 2 \cdot 10^{21} \text{ s}^{-1}$  and the dashed-dotted line to  $\beta = 5 \cdot 10^{21} \text{ s}^{-1}$ . The curves result from an approximate description of the fission width that will be introduced in section 6.2.2. The corresponding transient times  $\tau_f$  are also indicated. b) Calculation taken from reference [BhG86] that represents the relation between  $\beta$  and  $\tau_f$  for a system of mass  $A = 248$  and  $T = 1 \text{ MeV}$ .

The relation between the transient time and the reduced dissipation coefficient  $\beta$  can be deduced by solving the FPE. In figure 2.3b) a calculation taken from reference [BhG86] shows this relation for a system of mass  $A = 248$  at  $T = 1 \text{ MeV}$  in comparison with two analytical

approximations that are valid in the underdamped (dashed line) and in the overdamped (dashed-dotted line) regimes. In reference [BhG86] these two approximations are given by

$$\begin{aligned}\tau_f &= \frac{1}{\beta} \ln\left(\frac{10B_f}{T}\right) && \text{for } \beta < 2\omega_x \\ \tau_f &= \frac{\beta}{2\omega_x^2} \ln\left(\frac{10B_f}{T}\right) && \text{for } \beta > 2\omega_x\end{aligned}\tag{2.11}$$

where  $B_f$  is the fission barrier,  $T$  is the nuclear temperature and  $\omega_x$  is an effective oscillator frequency<sup>1</sup> at the ground state.

---

<sup>1</sup> According to [BhG86],  $\omega_x$  is the effective harmonic oscillator frequency around the ground state for a realistic nuclear potential (see figure 2.2a). It deviates slightly from the frequency  $\omega_l$  of the harmonic approximation. Nevertheless, in literature, expression (2.11) is mostly used approximating  $\omega_x$  by  $\omega_l$ .



# **Chapter 3: Review on previous experimental results on nuclear dissipation**

Fission is a very appropriate tool for studying nuclear dissipation, because it constitutes the most glaring case of a large-scale collective motion in nuclei. In addition, the two fission fragments that result from the excitation of this collective motion represent a clear signature that allows identifying this mechanism univocally. In the last years, a large amount of experimental work based on fission reactions has been devoted to the investigation of dissipation. The aim of this chapter is to introduce the standard observables that have been analysed up to now, to discuss the characteristics of the methods applied to induce fission and to report on the main recent experimental results. This is important in order to define in which domains additional experimental information and new techniques are required. We do not intend here to cover all the existing results and to explain the differences between them, but rather to present an overview on the experimental techniques currently used to study dissipation.

## **3.1. Standard observables sensitive to dissipation in fission**

Due to the development of the experimental techniques, during the last years a large variety of experimental observables sensitive to dissipation has been introduced. In the following sections, the most important ones will be explained together with some related results.

### **3.1.1. Even-odd structure in fission fragment yields**

Dissipation at low temperatures can be investigated analysing the even-odd structure in fission-fragment yields. Due to dissipation, part of the energy released from saddle to scission ( $E^*_{\text{intrinsic}}$ ) will be transferred to the intrinsic degrees of freedom, as illustrated in figure 3.1. Consequently, if we consider a cold fissioning nucleus with an even number of protons, the existence of fission fragments with an odd number of protons indicates that part of the available kinetic energy has been dissipated to break at least one proton pair. Theoretical investigations on the nature of the dissipation process in superfluid systems are reported in references [Sch77, BoA98, KrF01].

A new theoretical description published by F. Rejmund et al. [ReI00], based on the statistical model, was used in the analysis of even-odd effects in the nuclear-charge yields of different nuclei measured in thermal-neutron induced fission and in electromagnetic-induced fission. From this study it followed that, starting from a cold system at the barrier, the fraction of the potential energy gain dissipated during the descent to the scission configuration varies from approximately 35% to 45% depending on the nuclei. In the following we will only consider experimental signatures related to dissipation in excited nuclei.

### **3.1.2. Kinetic energy of fission residues**

The measurement of the kinetic energy of the fission fragments was introduced in the 60s and 70s as one of the pioneer experimental methods to obtain information on dissipation. The kinetic energy of the fission residues is the sum of the kinetic energy that the emerging fission fragments gain through the descent from the saddle point and the potential Coulomb energy of the

fragments at scission, see figure 3.1. The potential Coulomb energy depends on the shape of the fission fragments, which is strongly affected by shell effects. However, if we consider highly excited nuclei for which the shell effects are washed out, the kinetic energy of the fission fragments is very sensitive to the energy gained by the collective motion of the composite system from saddle to scission. Depending on the strength of dissipation, a certain amount of this kinetic energy will be transferred into internal single-particle motion slowing down the collective motion and increasing the excitation energy of the fission residues. Moreover, dissipation has also an effect on the shape of the fissioning nuclei. It was discussed by Davies, Sierk and Nix in 1976 [DaS76] that the shape of the fragments depends on the mechanism assumed for the nuclear viscosity. While two-body dissipation leads to rather elongated scission configurations, one-body dissipation leads to more compact shapes.

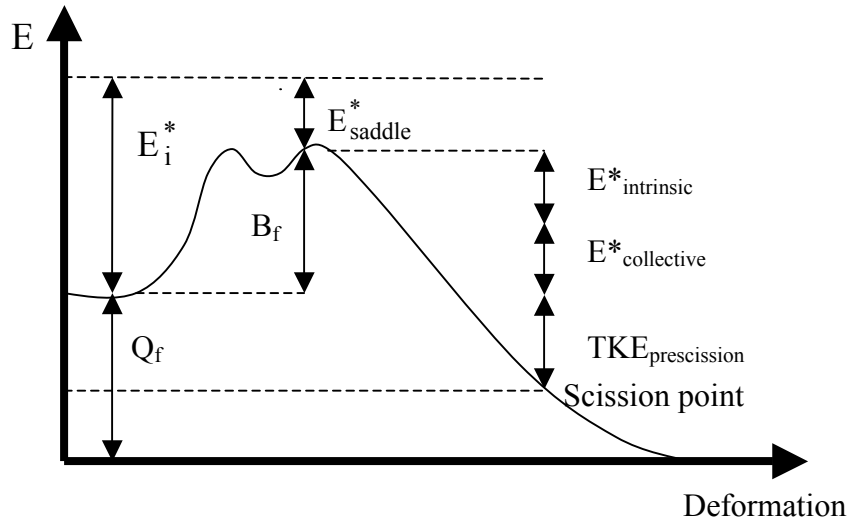


**Figure 3.1:** Schematic view of the nuclear potential energy as a function of the deformation.  $E_i^*$  is the initial excitation energy,  $Q_f$  is the  $Q$ -value associated to the fission process,  $B_f$  is the fission barrier,  $E_{\text{saddle}}^*$  is the excitation energy at saddle,  $E_{\text{intrinsic}}^*$  and  $E_{\text{collective}}^*$  are the parts of the energy gained when moving from the saddle point to the scission point that are transformed into intrinsic and collective excitation energy, respectively. Finally,  $TKE_{\text{prescission}}$  is the part of the energy gained from saddle to scission that is transformed into kinetic energy of the fission fragments.

The work of reference [DaS76] used a theoretical classical macroscopic approach with the assumption that nuclear dissipation arises from two-body collisions to interpret the experimental data. Because of the slowing down of the collective motion and the increased scission elongations, the kinetic energy of the fission fragments is expected to decrease with increasing two-body viscosity. The experimental most probable fission-fragment kinetic energies of highly excited nuclei in a mass range between  $A = 80$  and  $A = 278$  could be reproduced by a dissipation coefficient that represents 30% of the value that is required to critically damp the quadrupole oscillations of idealized heavy nuclei. Thus, according to this model, dissipation in nuclei is only moderate. However, the authors mentioned that it is not clear whether the systems studied had enough high excitation energies to apply their model. Moreover, they remarked that calculations based on one-body dissipation agreed equally well with the experimental data.

### 3.1.3. Particle and $\gamma$ -ray multiplicities

Dissipation lengthens the fission time scale, thus an additional approach to study nuclear dissipation is to measure this time. Since the early 80s suitable “nuclear clocks” based on the measurement of particle and  $\gamma$ -ray multiplicities have been developed leading to surprising new insights into fission dynamics. In fact, in 1981 different groups [GaB81, HiH81] discovered independently that pre-scission neutron multiplicities were much higher than expected from the statistical model, which revived the interest in nuclear dissipation. The measurement of neutron multiplicities prior to scission (neutron clock) and the measurement of GDR (Giant Dipole Resonance)  $\gamma$ -ray multiplicities (GDR clock) are the most applied nuclear clocks. The neutron clock and the GDR clock have been extensively described in the review articles of Hilscher and Rossner [HiR92] and Paul and Thoennessen [PaT94], respectively. Here we will just illustrate their main features.

The basic idea of the neutron clock is to measure the number of neutrons (or other light particles) evaporated prior to and post scission. The pre-scission lifetime can be deduced from the pre-scission neutron multiplicity  $M_n^{pre}$  according to the expression

$$\tau_{pre} = \sum_{i=1}^{M_n^{pre}} \tau_n^i \quad (3.1)$$

where  $\tau_n$  is the mean partial neutron evaporation time.  $\tau_n$  can be calculated using the statistical model. However, this requires a good knowledge of the ratio of the level densities of the initial and final state, which is not the case at very high excitation energies. Nevertheless, at high excitation energies one can use the post-scission neutron multiplicities to derive the pre-scission lifetime. Since the neutron emission time  $\tau_n$  decreases exponentially with the excitation energy, the emission time of the last neutron before scission determines the pre-scission lifetime. The excitation energy at the scission configuration  $E_{scission}^*$  is found as excitation energy in the separated fragments, which deexcite mainly by neutron emission. According to figure 3.1 the total excitation energy of the fission fragments after scission is,

$$E_1^* + E_2^* = E_{scission}^* + E_{deformation}^* = E_{saddle}^* + E_{intrinsic}^* + E_{collective}^* + E_{deformation}^* \quad (3.2)$$

where  $E_{saddle}^*$  is the excitation energy above the saddle point,  $E_{intrinsic}^*$  is the part of the energy gain from the saddle to the scission point that is transferred to the intrinsic degrees of freedom and  $E_{collective}^*$  [WiS76] is the part of the energy gain from the saddle to the scission point that is transferred to other collective degrees of freedom like vibrations or rotations.  $E_{deformation}^*$ <sup>2</sup> is the excitation energy that the fission fragments acquire when they snap back to their normal shape. Thus, measuring the post-scission neutron multiplicity, the excitation energy at the moment of emission of the last neutron prior to scission can be reconstructed, and the pre-scission time can

---

<sup>2</sup> The potential energy at the scission point is the sum of the coulomb interaction of the fragments and their deformation energy  $E_{deformation}^*$ . The first is transferred into kinetic energy and the second adds to the excitation energy of the fragments after separation.

be approximated by  $\tau_{pre} \approx \tau_n(E_{scission}^*)$ . Since the excitation energy at scission is low, the level densities from a well-known excitation-energy region can be employed.

The kinematical focusing is used to disentangle between pre-scission and post-scission neutrons. This feature relies on the fact that in thermal equilibrium, neutrons are evaporated isotropically in the rest frame of the emitting source. Thus, in the laboratory frame, the neutrons emitted by the compound nucleus will follow a homogeneous angular distribution, while the angular distribution of the neutrons emitted after scission will be peaked around the velocity vectors of the fission fragments. The measured pre-scission time is given by

$$\tau_{pre} = \tau_{formation} + \tau_f + \tau_{ssc} + \tau_{acceleration} \quad (3.3)$$

where  $\tau_{formation}$  is the time to form the compound nucleus,  $\tau_f$  is the time for the system to decide to fission,  $\tau_{ssc}$  is the time for the transition from saddle to scission and  $\tau_{acceleration}$  is an additional time induced by those post-scission neutrons emitted before the kinematical focussing is strong enough to disentangle them from the pre-scission neutrons. The charged-particle clock leads to larger uncertainties in the determination of reaction time scales than the neutron clock. The reason is that the measurement and interpretation of charged particle multiplicities is hindered by the low multiplicity in most reactions, the anisotropic angular distribution, which makes more difficult to apply the kinematical focussing, and the sensitivity of the decay widths to the deformation of the emitting source and to the not well defined emission barriers.

Although with a modest relative probability, high energetic  $\gamma$ -rays ( $E_\gamma \sim 5\text{-}20$  MeV) originating from the deexcitation of the giant dipole resonance (GDR) are emitted during the fission process. In analogy to the case of the pre-scission neutron multiplicities, Thoennessen et al. [ThC87] established that the GDR  $\gamma$ -ray multiplicities were around 50% larger than expected by the statistical model. They found the explanation to this phenomenon on the slowing down of the fission process caused by dissipation. The measurement of the multiplicity of the GDR  $\gamma$ -rays emitted prior to scission constitutes the basis of the GDR clock. The  $\gamma$ -ray spectrum registered results from two sources: the GDR  $\gamma$ -rays emitted from the compound nucleus before scission, and the  $\gamma$ -rays emitted from the fission fragments. Due to the dependence of the energy of the GDR  $\gamma$ -rays on the deformation and the mass of the emitting system, these two sources contribute in different ways to the spectrum. While the pre-scission GDR  $\gamma$ -rays dominate at energies from 8 to 15 MeV, the fission fragment component is the strongest at the lowest energies (statistic  $\gamma$ -rays emitted at the end of the deexcitation process) and at the highest energies ( $\gamma$ -rays resulting from the GDR). These different contributions cannot be disentangled experimentally and must be extracted by comparing with model calculations.

To transform the measured particle pre-scission and the GDR  $\gamma$ -ray multiplicities into the pre-scission lifetime, Monte-Carlo codes are used. In general, these calculations neglect  $\tau_{formation}$  and  $\tau_{acceleration}$  assuming that the equilibrium is reached very rapidly and considering only the process until the scission point is reached. In fusion-fission reactions  $\tau_{formation}$  plays a considerable role and the pre-scission time scale is affected by the increase of excitation energy that, due to dissipation, the system experiences on the way to scission. Therefore, determining the reaction times for such processes requires the use of dynamical codes. In such codes, dynamical trajectories are obtained by solving the classical equations of motion of the system, the Langevin equations, see section 2.2. They are coupled to a statistical code to account for the evaporation of particles. Incidentally, a considerable effort has been made lately in the development of

dynamical codes. For instance, a recent formulation of such description based on a three-dimensional Langevin equation is presented in reference [KaN01], and in reference [AlC01] it is investigated whether the statistical evaporation model is applicable for particle emission along quasifission trajectories. In addition, the GDR  $\gamma$ -ray multiplicity data have been analysed according to a statistical model [BuH91] in which the time-dependent fission decay width is given by an exponential in-growth function. We will explain in chapter 6 various arguments that shed severe doubts on the validity of this function to describe the time evolution of the fission decay width.

### 3.1.4. Angular, mass and charge distributions

To understand how these observables give information on the reaction time scales, it is necessary to consider the evolution of deep-inelastic collisions. A comprehensive review on these reactions can be found in reference [Sch84]. Once the repulsive Coulomb force has been overcome and the surfaces of the two nuclei come into contact, nucleons diffuse through the contact zone from one nucleus to the other in both directions. During the mass diffusion, the kinetic energy of the projectile is dissipated into thermal excitation of the nuclei. If the angular momentum is large, the nuclei do not fuse and they fly apart after exchanging some nucleons and losing kinetic energy. The mass transfer is a statistical process that increases with the time the two nuclei stay in contact. In general, there exists a strong correlation between the exchange of mass and charge between the reaction partners and the angular distribution. All these observables are sensitive to the reaction time. However, for their interpretation in terms of time scales one has to consider that they also depend strongly on the projectile-target combination and on the bombarding energy. For the cases of reactions with heavy systems, less asymmetric than the Businaro-Galone maximum, the drift towards symmetry of the mass and charge distribution of the residues from non-fusion reactions represents a proof of longer reaction times, and hence of the dissipative forces acting between the reaction partners. Normally, the anisotropy of the angular distribution decreases with increasing reaction time. For short time scales in which the system made less than one turn before separating, the angular distributions (selected for a certain fragment mass) present a typical forward-backward asymmetry. In [ShA87] the mean angle by which the dinuclear system has rotated while sticking together was used to extract the dynamical time scale of the reaction. The results were consistent with the one-body nuclear dissipation mechanism. As for the case of the neutron and charged-particle multiplicities, the correct interpretation of these signatures involves using dynamical codes. For example, Feldmeier [Fel87], applying his dynamical code HICOL, found that window dissipation could describe satisfactorily the scattering angle, mass and charge distributions of a large group of lightly damped heavy-ion collisions.

### 3.1.5. Fission and evaporation-residue cross sections

If the excited nucleus experiences a dynamical hindrance on its way to the saddle point, contrary to what is assumed by the statistical model, the fission channel will be initially closed in the deexcitation process of the system. Hence, if the particle decay time is shorter than the dynamical fission delay, the nucleus will release excitation energy evaporating particles. Due to the loss of excitation energy and to the decrease of fissility caused by the emission of light charged particles, the fission probability of the resulting system after the dynamical delay will be considerably smaller than the one of the original compound nucleus. Consequently, the fission cross sections will be reduced compared to the statistical-model predictions. Since the decay time for particle

emission decreases exponentially with increasing excitation energy, even without considering a temperature-dependent dissipation coefficient, there is a threshold excitation energy from which fission cross sections start to be sensitive to the dynamical delay. As will be shown in section 3.2, the determination of this threshold excitation energy is currently a subject of controversy. It is important to notice that fission cross sections give information on dissipation up to the saddle point, whereas pre-scission particle multiplicities and angular and mass distributions are sensitive to the whole deformation range up to the scission point.

The complementary effect to the drop of the fission probability at high excitation energies with respect to the statistical model is the increase of the evaporation-residue cross sections. Therefore, the excitation functions of the evaporation residues represent a clear signature of dissipation up to the saddle point as well. In a very recent work [HuB00, Dio01], the angular-momentum distribution of the evaporation residues has been introduced as an additional observable sensitive to dissipation inside the saddle, since the mean value of the spin distribution shifts to larger values with increasing dissipation.

Nevertheless, it should be noted that the interpretation of all these observables to deduce quantitative results on dissipation depends strongly on other parameters like the ratio of the level density parameters  $a_\beta/a_n$  and the temperature dependence of the fission barriers.

### 3.1.6. The crystal blocking technique

The crystal blocking technique [Gib75] is based on the fact that a positively charged particle that moves inside a crystal is blocked or deflected by the atoms in the crystal row or plane, hence the term crystal blocking. The angular distribution of the emerging particles will show a yield reduction in the angle corresponding to the crystal row or plane. When an excited compound nucleus is produced by a nuclear reaction between a projectile and a lattice atom, the excited nucleus recoils with a well-known velocity. If the nucleus fissions before it has a chance to move away from the original lattice location, the emerging fission fragments will be blocked by the lattice row or plane and their angular distribution will show what we will call a “prompt blocking dip”. If, however, some of the nuclei live long enough to recoil into the open space between the crystal rows or planes, the corresponding blocking dip will become shallower than the “prompt blocking dip”, see figure 3.2. Thus, contrary to the observables described up to now, the crystal blocking technique allows for a direct observation of the deviation from very fast fission decay times. This technique is only sensitive to a certain interval of the fission decay-time distribution. The lower limit is given by the time needed for the nucleus to move away from the thermal vibration of the crystal atoms. The upper limit is reached when the mean recoil distance becomes larger than the distance to the next atomic row or plane. The limits of the sensitivity interval depend on the beam energy. In the current experiments the lower limit reaches values of approximately  $10^{-19}$  s and the upper limit of  $10^{-14}$  s.

In reference [GoM99] fission decay times of reaction products close to uranium were measured at different excitation energies up to 250 MeV by applying this technique. The times found were larger than  $3 \cdot 10^{-19}$  s, one order of magnitude larger than the ones obtained from the measurement of prescission particle multiplicities for similar nuclei. In a recent work Gontchar et al. [GoM02] used a dynamical code based on the Langevin equations combined with a statistical model to interpret some of the fission times of reference [GoM99]. They calculated the scission-time distribution and compared it with the neutron emission-time distribution and with the  $\gamma$ -ray

emission-time distribution. This comparison showed that the scission-time distribution delivered by the analysis of neutron multiplicities does not include the largest scission times located in the tail of the complete distribution. In this way they explained why the scission times inferred from pre-scission neutrons are shorter than the values obtained from the blocking technique. The model calculations were also used to determine the strength of dissipation from neutron and  $\gamma$ -ray multiplicities. It resulted that the fission-time distribution and the  $\gamma$ -ray multiplicities required a reduction of the one-body dissipation given by the wall formula by a factor  $k_s \approx 0.45$ , while the neutron multiplicities needed a stronger dissipation to be reproduced.

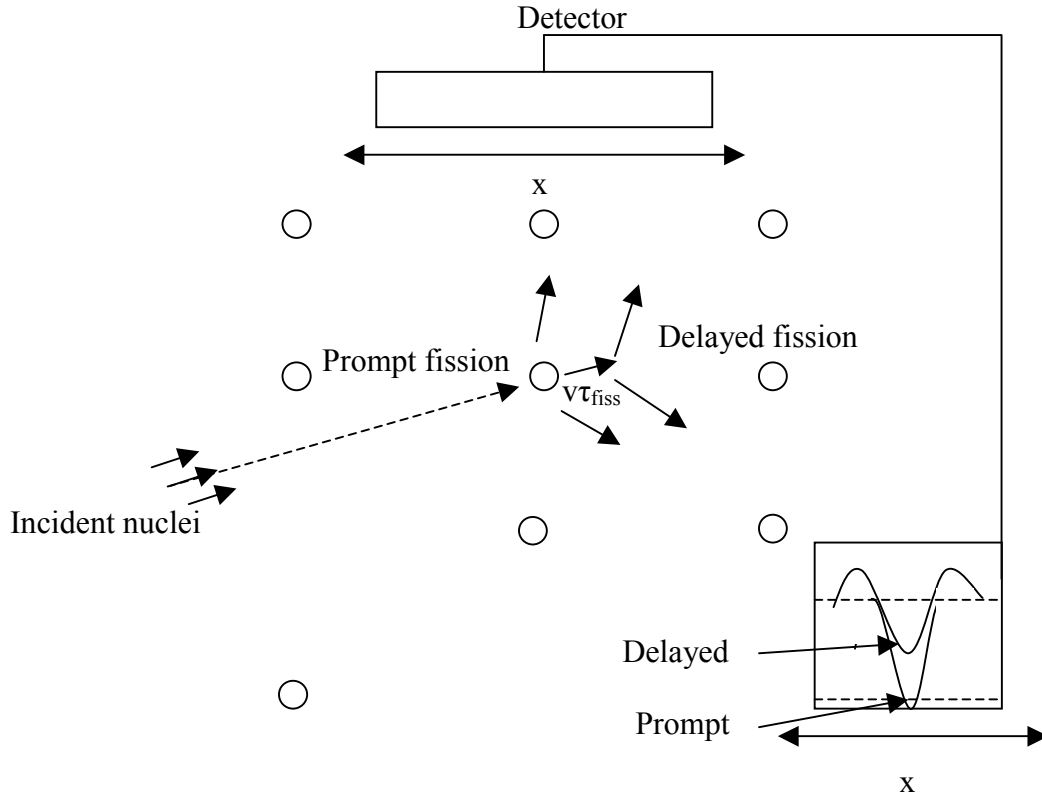


**Figure 3.2:** Schematic representation of the crystal blocking technique for determining the fission decay time  $\tau_{fiss}$ . The trajectories of the fission products where one is emitted in the direction of the lattice are schematically shown for prompt and delayed fission.

In the light of the previous paragraph, we would like to stress the fact that one should be cautious when comparing the fission time scales inferred from the various observables presented here. Let us consider first the ideal case in which the pre-scission time of individual events  $\tau_{pre}^i$  could be determined experimentally. The corresponding (linearly averaged) mean pre-scission time would then be

$$\langle \tau_{pre} \rangle_{lin} = \frac{\sum_{i=1}^N \tau_{pre}^i}{N} \quad (3.4)$$

In the case of neutron clock, the measured quantity is the (linearly averaged) mean value of the pre-scission neutron multiplicity  $\langle M_n^{pre} \rangle$ . From this magnitude the pre-scission time is derived according to equation (3.1). In order to have a more direct understanding of the relation between  $\langle M_n^{pre} \rangle$  and  $\tau_{pre}$ , we will consider the approximation discussed in section 3.1.3 where the pre-scission time is derived from the mean neutron decay time of the last neutron emitted  $\tau_n^{last}$ . According to the statistical model the mean neutron decay time is given by

$$\tau_n = \frac{\hbar^3 \pi}{2m_n R^2 T_r^2} \frac{\rho(E)}{\rho_r(E - S_n)} \quad (3.5)$$

where  $\rho(E)$  is the level density of the compound nucleus,  $S_n$  is the neutron separation energy,  $m_n$  is the neutron mass,  $R$  is the nucleus radius,  $\rho_r(E)$  is the level density of the daughter nucleus after neutron emission and  $T_r$  is the temperature of the daughter nucleus after neutron emission. Thus, for the mean decay time of the last neutron we have

$$\tau_n^{last} \approx \frac{\hbar^3 \pi}{2m_n R^2 T_r^2} \frac{(E^* - \langle M_n \rangle \cdot S_n)^{5/4}}{(E^* - (\langle M_n \rangle - 1) \cdot S_n)^{5/4}} \frac{\exp\left[2\sqrt{a(E^* - (\langle M_n \rangle - 1) \cdot S_n)}\right]}{\exp\left[2\sqrt{a(E^* - \langle M_n \rangle \cdot S_n)}\right]} \quad (3.6)$$

where we have used the expression for the level density that follows from the Fermi model, with  $a$  the level density parameter and  $E^*$  the initial excitation energy. Equation (3.6) shows that the time that follows directly from the mean pre-scission neutron multiplicity is not the mean pre-scission time defined in equation (3.4). To calculate a mean pre-scission time from the measurement of pre-scission neutron multiplicities it is necessary to average over a complicated function (equation 3.6) of the measured mean multiplicity. These ideas can be also expressed by means of the following generic expression. If the quantity  $y$  is a function  $f$  of another quantity  $x$

$$\langle y \rangle = \langle f(x) \rangle \neq f(\langle x \rangle) \quad (3.7)$$

In the same way, there exists a relation between the parameters of the measured blocking pattern and the pre-scission time that has to be considered when averaging. Moreover, the largest fission decay times to which the blocking technique is sensitive might be related to fissioning nuclei with very low excitation energies. In such cases, the statistical decay time is anyhow very long and thus, one is not sensitive to an increase of the dynamical fission time due to dissipation. When averaging over the pre-scission times obtained applying the blocking technique, all the events that do not lead to a deviation from the “prompt blocking dip” should be included. If this is not done and the mean pre-scission time is derived from averaging among the long-term tail of the fission decay-time distribution, the resulting pre-scission time and the pre-scission time that follows from the neutron clock should not be comparable.

## 3.2. Reaction mechanisms to induce fission

One way of classifying the various experimental approaches dedicated to dissipation studies is by considering the mechanism used to produce the excited system. The reaction mechanism determines the excitation energy, deformation and angular momentum of the fissioning system.

These magnitudes have to be considered correctly in the theoretical description of the fission process because they significantly influence any conclusion on dissipation. In this section the most important reaction mechanisms will be illustrated together with some recent results.

### 3.2.1. Fusion-fission, fast fission and quasifission reactions

The majority of the experimental approaches dedicated to the study of dissipation are based on nucleus-nucleus collisions at energies that range from 5 A MeV to about 100 A MeV. The evolution of such reactions for the largest impact parameters has already been explained in section 3.1.4. As the impact parameter decreases, the contact time of the two systems increases and so does the dissipated kinetic energy. For the smallest impact parameters, that is, for the largest mass diffusion, the entire total kinetic energy with respect to the centre of mass is transformed into excitation energy. Among the nucleus-nucleus collisions leading to fission, one distinguishes between fusion-fission, fast fission and quasifission reactions.

Fusion-fission reactions are characterized by the formation of a compound nucleus. The compound nucleus, in the definition used in the present work, is a stage of thermal equilibrium of all intrinsic and collective degrees of freedom. This means that, except for the excitation energy and the angular momentum induced, its subsequent decay is independent of how it was formed. Fusion-fission reactions are characterized by a symmetric mass distribution of the fission fragments. The angular distribution is described by the probability distribution of the  $K$  quantum number<sup>3</sup> as explained by Vandenbosch and Huizenga in reference [VaH73]. In the case of fusion-fission reactions the angular distribution for the particles and fission fragments is of  $1/\sin\theta$ -type but relatively attenuated at  $0^\circ$  and  $180^\circ$ .

In fast fission and quasifission reactions, the full equilibration is not acquired. Although there is a considerable mass transfer and the kinetic energy is completely dissipated, the contact of the projectile and target nuclei is not followed by compound-nucleus formation inside the saddle point. Thus, there is some residual memory of the entrance channel. In the case of fast fission the compound nucleus is not formed because there is no fission barrier. In quasifission, even though there exists a fission barrier, there is no compound-nucleus formation because after overcoming the fusion barrier of the entrance potential, the composite system adopts directly the saddle configuration and is not kept in the fission potential well. Due to the strong statistical fluctuations, both types of reactions are characterized by fragment mass distributions wider than the mass distributions resulting from fusion-fission reactions. Besides, the composite systems formed do not last long enough to evolve to configurations different than the  $K = 0$  configuration and the angular distributions are more peaked at the extremes  $0^\circ$  and  $180^\circ$  than in the case of fusion-fission reactions.

As was already mentioned in section 3.1, the interpretation of the experimental observables related to such reactions requires the use of elaborated dynamical codes that describe the complete evolution of the composite system along the dynamical trajectory. Moreover, to give reliable results such codes have to deal with the large angular momenta of the composite system and to include the effects of fluctuations around the mean trajectory.

---

<sup>3</sup>  $K$  is the projection of the angular momentum onto the symmetry axis of the fissioning nucleus.

In 1992 Hilscher and Rossner [HiR92] compiled the most important results on fission dynamics paying special attention to fusion-fission and quasifission reactions. Their investigations showed already rather controversial results. In the following, we proceed to report on the most recent results obtained from investigating this type of reaction mechanism. In reference [FrG93] Fröbrich, Gontchar and Mavlitov analysed the pre-scission neutron multiplicities and fission probabilities as a function of the excitation energy for several systems covering a broad range of fissilities. They interpreted the experimental data by means of a dynamical code based on the one-dimensional, overdamped Langevin equation coupled to a statistical code. In order to describe all the different reactions with a universal coefficient  $\beta$ , they introduced the following deformation dependence:  $\beta = 2 \cdot 10^{21} \text{ s}^{-1}$  until the necking of the fissioning nuclei starts to set in and a linear increase with deformation for the rest of the process. They interpreted this dependence as an evidence for two-body viscosity in the range of the compact shapes and the onset of one-body dissipation for the more deformed ones. Later [FGo93], the same model was successfully applied to reproduce the pre-scission neutron and charged-particle multiplicities, the GDR  $\gamma$ -ray multiplicities, the evaporation-residue and the fission cross sections of the reaction  $^{16}\text{O} + ^{208}\text{Pb}$  at different excitation energies. It was observed that  $\gamma$ -multiplicities and evaporation-residue cross sections clearly disagreed with an alternative description proposed by R. Butsch et al. [BuH91] to explain the same reaction where  $\beta$  was independent of the deformation and equal to  $20 \cdot 10^{21} \text{ s}^{-1}$ .

Wilczynski et al. [WiS96] applied the dynamical code HICOL [Fed87] coupled to a statistical cascade code to interpret the pre-scission neutron multiplicities emitted along several fast-fission trajectories. In the initial part of the reactions, the one-body dissipation expressed by the wall-and-window formula (section 2.1.2) was reduced by a factor  $k_s^{\text{in}} \leq 0.5$  until the formation of the composite system. From the mononucleus shape to scission, the one-body dissipation had to be increased drastically by factors that range from  $k_s^{\text{out}} = 4$  to  $k_s^{\text{out}} = 12$  depending on the reaction. The decrease of the dissipation coefficient as a function of the calculated temperature at the outgoing part of the trajectories was interpreted as the onset of two-body dissipation at a nuclear temperature of about 2 MeV. Nevertheless, in reference [VeM99] the fission-fragment mass and angular distributions of one of the previous reactions were measured at two different energies and analysed with HICOL coupled to a different evaporation code. In contrast to reference [WiS96], here the full wall-and-window formula was used with a smooth transition from the two walls plus window formula to the monowall formula. The mass and angular distributions were consistent with the one-body dissipation, and the analysis led to reaction times of  $(15\text{-}16) \cdot 10^{-21} \text{ s}$  in good agreement with the results obtained from the analysis of the neutron multiplicities performed by Hinde et al. [HiH92] for the same reaction. Consequently, in [VeM99] the onset of two-body dissipation supported by Wilczynski et al. was not confirmed for nuclear temperatures smaller than 2.5 MeV. It is interesting to notice that Hinde and co-workers [HiH92, HiB99] studied similar fusion-fission reactions using non-dynamical codes. In their models, the suppression of the fission channel for a fixed time of the order of  $(20\text{-}30) \cdot 10^{-21} \text{ s}$  accounted for dissipation effects.

Karpov et al. [KaN01] compared three-dimensional Langevin calculations with mass-kinetic-energy distributions and neutron multiplicities of several fusion-fission reactions. They used the dissipation tensor that results from the wall-window formula. The calculations agreed well with the experimental data when the contribution to the dissipation from the wall term was reduced by a factor  $k_s$  that varied from 0.25 to 0.5, depending on the reaction. Finally, in a very recent publication [ChP02] the chaos-weighted wall formula, a modified form of the wall friction introduced by the same authors in a previous reference [ChP01] (see section 2.1.2), has been applied to a dynamical description in the framework of the one-dimensional Langevin equation

coupled with a statistical evaporation code. The reduced dissipation coefficient  $\beta$  that follows from the chaos-weighted wall formula is about 10 times smaller than the value of  $\beta$  that results from the original wall formula. Pre-scission neutron multiplicities and fission probabilities of a number of compound nuclei formed in heavy-ion induced fusion reactions could be much better reproduced with the chaos-weighted wall formula than with the normal wall formula. Their calculations showed that for the compound nuclei  $^{178}\text{W}$ ,  $^{188}\text{Pt}$ ,  $^{200}\text{Pb}$ ,  $^{213}\text{Fr}$ , and  $^{224}\text{Th}$ , the pre-saddle neutrons account for most of the pre-scission neutrons at low excitation energies. However, for very heavy nuclei as  $^{251}\text{Es}$  they found that the majority of the pre-scission neutrons is emitted in the post-saddle stage. Their calculations could not reproduce the experimental pre-scission neutron multiplicity for this case. They suggested that one of the possible explanations for this discrepancy is a considerable increase of the dissipation in the post-saddle region.

An important set of results has been gained from applying the GDR clock to fusion-fission and quasifission reactions. In reference [ThB93] the threshold excitation energy from which the statistical model failed to reproduce a large amount of excitation functions of particle and  $\gamma$ -ray multiplicities was investigated. It was found that the ratio of the threshold temperature and the temperature-dependent fission barrier was independent of the mass of the fissioning nucleus and equal to 0.26. The authors suggested that this could reflect an onset of dissipation with increasing temperature. However, in [PlB95] this systematic behaviour was explained without any assumption of an onset of dissipation effects or temperature dependence. This work showed that the reason why the statistical model fails to reproduce the experimental data for  $T_{\text{threshold}}/B_f > 0.26$  is because at this point the dynamical delay time starts to be larger than the decay time predicted by the statistical model. Hofman, Back and Paul [HoB95] even found an analytical expression for the temperature dependence of dissipation from the study of the GDR multiplicities associated with several fusion-fission and quasifission reactions. According to this dependence,  $\gamma$ , defined as the ratio  $\beta/2\omega_0$ , is about 0.2 for temperatures smaller than 1.17 MeV, while for larger temperatures, both, a linear dependence with  $T$  and with  $T^2$  reproduced well the experimental data. An independent work [SoH98] based on the study of the yields and velocity distributions of heavy residues and fission fragments from the reaction of  $^{197}\text{Au}$  at 20 MeV on carbon and aluminium targets led to dissipation values consistent with the temperature dependence pointed out in [HoB95]. The most recent works concerning the study of GDR multiplicities in fusion-fission and quasifission reactions, though, were interpreted assuming a deformation dependence of dissipation instead of a temperature dependence. For instance, in [ShD00] a value of  $\gamma = 2$  inside the saddle point and of  $\gamma = 10$  outside the saddle point was required to reproduce the GDR multiplicity emitted in the fission process of  $^{240}\text{Cf}$ . Diószegi et al. [DiS01] found that the GDR multiplicities of the reaction  $^{19}\text{F} + ^{181}\text{Ta}$  at 161 and 181 MeV were not enough to determine the dissipation coefficient unambiguously. They used the evaporation-residue cross sections of the same reaction to determine the dissipation up to the saddle point,  $\gamma_{\text{saddle}} = 3$ . Fixing this value of the dissipation coefficient up to the saddle deformation, they varied the dissipation coefficient from saddle to scission to reproduce the gamma-multiplicities obtaining  $\gamma_{\text{scission}} = 10$ . Such deformation dependence with very low values of dissipation for the compact shapes up to saddle is compatible with the examination of the angular-momentum distribution of the evaporation residues presented in [HuB00, Dio01]. For the latter case, the experimental data could be reproduced using the code CASCADE without any dissipation.

Further results have also been obtained by studying  $\alpha$ -induced fission. This method was used in [EmM96] to investigate fission of Pu isotopes produced in the reaction of  $^{238}\text{U} + \alpha$  with  $E_\alpha = 37$  and 43 MeV. At low excitation energies, the double-humped structure of the fission barrier

causes an additional delay. This delay is related to the dynamical trajectories that are trapped in the second well. The probability that the system follows such trajectories is influenced by dissipation. The study of reference [EmM96] was based on the analysis of the fission-fragment angular distributions, which are a superposition of the distribution related to the inner and to the outer barrier. The FPE was used to calculate the time-dependent probability of finding the system at the second saddle. This probability was introduced into a statistical code that led to  $\beta = 0.25 \cdot 10^{21} \text{ s}^{-1}$  for the reaction at 37 MeV and  $\beta = 0.35 \cdot 10^{21} \text{ s}^{-1}$  for  $E_\alpha = 43 \text{ MeV}$ . These results were interpreted as a signature of the increase of dissipation with temperature. Fission induced by  $\alpha$ -particles has been extensively investigated by Moretto and co-workers. In reference [MoJ95] fission excitation functions for different compound nuclei from  $A = 186\text{--}213$  with excitation energies of about 25 to 125 MeV were investigated in terms of the transition-state model with the fission width suppressed for a fixed transient time  $\tau_f$ . The agreement with the model was very good and no effects of transient times longer than  $3 \cdot 10^{-20} \text{ s}$  were visible. In a more recent work [JiP01], the upper limit of the transient time could be further constrained to  $\tau_f < 25 \cdot 10^{-21} \text{ s}$  for excitation energies up to 150 MeV, and the most probable value was found to be  $\tau_f = 10 \cdot 10^{-21} \text{ s}$ .

### 3.2.2. Antiproton annihilation

Antiproton annihilation is an alternative mechanism to induce fission where the characteristics of the fissioning nucleus coincide with the assumptions of the model of Grangé and Weidenmüller [GrJ83] described in section 2.3. The absorption of antiprotons by nuclei has several stages. In the first stage the antiproton annihilates with a single nucleon of the surface or inside the nucleus. The main annihilation channel leads to the production of a pion cloud containing an average of about 5 particles. Depending on the energy of the incident antiproton this cloud is more or less focused forward into the nucleus. The interaction of the pion cloud with the nucleus can be described by intranuclear cascade (INC) calculations. The cascades of sequential two-body collisions lead to a certain number of holes and excited nucleons. These calculations predict that the angular momentum remains low ( $l < 25 \hbar$ ) and that shape distortion and density compression are negligible in contrast to what occurs for heavy-ion induced fusion-fission and quasifission reactions. Additionally, the time for achievement of thermal equilibrium is of the order of  $10^{-22} \text{ s}$ , much shorter than the corresponding time for fusion-fission and quasifission reactions. In [GoB96] a new experimental method to determine the thermal excitation energy produced with energetic antiprotons was introduced. It was based on the measurement of the neutrons and charged particles (fission fragments, intermediate mass fragments, and light-charged particles) emitted in the deexcitation process of several target nuclei. The relation between the light-particle multiplicities and the excitation energy was inferred by the statistical code GEMINI [ChM88]. For the case of an uranium target, the absolute differential cross section  $d\sigma/dE^*$  obtained by this method results in more than 12% of the reaction cross section leading to excitation energies larger than 600 MeV, with the tail of the distribution (approximately 1% of the reaction cross section) reaching up to energies close to 1 GeV (see figure 4.2 of chapter 4). However, it is worthwhile to remark that in antiproton annihilation reactions we have to consider the effect of fluctuations in the measurement of the excitation energy in combination with a production cross section, which is steeply decreasing for the highest excitation energies (figure 4.2 of chapter 4). In our opinion, this implies the danger that events of a selected apparent high excitation energy are strongly "contaminated" by a part of the more abundant processes of smaller true excitation energies.

Fission of different nuclei induced by stopped antiprotons was firstly analysed considering dissipative effects according to the FPE in references [HoI94, KiI96]. Although the mass, velocity and momentum distributions, and the correlations between these magnitudes could be quite well reproduced with this model, it is difficult to extract any conclusion on dissipation from these investigations. Later in [ScE97], the neutron multiplicities produced in the antiproton-induced fission reaction of  $^{238}\text{U}$  at different excitation energies were analysed according to the statistical model including some modifications related to dissipation. The data could be either reproduced by including the Kramers factor (equation (2.9) of chapter 2) with  $\gamma = 0.7$  or assuming a saddle-to-scission delay time  $\tau_{ssc}$  of  $10^{-20}\text{s}$ . In a recent publication [LoG01], the fission probabilities for  $\bar{p}$  (1.22 GeV) + Au and U as a function of the excitation energy were determined. They were analysed according to two different model calculations. The calculations combining INC and the statistical code GEMINI [ChM88] that assumes a fixed transient time independent of the temperature and the fission barrier led to an upper limit of the transient time  $\tau_f$  of  $1 \cdot 10^{-21}\text{s}$ . The calculations performed with INC and ABLA [GaS91, JuJ98] led to a reduced dissipation coefficient  $\beta \approx 2 \cdot 10^{21}\text{s}^{-1}$ .

### 3.2.3. Very peripheral transfer reactions

This section is dedicated to a very interesting experiment based on a transfer-fission reaction where the fission events originating from excited systems that fulfilled the conditions of Grangé and Weidenmüller's model [GrJ83] were filtered and analysed. In this experiment [EcK90] the fission probabilities of very peripheral  $^{40}\text{Ar} + ^{232}\text{Th}$  collisions at 30 A MeV were measured. From the measured linear-momentum transfer, the average initial excitation energy and the angular momentum of the compound nuclei formed were deduced. The linear-momentum transfer was determined from the fission-fragment folding angles. An average value for the charge of the nucleus right before the start of the evaporation cascade could be deduced from the charge of the projectile-like fragments and the emitted light charged particles measured in coincidence with the fission fragments. For this it was assumed that the light charged particles either were of preequilibrium nature or emitted by the projectile-like fragments. In this way, the initial average values of the charge, excitation energy and angular momentum of the system after the collision could be inferred. Within the narrow range of impact parameters they selected, the average charge of the excited nucleus varied from 88.5 to 88.7, the average excitation energy from 49 to 219 MeV and the average angular momentum from 14 to  $55\ \hbar$ . Because of the large impact parameters selected, the deformation of the excited nuclei after the collision was very close to the ground-state deformation. It is worth to notice how, by selecting very large impact parameters, the characteristics of the excited nucleus (except for the excitation energies) produced in a transfer reaction could be as favourable as in the case of antiproton annihilation. The experimental fission probabilities were compared with the statistical code HIVAP [ReH85] with  $1.05 \leq a_f/a_n \leq 1.09$ . The transient time  $\tau_f$  was deduced in the following way. Firstly, the fission probability was set artificially to zero and the different steps of the neutron cascade were calculated. Then, for the particular conditions (excitation energy, angular momentum, etc.) of the different steps of these sequences, the fission probabilities were calculated. The so determined fission probabilities decrease along the evaporation paths until they cross the range of experimental values. The excitation energy  $E^*_{Threshold}$  (or better the range of excitation energies) where this occurs was interpreted as the threshold excitation energy where the transient time and the statistical decay time become comparable. Thus,  $\tau_f \approx \tau_n(E^*_{Threshold})$ , where  $\tau_n$  is the mean neutron decay time. The authors remarked that the results are very much dependent on the choice

of  $a_f/a_n$ . Nevertheless, the existence of a transient time  $\tau > 1 \cdot 10^{-21} \text{ s}$  and  $E^*_{Threshold} \sim 120 \text{ MeV}$  followed from their work independently of these considerations.

### 3.2.4. Spallation reactions

Spallation or proton-induced fission represents an additional mechanism that leads to excited nuclei with the characteristics of the model of Grangé and Weidenmüller [GrJ83]. The reaction in inverse kinematics of a  $^{197}\text{Au}$  beam at 800 A MeV on a proton target was studied at GSI. In reference [BeA02] signatures of fission dynamics were extracted from the analysis of the properties of the fission fragments resulting from this reaction. The nuclear charge, mass and velocity of one of the fission products could be determined by means of the projectile-fragment separator FRS [GeA92]. With this information, the characteristics of the fissioning system at saddle could be reconstructed. From the velocity and the charge of the fission fragment the charge distribution of the fissioning nucleus was inferred. It resulted to be very narrow with a most probable value of  $Z_{fiss} = 76.5 \pm 0.5$ . The mass number of the fissioning nucleus was obtained assuming a symmetric mass distribution of the fission fragments and correcting for post-scission neutron emission, the value found was  $A_{fiss} = 180 \pm 2$ . This work introduces a very interesting observable, namely, the width of the charge distribution of the fission residues. In the next chapter it will be explained how this quantity is directly related to the excitation energy of the fissioning nucleus at saddle. Their analysis led to an excitation energy over the saddle of  $E^*_{saddle} \approx 110 \pm 20 \text{ MeV}$ . A nuclear-reaction code consisting of an intra-nuclear cascade [CuV97] linked to the evaporation code ABLA [GaS91, JuJ98] was used to interpret the measured quantities and to infer the initial characteristics of the excited system. The measured excitation energy at saddle was considerably lower than the initial calculated one, evidencing a clear suppression of the fission channel at high excitation energies. Calculations based on the transition-state model could not reproduce the whole set of observables independently of the value used for the parameter  $a_f/a_n$ . Only with the inclusion of dissipation by means of a time-dependent fission width approximated by a step function and  $a_f/a_n = 1.05$ , better agreement with the data was found. With a value of  $\beta$  between 2 and  $3 \cdot 10^{21} \text{ s}^{-1}$  the total fission cross sections, the isotopic distributions of the fission residues as well as the characteristics of the fissioning nucleus at saddle could be explained very satisfactorily.

# Chapter 4: New experimental approach

In the previous chapters we have seen that, in spite of the experimental and theoretical efforts, the value of the reduced dissipation coefficient and, more exactly, its variation with deformation and temperature is still subject of debate. From the experimental side, several work [PlB95, DiS01] have already remarked the difficulty of finding experimental signatures sensitive to the temperature dependence of dissipation. With regard to the deformation dependence, for the large-deformation regime clear signatures of dissipation have been found, whereas for the deformation regime from the ground-state to the saddle the situation is rather uncertain. While some studies find clear effects with  $\beta = 4 \cdot 10^{21} \text{ s}^{-1}$  [ShD00] and  $\beta = 6 \cdot 10^{21} \text{ s}^{-1}$  [DiS01], other work point to weak effects  $\tau_f \approx 10 \cdot 10^{21} \text{ s}$  [JiP01],  $\tau_f < 1 \cdot 10^{21} \text{ s}$  [LoG01],  $\beta = 2 \cdot 10^{21} \text{ s}^{-1}$  [BeA02] or to no dissipation effects at all [HuB00, Dio01]. To improve this situation, new observables sensitive to dissipation in this deformation regime should be introduced and alternative mechanisms to induce fission are needed. Heavy-ion induced fusion-fission reactions have proven to be very successful in the large deformation scale, but they do not offer optimum conditions for extracting the relevant information at small deformations. These reactions cannot be analysed with the model of Grangé and Weidenmüller [GrJ83] because the initial conditions of the composite system formed after the collision do not correspond to those assumed in this model. As mentioned in the previous chapter, such reactions require elaborate dynamical models that have to take into account all the additional side effects that influence the fission process. Furthermore, since the transient time is expected to be a tiny effect, the excitation energy of the nucleus should be high enough for the statistical decay time to be shorter than the transient time. Thus, an experimental approach is required that produces highly-excited heavy nuclei with high cross sections. Concerning the observables, the analysis of particle multiplicities gives information on dissipation on the whole path from the ground state to scission but it does not allow to explore the deformation range from the ground state to the saddle point independently. Total fission or evaporation-residue cross sections are the most used observables to investigate dissipation at low deformation. However, we will see in chapter 6 that these observables are not sufficient to face questions like the temperature dependence of dissipation or the effects that the theoretical description of the process has on the deduced dissipation coefficient. In this chapter we will introduce an experimental method based on peripheral heavy-ion collisions at relativistic energies that represents ideal conditions for investigating dissipation at small deformations. An experimental set-up optimal for fission studies, which is illustrated in section 4.2, allowed to measure the total fission cross sections of a  $^{238}\text{U}$  beam at 1 A GeV on different targets and to establish two additional experimental observables sensitive to dissipation at small deformations, they will be introduced in section 4.3.

## 4.1. Peripheral heavy-ion collisions at relativistic energies

The ideal scenario for the investigation of dissipation at small deformations is one where the heavy nucleus produced meets the conditions of the theoretical work of reference [GrJ83]. This means that the nucleus should be highly excited with only little shape distortion. In addition, the angular momentum induced should be small in order to avoid additional influence on the fission process. Such well-defined initial conditions considerably simplify the theoretical treatment of the process because, provided the nuclear potential as a function of the deformation is well known, the evolution of the system up to the saddle point is quantitatively described by the FPE.

These specific initial conditions can be achieved by applying a projectile-fragmentation reaction, i.e. a very peripheral nuclear collision with relativistic heavy ions. The evolution of such reactions follows three main stages: First the collision takes place leading to a prefragment, then thermal equilibrium in the intrinsic degrees of freedom is established and finally, this equilibrated system decays by particle emission or fission. A scheme of the different stages is shown in figure 4.1.

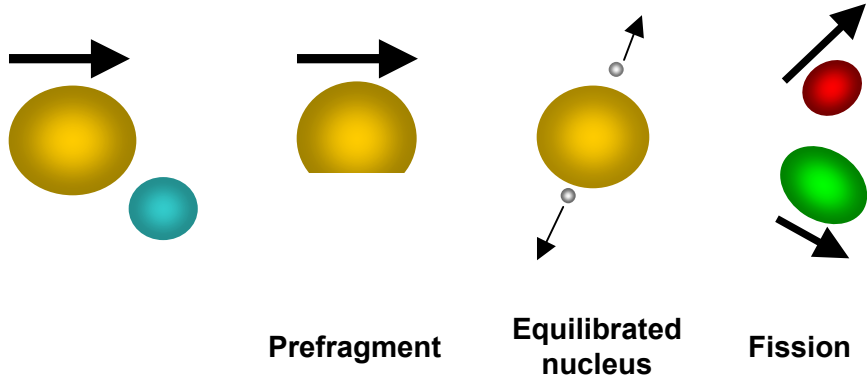


**Figure 4.1:** Scheme of the different stages of a very peripheral heavy-ion collision at relativistic energies that leads to fission.

The characteristics of the prefragment can be well described by the geometrical abrasion model [GaS91, ScB93], which is explained in chapter 6. Nuclear collisions at bombarding energies well above the Fermi energy can be considered as quasi-free nucleon-nucleon collisions. Hence, a peripheral collision of the relativistic heavy projectile with the target essentially removes a number of nucleons from the projectile respectively target nucleus. The shape of the prefragment is almost not distorted, the root mean squared value of the angular-momentum distribution of the prefragment varies from 10 to 20  $\hbar$  (as shown by numerical calculations [Joi97]) and its excitation energy is given by the number of nucleons abraded. It has been found experimentally [ScB93] that on the average 27 MeV excitation energy pro nucleon abraded are induced. As discussed in section 3.2, similar initial conditions can be reached by relativistic proton-nucleus collisions in inverse kinematics [BeA02] and by the annihilation of antiprotons [GoB96, HoI94] at the nuclear surface. However, a comparison between model calculations based on the intranuclear cascade [BoC02] and the abrasion model [GaS91, ScB93] show that, if the same fissioning nucleus is produced by means of both reaction mechanisms, the angular momentum induced by proton reactions is approximately three times larger than the angular momentum induced by peripheral fragmentation reactions. In addition, our approach populates higher excitation energies more strongly than proton or antiproton-induced reactions. This is shown in figure 4.2 for the case of antiproton reactions, where the experimental differential total reaction cross section  $d\sigma/dE^*$  for the reaction  $\bar{p}(1.2 \text{ GeV}) + {}^{238}\text{U}$  taken from reference [GoB96] is compared with a calculation according to the abrasion model for the fragmentation reaction of  ${}^{238}\text{U}(1 \text{ GeV}) + \text{Pb}$ . This picture shows that fragmentation reactions can lead to very high excitation energies. Recent experimental results [ScR02] indicate that if temperatures above approximately 5 MeV are reached, thermal instabilities set in eventually leading to multifragmentation. This means that instead of equilibrating directly after the fragmentation reaction, the system undergoes a simultaneous break-up. This phenomenon is considered as well in the theoretical model used to interpret these reactions and it is discussed in chapter 6. As can be seen in figure 4.2, while the reaction cross section induced by antiproton annihilation starts to

decay steeply at excitation energies of about 500 MeV, this range of energies remains strongly populated by fragmentation reactions. This is of great advantage not only because it enables observing the effects of the dynamical delay induced by dissipation and analysing a possible temperature dependence, but also because it allows investigating the interplay between dissipation and thermal instabilities in the inhibition of fission at high excitation energies.

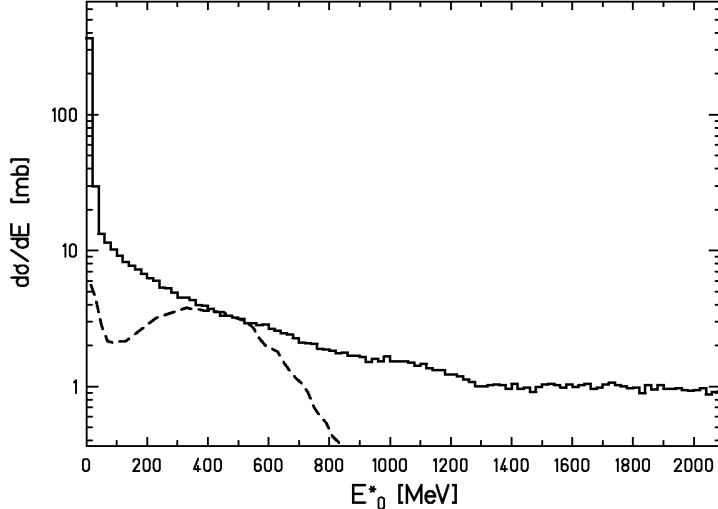


**Figure 4.2:** Total reaction cross section as a function of the excitation energy induced right after the collision. The dashed line corresponds to the reaction  $\bar{p}$  (1.2 GeV) +  $^{238}\text{U}$  measured in reference [GoB96], and the full line is a calculation performed with the abrasion model [GaS91, ScB93] for the reaction  $^{238}\text{U}$  (1 A GeV) + Pb.

## 4.2. Experimental set-up

For investigating the reactions described in the previous section, a beam of relativistic heavy ions is needed. This is possible at GSI where the heavy-ion synchrotron SIS delivers an intense  $^{238}\text{U}$  beam at 1 A GeV. In our measurements the experimental set-up for fragmentation-fission studies was located behind the FRS. Although the FRS is a high-precision magnetic spectrometer [GeA92], for the present experiment it was solely used as a beam line to guide the  $^{238}\text{U}$  primary beam to the set-up. The FRS consists of two parts with two dipoles each, see figure 4.3. The ions passing through the dipoles of each part are deflected according to their velocity and the ratio of their mass  $A$  and their ionic charge  $q$ :

$$B\rho = \frac{\beta\gamma mc}{qe} = 3.107 \frac{\beta\gamma A}{q} [Tm] \quad (4.1)$$

where  $B\rho$  is the magnetic rigidity,  $\beta=v/c$ ,  $\gamma=(1-\beta^2)^{-1/2}$  are the relativistic factors,  $c$  is the speed of light in vacuum,  $m = A \cdot u$  is the mass at rest and  $e$  is the electron charge. During our experiment, the magnetic fields of the dipoles were chosen to centre the trajectories of the  $^{238}\text{U}$  fully stripped projectile ions. A Nb-foil at the entrance of the FRS was used to fully strip the  $^{238}\text{U}$  projectiles. This was necessary to prepare a well-defined beam, since the projectiles leaving the SIS with  $q = +73$  were only partly stripped by the thin vacuum window located at the exit of the SIS.

However, the interaction of the primary uranium beam with the different layers of matter positioned on the way to the experimental set-up (SIS vacuum window, SEETRAM foils, dummy target and niobium-foil in front of the FRS, scintillator plate and Nb-foil at the second focal plane S2) led to contaminants with different charge stages and different masses than the required primary beam of  $^{238}\text{U}^{92+}$ . Since these contaminants have different  $B\rho$  than the primary beam, they arrived to the focal planes of the spectrometer S2 and S4 with different positions. Two scintillation detectors located at these focal planes allowed for measuring the position of the ions after traversing the pair of dipoles. Figure 4.4 shows how combining the position of the nuclei at the fourth focal plane S4 with their position at the second focal plane S2, it was possible to disentangle the primary uranium beam from the rest of contaminants.

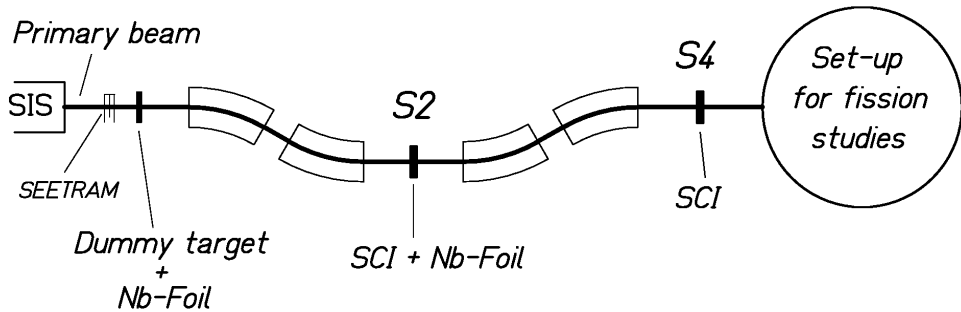


**Figure 4.3:** Schematic view of the FRS as used in this experiment.

The window depicted in figure 4.4 selects the primary beam. The three peaks situated to the left of the beam peak at the same height are the products of neutron-removal reactions. The peak located at a position at S2 of approximattely -25 mm corresponds to  $^{237}\text{U}^{92+}$ , the peak found at about -60 mm to  $^{236}\text{U}^{92+}$  and the one at around -85 mm to  $^{235}\text{U}^{92+}$ . The intense peak below the primary beam corresponds to those nuclei that capture one electron when traversing the layers of matter positioned at S2. The peaks to the left of this peak found at positions at S2 of approximately -25 and -60 mm correspond to the products  $^{237}\text{U}^{91+}$  and  $^{236}\text{U}^{91+}$ , respectively.

#### 4.2.1. Set-up for fission studies in inverse kinematics

After passing through the FRS, the primary beam reached the experimental set-up schematically illustrated in figure 4.5. This set-up, especially designed for fission studies in inverse kinematics, consisted of a scintillation detector, two MULTiple-Sampling Ionisation Chambers (MUSICs), a double ionisation chamber and a time-of-flight wall. The first scintillation detector had several functions. It supplied the horizontal position at the exit of the FRS, it provided the start signal for the time-of-flight measurement and it served as a trigger. The target was located in between the two MUSICs. This configuration worked as an active target. The double IC recorded the energy-loss signals of both fission fragments separately. Finally, the time-of-flight wall provided the stop signal for the time-of-flight measurement of the fission fragments. This set-up was a modified version of a previous one [ScS00] that was conceived to study electromagnetic-induced fission in a lead target. The even-odd structure [ReI00] of the charge yields of the fission fragments measured in this experiment was used to study dissipation in cold nuclei, see section 3.1.1. In the present case, we wanted to focus our investigations on dissipation at higher excitation energies. Therefore, we optimised the set-up for investigating nuclear-induced fission in different targets.

In the previous experiment, a subdivided scintillation detector, mounted in front of the double IC, served as a fast trigger to reduce the load of the data acquisition. In the present measurement, this detector was removed to avoid the effects caused by the secondary reactions of the fission fragments when passing through it.

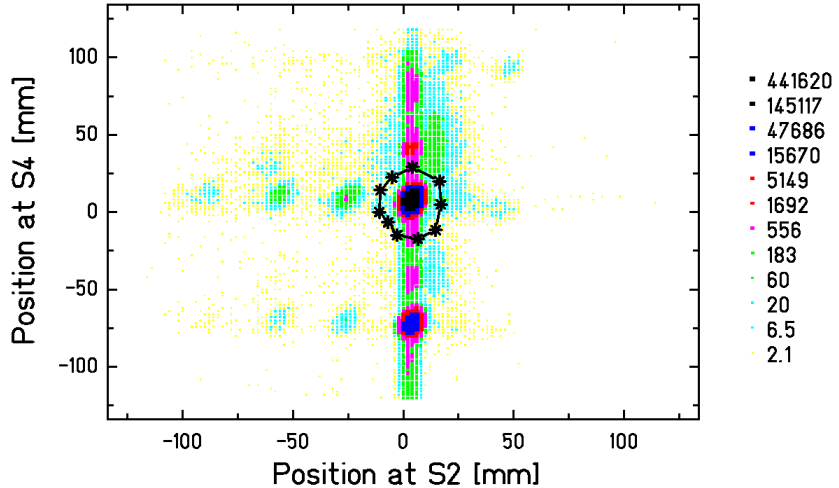


**Figure 4.4:** Position at the last focal plane of the FRS (S4) versus position at the intermediate focal plane (S2). The window selects the primary beam. The other peaks correspond to contaminants that result from neutron-removal and electron-capture reactions in the layers of matter located between the SIS and the experimental set-up for fission studies. The numbers indicate the scale of the cluster plot.

As will be shown in the next chapter, the experimental observables that we analysed were determined by means of the MUSICs and the double IC. A schematic upper view of a MUSIC is shown in figure 4.6a). The four anodes positioned at the side of the chamber allowed for a multiple measurement of the energy deposition and the drift time of the induced signals. The active depth of the chamber was 40 cm. The width of 20.4 cm was large enough to cover the complete angular distribution of the fission fragments that populated a cone of several tens of mrad. The active volume was filled with P10, a mixture of 90% argon and 10% methane. The cathode was subject to a potential of  $-4000\text{V}$  and the anodes to 650 V. To restrict the position dependence of the induced signals and the effects of the signals induced by the gas ions, a Frisch-grid at zero voltage was placed 2.3 cm in front of the anodes.

The double ionisation chamber was conceived according to the kinematics of fission residues in inverse kinematics. It consisted of two independent counting-gas volumes separated horizontally. In this way, the measurement of energy loss of both fission fragments could be performed independently. The active volume of the chamber was 80 cm long, 40 cm high and 60 cm wide, and was filled with the counting gas P10. At a height of 20 cm, the active volume was divided in two parts by the cathode. Two groups of four anodes were situated on the top and the bottom of the chamber at opposite sides of the cathode. The anodes were connected to a voltage of 1000 V and the cathode to  $-4000\text{ V}$ . Two Frisch-grids at zero voltage were placed 2 cm in front of the anodes. A schematic side view of the double IC is depicted in figure 4.6b). The common cathode was located at the height of the beam axis to ensure that each fission residue was detected in a different part of the chamber. Moreover, with such geometry, the slow gas ions generated by the

intense non-fissioning projectiles were absorbed very fast by the cathode, and recombination losses could be avoided. However, due to the vertical emittance of the primary beam and an eventual shift of the cathode with respect to the mean vertical position of the beam, there was a certain probability that both fission fragments passed through the same half of the double IC. Additionally, fission fragments moving very close to the cathode had less active volume to ionise and produced less electron-ion pairs. This caused additional losses. Overall, the detection efficiency of the double IC was approximately 90%. In the next chapter it will be described how the combined information from the double IC and MUSIC 2 allowed for reducing considerably these losses leading to a detection efficiency of approximately 97%.

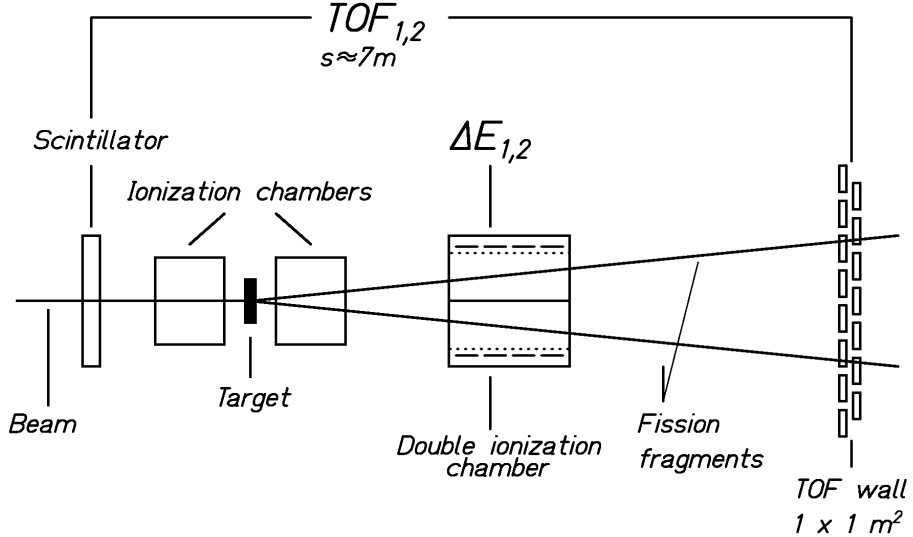


**Figure 4.5:** Experimental set-up for fission studies in inverse kinematics placed after the FRS.

As discussed in [Bad73, PfG94, Mül96], the resolution of the energy-loss signals in the ionisation chambers can be considerably improved by suppressing the contribution of the highly energetic  $\delta$ -electrons. This was performed filtering the lower frequencies of the energy-loss signal with a proper shaping time in the main amplifiers, 0.5  $\mu$ s in the MUSICs and 1  $\mu$ s in the double IC.

### 4.3. New observables sensitive to dissipation at small deformation

At relativistic energies, the velocity of the fission fragments is close to the velocity of the projectile. In the velocity range of the present experiment, the energy deposition is almost independent of the velocity. Therefore, since the fission residues are fully stripped, the energy loss is directly related to the square of the atomic number Z. This feature was already used in reference [GrC85] to determine charge-changing cross sections and total fission cross sections. The experimental set-up described in the previous section allowed for measuring the energy-loss signals of the two fission products resulting from the interaction of the  $^{238}\text{U}$  relativistic beam with different targets. With this information it was possible to extract the total fission cross sections as a function of the target mass. The target has an influence on the mass and the excitation energy of the residues produced directly after the collision. Consequently, dissipation might affect differently the number of systems that fission for each target combination. Furthermore, due to the charge identification of both fission fragments, we could determine two additional

observables: the partial fission cross sections, that is, the cross section as a function of the fissioning element, and the charge distributions of the fission fragments that result from a given fissioning nucleus. The next chapter explains in detail how these three observables have been determined. In chapter 3 we have already elucidated why total fission cross sections are sensitive to dissipation. In this section it will be qualitatively illustrated why the partial fission cross sections and the widths of the charge distributions represent two new observables, sensitive to the strength of the dissipation coefficient at small deformation.

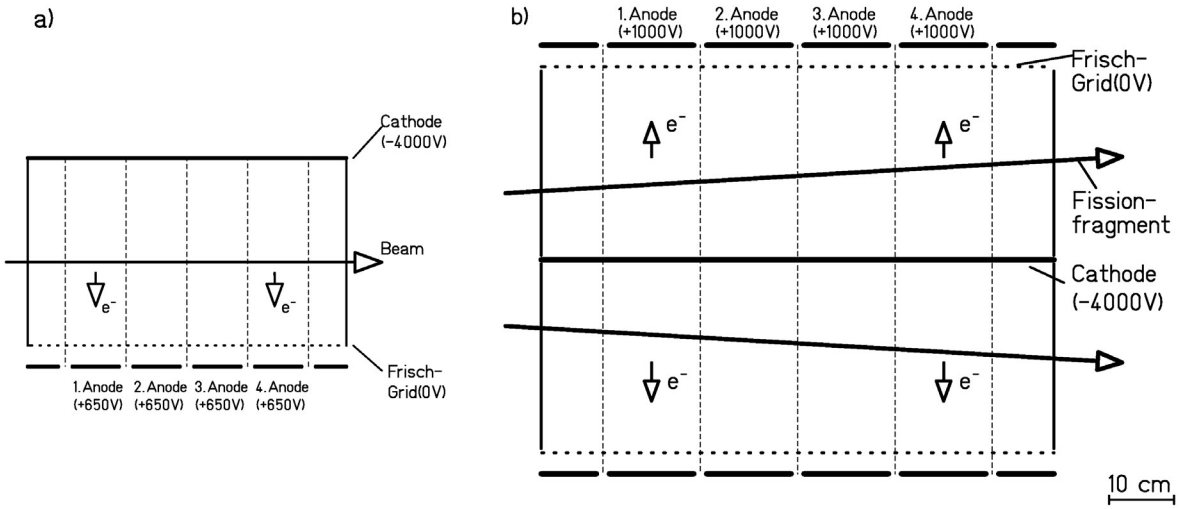


**Figure 4.6:** a) Schematic upper view of the active volume of the MUSIC. b) Schematic side view of the active volume of the double IC.

The double IC allows for determining the sum of the nuclear charges of the fission residues  $Z_1+Z_2$ . The fission fragments are neutron rich and their excitation energy is too low for emitting protons after scission. Therefore, the sum of the charges of the two fission fragments is a very significative magnitude because it gives the charge of the fissioning nucleus. Although there might be few charged particles emitted after the abrasion, the charge of the fissioning element goes linearly with the charge of the prefragment and hence, it gives an indication of the centrality of the collision. Low values of  $Z_1+Z_2$  imply small impact parameters and large excitation energies induced by the abrasion process. If the excitation energy of the nucleus is higher than the threshold excitation energy at which the statistical decay time and the transient time  $\tau_f$  become comparable, fission competition is delayed with respect to particle evaporation by the transient time. Therefore, for the lightest fissioning nuclei (lowest values of  $Z_1+Z_2$ ) the existence of a transient time would imply a considerable reduction of the fission probability (and hence of the fission cross section) compared to the predictions of the transition-state model.

We have shown in section 3.2.4 that the width of the charge distribution of the fission fragments was used in reference [BeA02] to determine the temperature of the fissioning system at saddle. This relation between the width of the charge distribution and the saddle point temperature  $T_{\text{saddle}}$  relies on an empirical systematic behaviour between the variance of the mass distribution  $\sigma_A^2$  and  $T_{\text{saddle}}$  that reads

$$\sigma_A^2 = \frac{T_{\text{saddle}}}{C_A} \quad (4.2)$$

where  $C_A$  is a constant that depends on the fissility  $Z^2/A$  of the fissioning nucleus. Due to the strong correlation between the charge distribution of the fission fragments and the mass distribution, a linear relation between  $\sigma_A^2$  and the temperature at saddle directly implies a linear relation between  $\sigma_Z^2$  and  $T_{\text{saddle}}$ . Thus, for the lower values of  $Z_1+Z_2$ , i.e., for the lighter fissioning nuclei where the initial excitation energy is larger than the threshold excitation energy, the nucleus will evaporate particles while it deforms, and the temperature at saddle  $T_{\text{saddle}}$  will be smaller than the initial temperature. Consequently, the corresponding charge distributions will be narrower than the ones predicted by the transition-state model. The quantity  $C_Z$  that connects  $\sigma_Z^2$  with  $T_{\text{saddle}}$  is related with  $C_A$  as follows

$$C_Z = \frac{A_{\text{fiss}}^2}{Z_{\text{fiss}}^2} \cdot C_A \quad (4.3)$$

where  $A_{\text{fiss}}$  and  $Z_{\text{fiss}}$  represent the mass and the nuclear charge of the fissioning nucleus, respectively.

Rusanov et al. [Rus97] analysed the experimental mass-energy distributions of fragments produced in the fission of various nuclei with fissilities  $Z^2/A \geq 32$  and excitation energies between 40 and 150 MeV. This study revealed a considerable enhancement of the variances  $\sigma_A^2$  with the angular momentum. The relation between  $C_A$  and the fissility parameter was intensively studied. In a later work [Mus98], the experimental mass distributions of the fission products of proton- and alpha-induced reactions were investigated. By means of a fitting procedure, the values of the parameter  $C_A$  for nuclei within a range of fissilities  $Z^2/A$  from about 28 to 44 and excitation energies from approximately 5 to 25 MeV were determined. Including the data for larger fissilities of reference [Rus97] corrected for angular-momentum effects, a parameterisation of the relation between  $C_A$  and the fissility was presented.

According to the transition-state model the constant  $C_A$  is proportional to the stiffness of the liquid-drop potential at the saddle point respect to mass-asymmetric changes. In the frame of the transition-state model the mass yields  $Y(A)$  follow the expression

$$Y(A) \propto \exp\left[2\sqrt{a_f(E^* - B_f(A))}\right] \quad (4.4)$$

where  $A$  is the mass of the fragments,  $a_f$  is the level density parameter at saddle and  $E^*$  is the excitation energy of the fissioning nucleus. The conditional fission barrier  $B_f(A)$  corresponding to the mass  $A$  can be described by the liquid-drop model including shell effects

$$B_f(A) = (B_f^{LD} - W_g) + K_A \left( A - \frac{A_{\text{fiss}}}{2} \right)^2 + W_f(A) \quad (4.5)$$

where  $B_f^{LD}$  is the liquid-drop fission barrier,  $W_g$  and  $W_f(A)$  are the shell corrections in the ground state and in the transition state, respectively and  $K_A$  is the stiffness parameter of the liquid drop with respect to mass-asymmetric variations at saddle:

$$K_A = \frac{1}{2} \frac{d^2 V(A)}{dA^2} \Big|_{A=A_{fiss}/2} \quad (4.6)$$

Inserting equation (4.5) into equation (4.4) and taking into account that at high excitation energies shell effects can be neglected, the mass yield  $Y(A)$  can be approximated by a Gaussian with the standard deviation

$$2\sigma_A^2 = \frac{\sqrt{E_{saddle}^* / a_f}}{K_A} = \frac{T_{saddle}}{K_A} \quad (4.7)$$

where  $E_{saddle}^*$  is the excitation energy of the fissioning nucleus over the fission barrier. Comparing equation (4.7) with equation (4.2) it follows that  $C_A = 2K_A$ .

Although the arguments that lead to equation (4.7) were based on the statistical model, the linearity between the variance of the mass distribution and the temperature at saddle has been confirmed by dynamical calculations. However, in this more complete picture the quantity  $C_A$  cannot be just interpreted as the stiffness of the liquid drop potential at saddle because it includes as well the dynamical effects that influence the charge distribution on the way from saddle to scission. In reference [VaK99] two-dimensional Langevin calculations were used to investigate the mass distribution of the fragments produced in the fission process of compound nuclei within the fissility range  $20 < Z^2/A < 40$ . For the compound nucleus  $^{205}\text{At}$  the dependence between  $\sigma_A^2$  and  $T_{saddle}$  was calculated for saddle-point temperatures reaching up to 2.4 MeV. The effective stiffness  $C_A$  that can be extracted from this calculated linear relation is in very good agreement with the value (corrected for angular momentum effects) that follows from the parameterisation of reference [MuS98]. This demonstrates that the parameterisation presented in [MuS98] is valid also at higher excitation energies. As will be illustrated in chapter 6, the quantitative analysis of the experimental widths of the charge distributions measured in our experiment is based on the comparison with model calculations. To obtain the calculated widths, the values of the constant  $C_Z$  for each fissioning nucleus are extrapolated from the parameterisation introduced in reference [MuS98].



# Chapter 5: Data analysis

In this chapter we will outline how the experimental data gained with the set-up described in the previous chapter have been analysed to determine the three observables whose sensitivity to dissipation will be studied in chapter 6. The first section reports on the ascertainment of the total fission cross sections for the reaction of  $^{238}\text{U}$  at 1 A GeV on different targets. For the reaction of  $^{238}\text{U}$  at 1 A GeV on a  $(\text{CH}_2)_n$  target we also established the partial fission cross sections and the widths of the charge distributions of the fission fragments. This is shown in sections 5.2 and 5.3, respectively.

## 5.1. Total fission cross-sections

The experimental set-up for fission studies, positioned behind the last image plane of the FRS, allowed for the measurement of the total fission cross-sections of  $^{238}\text{U}$  at 1 A GeV induced in  $(\text{CH}_2)_n$ , C, Cu, and Pb targets. The detectors used for the determination of the total fission cross sections were the MUSIC located before the target (MUSIC 1), the MUSIC placed behind the target (MUSIC 2) and the double IC situated after MUSIC 2 (see figure 4.5 of chapter 4). As was mentioned in section 4.2.1, the efficiency of the double IC is limited to approximately 90%. In contrast to the double IC, MUSIC 2 detects all the reaction products without any losses. This is the reason why instead of using the double IC we used MUSIC 2 to determine the number of fission events. Since the nuclear charge of the fission fragments is more or less half of the projectile nuclear charge, the fission fragments can be well identified by a peak positioned approximately in the middle of the energy-loss spectrum of MUSIC 2. This fission peak is, nevertheless, mixed with fragmentation events. Consequently, the total number of fission events can be determined if we remove this fragmentation background. Section 5.1.1.1 shows how, combining the information supplied by the double IC and MUSIC 2, the fragmentation background was determined. The various corrections applied to establish the cross sections are illustrated in section 5.1.2. Finally, the results are presented in section 5.1.3. If it is not mentioned explicitly, all the following figures correspond to the reaction of  $^{238}\text{U}$  at 1 A GeV on the  $(\text{CH}_2)_n$  target, but the procedure described is general and applies for all the targets.

### 5.1.1. Determination of the fission events

Fission fragments are emitted back-to-back isotropically in the projectile frame. The velocity distribution of the fission fragments, spherical and homogeneous in the centre-of-mass system, converts in the laboratory frame into an ellipsoid whose rotational axis is the projectile direction. The resulting velocity vectors lie inside a cone ending in an ellipsoidal shell that has a certain diffuseness due to the different mass partitions and to the distribution in total kinetic energy given by the fission process. The opening angle of the cone depends on the projectile velocity. For a projectile energy of 1 A GeV, the fission fragments are emitted within an angular range of about 30 mrad around the beam axis. In such conditions, both fission fragments pass through the MUSIC 2. In our experiment, the ADCs used were inhibited as soon as the slope of the energy-loss signal registered started to be negative. Hence, only the first signal arriving to the anode was processed. In the case of fission events emitted in the vertical plane YZ (see figure 5.5), the energy-loss signals of the fission fragments arrive to the anode of the MUSIC at the same time and the output signal corresponds to the sum of the energy-loss signals of the two fragments. For

a symmetric fission event, the corresponding energy-loss signal is about  $\frac{1}{2}$  of that of the projectiles. The energy-loss signals related to those fission residues that move in the other possible emission planes arrive to the anode at different times. Therefore, if we consider only symmetric fission events, the resulting energy-loss signals would be peaked at about  $\frac{1}{4}$  of that of the projectiles. The existence of asymmetric fission events leads to energy-loss signals that populate the gap between  $\Delta E_{loss}^{Proj}/4$  to  $\Delta E_{loss}^{Proj}/2$  and extend these limits to somewhat smaller or larger values. This can be seen in figure 5.1a), where the energy-loss spectrum recorded in MUSIC 1 is depicted. The central broad peak corresponds to the fission events produced before the projectile reaches the target, while the large peak at the highest energies corresponds to the projectiles that did not react before reaching the target. The integral of this peak gives the total number of  $^{238}\text{U}$  projectiles impinging on the target  $n_{proj}^0$ .

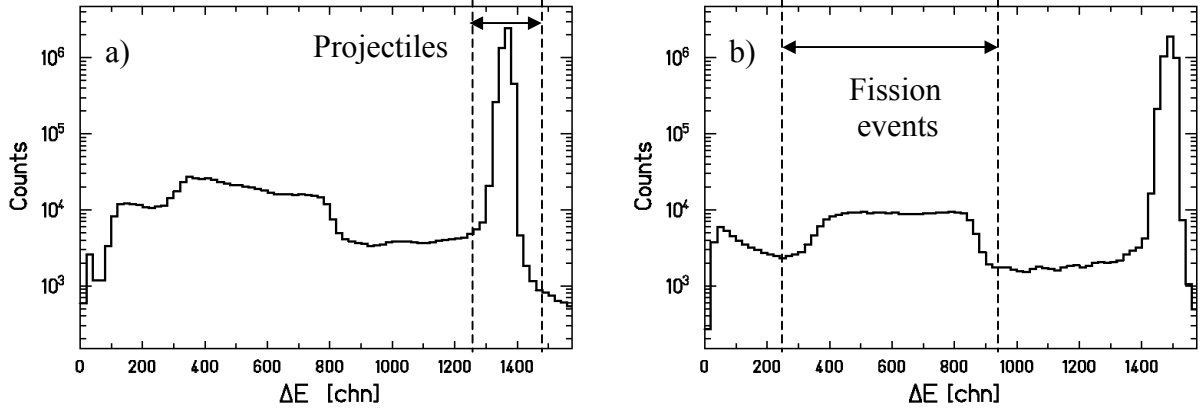


**Figure 5.1:** a) Energy loss in the MUSIC situated before the target, MUSIC 1. The window selects the projectiles of  $^{238}\text{U}$  at 1 A GeV that did not react before entering the target. b) Energy-loss signals in MUSIC 2 resulting from the passage of  $^{238}\text{U}$  at 1 A GeV through a  $(\text{CH}_2)_n$  target. The window contains the fission events.

The energy-loss spectrum recorded in MUSIC 2 for the projectiles selected by the window of figure 5.1a) shows again the same pattern as the one of MUSIC 1, see figure 5.1b). In this case, the middle peak is the interesting part since it contains the fission events emerging from the reaction of  $^{238}\text{U}$  in the target. However, this peak contains also fragmentation residues arising from collisions with impact parameters that decrease as the amplitude of the energy-loss signal decreases. Thus, to extract the number of fission events, the fragmentation background has to be defined and subtracted from the energy-loss spectrum of figure 5.1b).

### 5.1.1.1. The fragmentation background

In this section we will consider the various steps followed to determine the fragmentation background.

#### Step 1

The double IC situated after MUSIC 2 allows for measuring the energy-loss signal of both fission residues simultaneously and provides a good method to discriminate fission events from

fragmentation events and events emerging from central collisions. In figure 5.2, a cluster plot with the energy-loss signal in the upper part of the double IC against the energy-loss signal in the lower part is shown. The fission events are included in the window and populate the central peak, while the residues produced in fragmentation reactions and central collisions occupy the edges of the spectrum. The thin line of figure 5.3 represents the energy-loss signals measured in MUSIC 2 for the events outside the window of figure 5.2. This spectrum defines the first stage of the determination of the fragmentation background and we will call it *BG\_1*. However, this spectrum still contains fission events as reflected by the broad central peak.

The thick line of figure 5.3 represents the energy-loss spectrum in MUSIC 2 of all the residues produced by the passage of the  $^{238}\text{U}$  beam through the target. Besides the fission region, also the part of this spectrum corresponding to the heaviest fragmentation residues ( $\Delta E > 900$  channels) has more counts than the same part of the spectrum *BG\_1* (thin line). Two effects cause this difference: The projectiles that fission in MUSIC 2 and the heavy fragmentation products that fission between the second half of MUSIC 2 and the entrance of the double IC. The energy loss associated to the first group of events varies from the beginning of the fission peak until the largest energy-loss signal, depending on whether the fission process takes place at the entrance or at the exit of the of MUSIC 2. Concerning the second group of events, the heavy fragmentation products can be produced in the target, in the layer of air located after the target or in MUSIC 2. Both types of events are registered as fission events by the double IC and consequently do not appear in the background *BG\_1*.

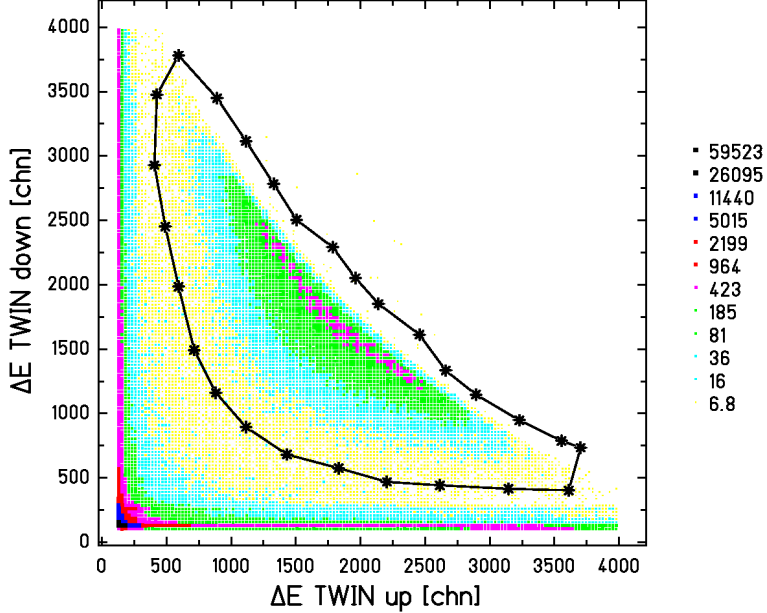


**Figure 5.2:** Energy-loss signal in the lower part of the double IC versus energy-loss signal in the upper part of the double IC for the reaction of  $^{238}\text{U}$  (1 A GeV) on  $\text{CH}_2$ . The window defines the fission events.

The events of the first type can be completely removed by subtracting the events produced in the dummy target. However, the events of the second type can only be partially removed because the heavy fragmentation residues produced in the target do not vanish when the dummy events are subtracted. Nevertheless, the number of events of the first type is 25 to 30 times larger than the

events of the second type. Therefore it is to be expected that, except for that tiny amount of heavy fragmentation residues produced in the target, the events causing the difference between the spectra of figure 5.3 in the heavy fragmentation region ( $\Delta E \geq 900$  channels) will be removed after subtracting the events of the dummy target.

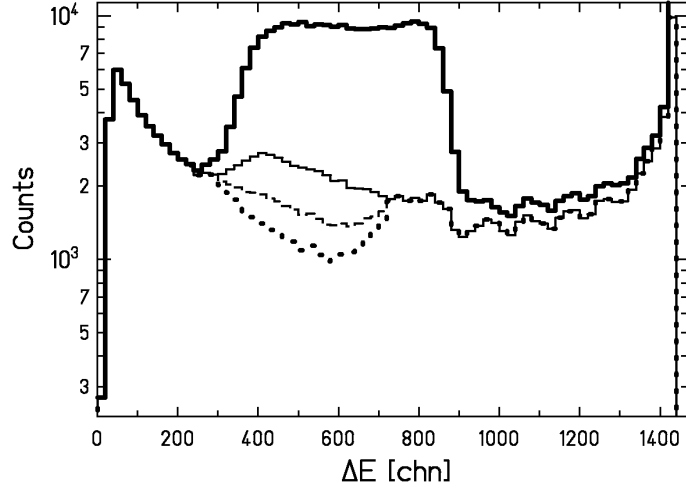


**Figure 5.3:** Fission peak in comparison with the spectra representing the different stages followed to determine the fragmentation background. The semilogarithmic scale has been chosen to better distinguish the different stages. The thick line represents the energy loss in MUSIC 2 of all the reaction products emerging from the  $(CH_2)_n$  target. The thin line corresponds to the spectrum  $BG\_1$ . It represents the energy-loss signal in MUSIC 2 of the fragmentation residues selected with the double IC. The dashed line represents the fragmentation background  $BG\_2$  obtained removing from  $BG\_1$  the events contained in the window of figure 5.6. The dotted line illustrates spectrum  $BG\_3$  obtained subtracting from  $BG\_2$  the fission fragments emitted in forward and backward direction.

## Step 2

Some fission fragments are still present in the background spectrum  $BG\_1$  (thin line of figure 5.3), because either one or both fragments hit the cathode of the double IC or both fission fragments entered into the same part of the double IC. The fraction of fission events not recognized by the double IC depends on the emittance and eventually some misalignment of the beam. The velocity vectors of these fission fragments populate a ring in the vicinity of the horizontal plane at the height of the beam, see figure 5.4. Most of these fission events can be identified with the drift-time signal of MUSIC 2, since the velocity distribution of the fission residues differs significantly from the one of the fragmentation residues. An upper view of the residue trajectories depicted in figure 5.5 shows that the fission fragments are emitted within a broader cone than the fragmentation residues. Consequently, the absolute difference between the drift-time signals delivered by the first and the last anode of the MUSIC 2 extends to larger values in the case of fission events than in the case of fragmentation events. This aspect was already used in [HeB96] to determine total fission cross sections. In figure 5.6, the energy-loss signals in MUSIC 2 of the events included in  $BG\_1$  are plotted as a function of the corresponding drift-time difference between the first and the last anode of MUSIC 2. The window of figure 5.6 marks fission events which are characterized by large angles with respect to the beam direction. Notice that the lightest fragments show also the largest angles, as can be deduced from

momentum conservation. The dashed line of figure 5.3 depicts the energy loss in MUSIC 2 after subtracting from  $BG\_1$  the events included in the window of figure 5.6. This line represents the second stage of the determination of the background and we will call it  $BG\_2$ .

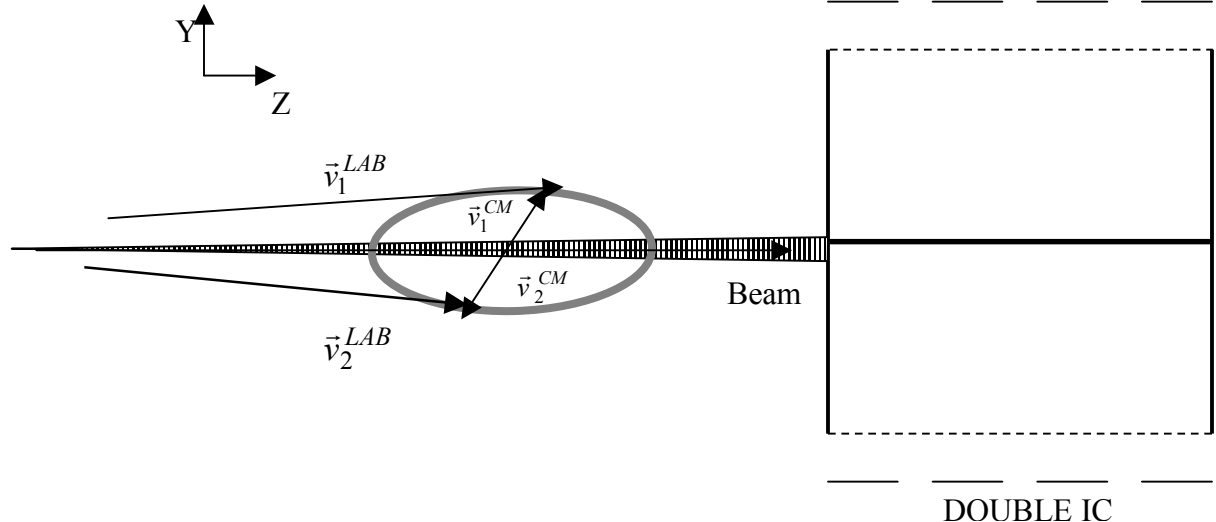


**Figure 5.4:** Schematic drawing of the velocity distribution of the fission fragments with respect to the geometry of the double IC. The ellipsoid represents the velocity distribution of the fission fragments in the laboratory frame. The velocity vectors of the fission fragments in the centre-of-mass frame are marked with the index CM and in the laboratory frame with the index LAB. The dashed area represents the fission fragments that hit the cathode or are detected in the same part of the double ionisation chamber.

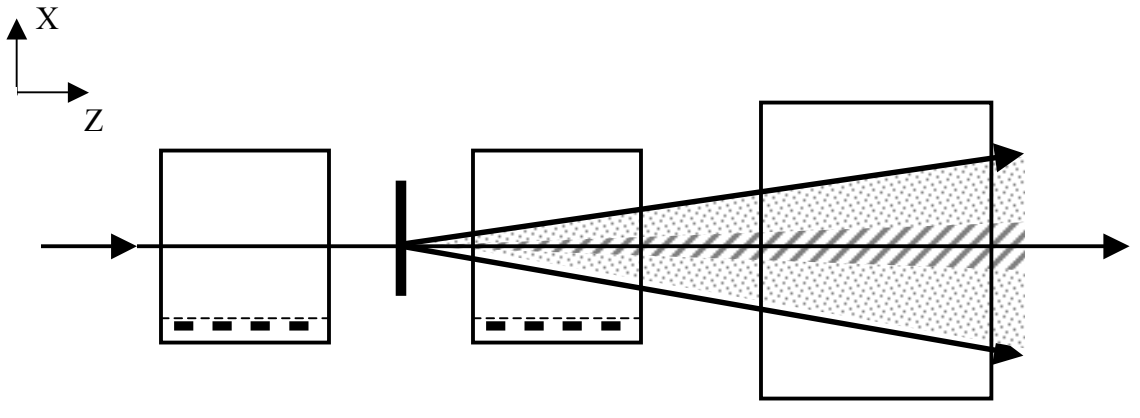


**Figure 5.5:** Schematic upper view of the experimental set-up and the trajectories of the reaction residues. The dotted area represents the projection of the angular distribution of the fission fragments on the horizontal plane XZ and the dashed area the projection of the angular distribution for the fragmentation residues.

Unfortunately, the heaviest fission fragments are only weakly deflected and cannot be separated from the fragmentation residues with the same nuclear charge. These events can be recognized in  $BG\_2$  (dashed line of figure 5.3) by the peak located around channel 800 in vertical direction. There is no way to remove these fission events from the background. However, it will be shown

later that, if the rest of the fragmentation background is well known, the shape of the background for the heaviest fission fragments can be well extrapolated.

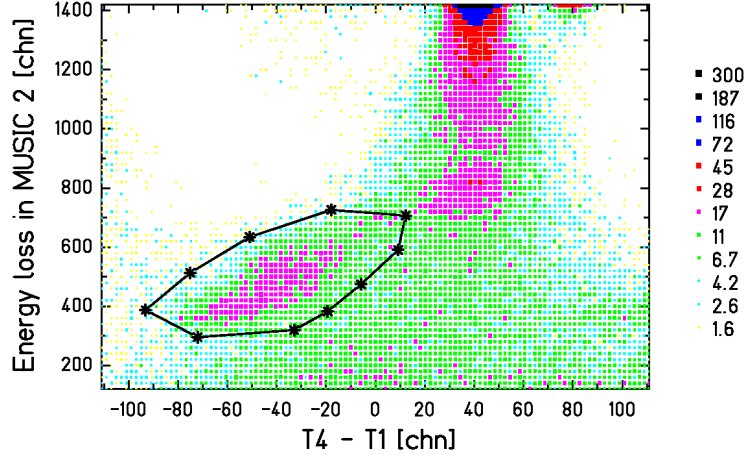


**Figure 5.6:** Energy loss in MUSIC 2 as a function of the difference in drift time between the fourth and first anode of MUSIC 2 for the events included in  $BG\_1$ . The window contains part of the fission events moving close to the horizontal plane that contains the beam.

### Step 3

The background spectrum  $BG\_2$  still contains fission events over the whole region from channel 300 to channel 900. These correspond to fission fragments emitted close to the beam axis in forward and backward direction. Their horizontal angles are too small to be distinguished from fragmentation products by the drift-time difference in figure 5.6. We estimated the contribution of these fission events to the background spectrum  $BG\_2$  from a geometrical consideration. Figure 5.7 schematically represents the projection onto the XZ plane of the horizontal ring formed by the velocity vectors of fission fragments not recognized by the double IC in the frame of the beam. We estimate that the window of figure 5.6 comprises approximately the fission events emitted with horizontal deflections larger than half the maximum horizontal deflection. In the frame of the beam, this means that the fission events where one of the fission fragments is emitted between  $0^\circ$  and  $30^\circ$  with respect to the beam direction are still present in the spectrum  $BG\_2$ , see figure 5.7. Therefore, the drift-time difference of MUSIC 2 was able to identify 2/3 of the fission events remaining in the background spectrum  $BG\_1$ . The outstanding part can be removed from  $BG\_2$  by performing the following operation with the spectra  $BG\_1$  and  $BG\_2$ :

$$BG\_3 = BG\_2 - 1/2 \cdot (BG\_1 - BG\_2) \quad (5.1)$$

The result is the spectrum  $BG\_3$  that is depicted by the dotted line in figure 5.3. Apart from the peak around channel 800 due to the heavy fission fragments, the spectrum  $BG\_3$  presents as well a smaller peak located around channel 280. This peak corresponds to very light fission fragments with large deflection angles that are not included in the window of figure 5.6.

The number of fission events still present in the background spectrum  $BG\_2$  is subject to an uncertainty. The estimation of this number was based on the shape of the drift-time difference distribution of the fission events (the left peak in figure 5.6) and on the drift time difference of the primary beam (upper right peak in figure 5.6). A closer look to figure 5.6 reveals that the mean

drift-time difference of the fragmentation products slightly shifts with decreasing amplitude. This is an indication for a walk of the constant-fraction discriminators. We conclude that the drift-time difference  $T_4-T_1$ , corresponding to the beam direction ( $\varphi = 0^\circ$ ) for nuclei as light as the fission fragments is only known with some uncertainty:

$$T_4-T_1(\varphi = 0^\circ) \approx (40 \pm 20) \text{ channels} \quad (5.2)$$

As a consequence, the lower limit of the window in figure 5.6 transforms into an emission angle of

$$\varphi \approx 30^\circ \pm 10^\circ \quad (5.3)$$

in the frame of the beam. Recalling figure 5.7, it finally results that the background spectrum  $BG\_3$  is subject to an uncertainty given by:

$$BG\_3 = BG\_2 - (0.5 \pm 0.2) (BG\_1 - BG\_2) \quad (5.4)$$

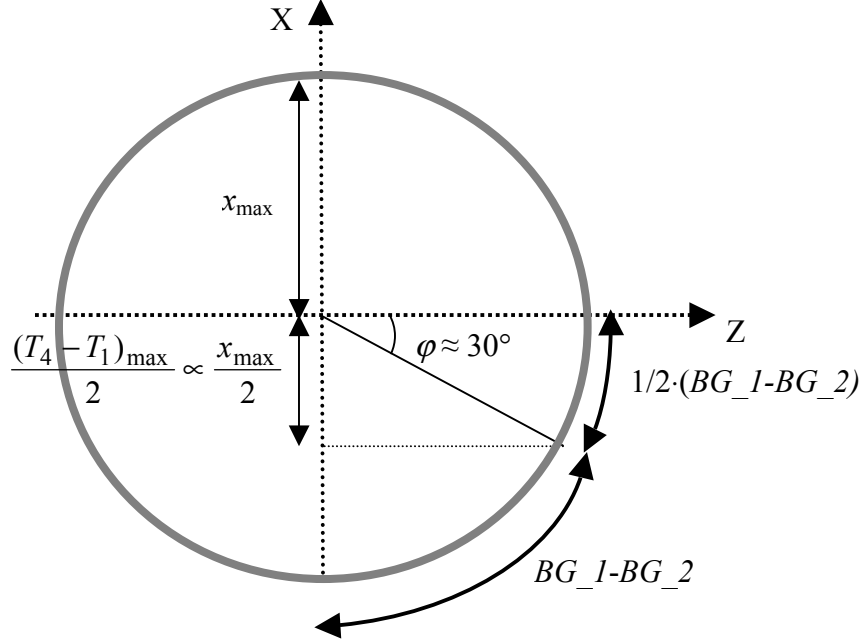


**Figure 5.7:** Projection onto the horizontal plane  $XZ$  of the distribution of velocities in the centre of mass frame for the fission events not recognized by the double IC. The figure shows the relation between the horizontal deflection  $x$  (or  $T_4-T_1$ ) and the deflection angle  $\varphi$ . The integral over the distribution from  $\varphi = 90^\circ$  to  $\varphi \approx 30^\circ$  gives the fission events contained in the window of figure 5.6. The integral from  $\varphi \approx 30^\circ$  to  $\varphi = 0^\circ$  gives the fission events still contained in  $BG\_2$ .

### 5.1.1.2. Number of fission events

Following the three steps described in the previous section with those events produced in the dummy target, we determined the corresponding fragmentation background  $BG\_3DUMMY$ . The final fragmentation background,  $BG\_FINAL$ , is obtained by subtracting from  $BG\_3$  the spectrum  $BG\_3DUMMY$  and fitting a fourth-degree polynomial to the resulting spectrum excluding the peaks around channels 280 and 800, see figure 5.8a). In addition, we also subtract the fission

events and the fragmentation residues produced in the dummy target from the spectrum of figure 5.1b) that contains the signals of all the reaction products. The final fragmentation background and the final spectrum of all reaction products from the plastic target are shown in figure 5.8b). The difference between these two spectra gives the number of fission events  $\dot{n}_{fiss}^{\exp}$  resulting from the reaction of the  $^{238}\text{U}$  projectiles at 1 A GeV with the target. The number of fission events is subject to the same uncertainty as the background spectrum  $BG\_3$  expressed by equation (5.4), that is:

$$\Delta\dot{n}_{fiss}^{\exp} = \pm 0.2 \sum BG\_1 - BG\_2 \quad (5.5)$$

where the sum extends over the entire energy-loss range of the spectra  $BG\_1$  and  $BG\_2$ .

Comparing figure 5.8b) and figure 5.3 one notices that, as expected, the subtraction of the reaction events occurred in the dummy target causes the two spectra of figure 5.8b) to coincide for the heavy fragmentation residues with  $\Delta E \geq 900$  channels. This last feature proves that the subtraction of the reaction products from the dummy has been properly done.

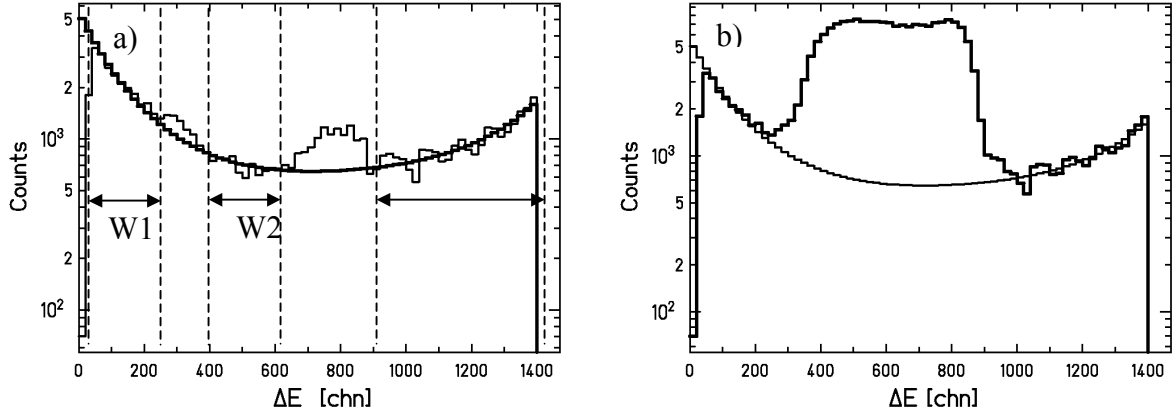


**Figure 5.8:** a) The thick line is the final fragmentation background  $BG\_FINAL$ . It has been obtained by fitting a fourth-degree polynomial to the spectrum represented by the thin line, which is the result of subtracting  $BG\_3DUMMY$  from the spectrum  $BG\_3$ .  $W1$ ,  $W2$  and  $W3$  indicate the parts of the spectrum represented by the thin line that have been used for the polynomial fit.  
 b) The thick line represents the energy-loss signals in MUSIC 2 after subtracting the signals of the residues produced in the dummy target. The thin line is the final fragmentation background  $BG\_FINAL$ .

### 5.1.2. Corrections applied to the total fission cross sections

The total fission cross sections are calculated according to the following expression:

$$\sigma_{fiss} = \frac{\dot{n}_{fiss}^{\exp} \cdot f_{sec} \cdot f_{centr}}{\dot{n}_{proj}^0 \cdot f_{atte} \cdot N_{target}} \quad (5.6)$$

where  $\dot{n}_{fiss}^{\exp}$  is the rate of fission events,  $\dot{n}_{proj}^0$  is the intensity of the projectile beam and  $N_{target}$  is the number of target atoms per unit area. We have described in the previous section, how to obtain the values for  $\dot{n}_{proj}^0$  and  $\dot{n}_{fiss}^{\exp}$ . The other terms of equation (5.6) are the correction factors for secondary reactions inside the target  $f_{sec}$ , for central collisions  $f_{centr}$  and for the beam attenuation inside the target  $f_{atte}$ . In this section a detailed description is presented on how the estimates for these corrections and the related uncertainties have been derived. In order to better assess the origin of the different corrections, the thicknesses of the different targets and the layers of matter located between the target and the double IC are listed in table 5.1 together with the corresponding nuclear reaction rates. In general, the corrections and the corresponding uncertainties have been accurately estimated for those effects that influence strongly the results. For the rest of the effects, the upper limits of the corrections are used.

	Material	Thickness [mg/cm <sup>2</sup> ]	Relative nuclear reaction rate
Targets	(CH <sub>2</sub> ) <sub>n</sub>	198.3	0.067
	C	376.0	0.066
	Cu	1792.0	0.089
	Pb	3265.9	0.073
Layers between target and double IC	Air	23.9	0.003
	Ar (MUSIC)	99.7	0.005
	Air	197.9	0.022

**Table 5.1:** Thicknesses and reaction rates of the different targets and the layers of matter located between the target and the double IC. The relative nuclear reaction rates in the targets have been calculated for <sup>238</sup>U at 1 A GeV, while the relative nuclear reaction rates in the rest of the layers have been calculated for the nucleus Z = 46 A = 116 at 1 A GeV. All calculations have been done using the model of [BeC89].

### 5.1.2.1 Losses of projectiles due to the beam attenuation inside the target

The number of <sup>238</sup>U projectiles decreases exponentially inside the target. Thus, the effective number of impinging projectiles at a certain length  $l$  of the target follows the expression:

$$\dot{n}_{proj}(l) = \dot{n}_{proj}^0 \cdot \exp\left(-\sigma_{total} \cdot \frac{dn_T}{dV} \cdot l\right) \quad (5.7)$$

where  $\dot{n}_{proj}^0$  is the number of projectiles at the entrance of the target,  $\sigma_{total}$  is the total reaction cross section inside the target and  $dn_T/dV$  is the number of target atoms per volume. The average number of projectiles impinging on a target of thickness  $L_{target}$  is given by:

$$\langle \dot{n}_{proj} \rangle \approx \frac{1}{L_{target}} \int_0^{L_{target}} \dot{n}_{proj}^0 \cdot \left(1 - \sigma_{total} \cdot \frac{dn_T}{dV} \cdot l\right) dl \quad (5.8)$$

In equation (5.8) we have assumed the case of a thin target where equation (5.7) can be approximated by a linear expression. The result of (5.8) is

$$\langle \dot{n}_{proj} \rangle = \dot{n}_{proj}^0 \cdot f_{atte} \quad (5.9)$$

with

$$f_{atte} \approx 1 - \frac{1}{2} \sigma_{total} \cdot N_{target} \quad (5.10)$$

and  $N_{target}$  given by

$$N_{target} = \frac{dn_T}{dV} \cdot L_{target} \quad (5.11)$$

The error associated to this correction is given by:

$$\Delta f_{atte} = \frac{1}{2} \sqrt{(N_{target} \Delta \sigma_{total})^2 + (\sigma_{total} \Delta N_{target})^2} \quad (5.12)$$

The total reaction cross section  $\sigma_{total}$  appearing in equation (5.10) is obtained from the sum of the total nuclear-induced reaction cross section calculated according to the soft-sphere model of Karol [Kar75] with the modifications introduced in [Bro94] and the total electromagnetic-induced reaction cross section calculated according to [ScS00]. The uncertainty associated to both models is of 5%.

### 5.1.2.2. Contribution to fission from secondary reactions inside the target

The considerations on the beam attenuation presented in the previous section only account for one-step reactions. Part of the heavy fragmentation residues, however, may undergo a second reaction in the target, eventually leading to fission. These events are included in the measured fission spectrum (thick line of figure 5.8b), we will call these fission events  $\dot{n}_{fiss}^{sec}$ . Since this contribution is rather small, a rough estimate is sufficient.

The evolution of  $\dot{n}_{fiss}^{sec}$  along the target is described by the differential equation:

$$\frac{d\dot{n}_{fiss}^{sec}}{dl} = \frac{dn_T}{dV} \sum_{Z_i, A_i} \sigma_{fiss}(Z_i, A_i) \cdot \dot{n}(Z_i, A_i, l) \quad (5.13)$$

where  $l$  is the coordinate in the beam direction,  $\sigma_{fiss}(Z_i, A_i)$  is the total fission cross section of a nucleus with charge  $Z_i$  and mass  $A_i$  different from the projectile, and  $\dot{n}(A_i, Z_i)$  is the number of nuclei with charge  $Z_i$  and mass  $A_i$ . Formulating this equation for every nucleus  $A_i$ ,  $Z_i$  gives a complete system of differential equations. To solve this system would require the knowledge of all cross sections involved. Therefore, we will introduce several approximations. The primary fragmentation products are certainly less fissile than the primary beam on the average, since they extend to appreciably lighter nuclei [HeS02]. An upper estimate of the contribution of secondary

reactions to the measured fission events is obtained by assuming that the fission cross section of the primary fragmentation residues is equal to the fission cross section of the primary projectiles. This means that we assume that  $\sigma_{fiss}(Z_i, A_i) \approx \sigma_{fiss}(Z_p, A_p)$ , where  $\sigma_{fiss}(Z_p, A_p)$  is the total fission cross section of the projectile of charge  $Z_p$  and mass  $A_p$ . With this, equation (5.13) turns into:

$$\frac{d\dot{n}_{fiss}^{\sec}}{dl} \approx \frac{dn_T}{dV} \cdot \sigma_{fiss}(Z_p, A_p) \sum_{Z_i, A_i} \dot{n}(Z_i, A_i, l) \quad (5.14)$$

An estimate of the increase of the primary fragmentation-evaporation products along the target represented by the term  $\sum_{Z_i, A_i} \dot{n}(Z_i, A_i, l)$  of equation (5.14) is given by:

$$\sum_{Z_i, A_i} \dot{n}(Z_i, A_i, l) \approx \dot{n}_{proj}^0 \cdot (\sigma_{tot}(Z_p, A_p) - \sigma_{fiss}(Z_p, A_p)) \cdot \frac{dn_T}{dV} \cdot l \quad (5.15)$$

where the total reaction cross section was obtained summing the nuclear component calculated by the models [Kar75, Bro94] plus the electromagnetic component calculated according to [ScS00]. The number of fission events that originate from secondary reactions is determined inserting expression (5.15) into equation (5.14) and integrating equation (5.14) over the whole target thickness  $L_{target}$ . The result is:

$$\dot{n}_{fiss}^{\sec} \approx \frac{1}{2} \cdot \dot{n}_{proj}^0 \cdot P_{fiss} \cdot (P_{tot} - P_{fiss}) \quad (5.16)$$

where we have used that  $N_{target} \cdot \sigma_{tot}$  and  $N_{target} \cdot \sigma_{fiss}$  correspond to the total reaction probability  $P_{tot}$  and to the total fission probability  $P_{fiss}$ , respectively.

A lower estimate for the number of secondary fission events is given by setting the fission cross section to zero in equation (5.13). Thus, the actual number of fission events  $\dot{n}_{fiss}$  will be between the upper limit given by the measured number of fission events  $\dot{n}_{fiss}^{\exp}$  and the lower limit  $\dot{n}_{fiss}^{\exp} - \dot{n}_{fiss}^{\sec}$ . Assuming that the correction for secondary reactions is the mean value of these two extremes, we arrive to the following estimate:

$$f_{sec} = 1 - \frac{1}{2} \frac{\dot{n}_{fiss}^{\sec}}{\dot{n}_{fiss}^{\exp}} \quad (5.17)$$

with  $\Delta\dot{n}_{fiss}^{\sec} = \pm \frac{1}{2} \dot{n}_{fiss}^{\sec}$ .

### 5.1.2.3 Losses of fission fragments due to central collisions

The fission fragments produced in the target have to pass several layers of matter until they arrive to the double IC. On this way at least one of the fission fragments may undergo a nuclear reaction. If the energy-loss signal of the reaction products in the double IC reduces so much that the event moves outside the window of figure 5.2, this event is not recognized as fission any

more. Events of this kind are considered as part of the fragmentation background, leading to an underestimation of the fission cross section. The number of such events is

$$\dot{n}_{fiss}^{central} \approx P_{central} \cdot \dot{n}_{fiss} + P_{central} \cdot (1 - P_{central}) \cdot \dot{n}_{fiss} \quad (5.18)$$

The first term on the right side of equation (5.18) accounts for the cases where the fission fragment whose energy-loss signal is registered by MUSIC 2 suffers a central collision and the second term corresponds to those events where the complementary fission fragment suffers the central collision, while the fragment responsible for the energy-loss signal in MUSIC 2 survives. The probability  $P_{central}$  depends on the size of the fission fragment. As a representative case, we estimated this value for symmetric fission by subtracting the probability for peripheral collisions from the total nuclear reaction probability calculated with the soft-sphere model of references [Kar75, Bro94]. The probability for peripheral collisions has been calculated applying the code ABRABLA [GaS91, JuJ98]. We defined as peripheral collisions those that lead to residues with charges larger than a limiting value. This limiting value can be deduced from the charge of the residues sited on the window that separates the fission peak from the rest of the residues in the double IC (figure 5.2), which is of approximately 30 units. The uncertainty of this loss of fission fragments due to central collisions between the target and the double ionization chamber is mainly determined by the uncertainty of the ABRABLA code. As an upper estimate we assume that the relative uncertainty of this correction amounts to 50 %. Thus,

$$f_{centr} = 1 + \frac{\dot{n}_{fiss}^{central}}{\dot{n}_{fiss}^{\exp}} \quad (5.19)$$

with  $\Delta\dot{n}_{fiss}^{central} = \pm \frac{1}{2}\dot{n}_{fiss}^{central}$ .

### 5.1.3. Results

According to equation (5.6), the relative uncertainty of the total fission cross section  $\sigma_{fiss}$  is:

$$\frac{\Delta\sigma_{fiss}}{\sigma_{fiss}} = \sqrt{\left(\frac{\Delta\dot{n}_{fiss}^{\exp}}{\dot{n}_{fiss}^{\exp}}\right)^2 + \left(\frac{\Delta N_{target}}{N_{target}}\right)^2 + \left(\frac{\Delta f_{atte}}{f_{atte}}\right)^2 + \left(\frac{\Delta f_{sec}}{f_{sec}}\right)^2 + \left(\frac{\Delta f_{centr}}{f_{centr}}\right)^2} \quad (5.20)$$

The procedure described in the previous sections has been applied to obtain the quantities involved in equations (5.6) and (5.20) and to determine the total fission cross sections of  $^{238}\text{U}$  at 1 A GeV on  $(\text{CH}_2)_n$ , C, Cu and Pb targets. The values of the relative errors appearing in equation (5.20) are listed in table 5.2. The largest sources of error are due to the uncertainty in the determination of the fragmentation background represented by  $\Delta\dot{n}_{fiss}^{\exp}$  and the uncertainty in the determination of the losses due to central collisions represented by  $\Delta f_{centr}$ .

We studied the reaction on  $(\text{CH}_2)_n$  because if we consider a component of the  $(\text{CH}_2)_n$  molecule we have:

$$\sigma_{fiss}(\text{CH}_2) = \sigma_{fiss}(\text{C}) + 2\sigma_{fiss}(\text{H}) \quad (5.21)$$

Applying equation (5.21) it is possible to deduce the very interesting total fission cross section of  $^{238}\text{U}$  on H. This cross section is of considerable interest for the development of neutron sources [Bau01, RiM98] and Accelerator Driven Systems (ADS) [Bow98, Sci99, NiD01], a new generation of nuclear reactors that combines a proton accelerator with a subcritical reactor. In a compilation of proton-induced fission cross-section data, Prokofiev [Pro01] developed a general systematic that predicts a cross section of 1.29 b for this reaction. This value is considerably lower than the results of Bochagov<sup>4</sup> et al. [BoB78] and of Vaishnene et al. [VaA81] listed in table 5.3. Consequently, our independent measurement of this reaction cross section can help to clarify this situation.

Target	$\frac{\Delta \dot{n}_{\text{fiss}}^{\text{exp}}}{\dot{n}_{\text{exp}}^{\text{fiss}}}$	$\frac{\Delta N_{\text{TARGET}}}{N_{\text{TARGET}}}$	$\frac{\Delta f_{\text{atte}}}{f_{\text{atte}}}$	$\frac{\Delta f_{\text{sec}}}{f_{\text{sec}}}$	$\frac{\Delta f_{\text{centr}}}{f_{\text{centr}}}$
C	1.75 %	0.25 %	0.12 %	0.61 %	1.95 %
$(\text{CH}_2)_n$	1.70 %	0.95 %	0.12 %	0.25 %	1.12 %
Cu	2.30 %	0.15 %	0.19 %	1.40 %	2.07 %
Pb	2.73 %	0.35 %	0.21 %	1.93 %	1.53 %

**Table 5.2:** Single contributions to the total relative error of the total fission cross sections. The values correspond to the fission reaction of  $^{238}\text{U}$  at 1 A GeV on different targets.

Target	$\sigma_{\text{fiss}}^{\text{total}} [\text{b}]$	$\sigma_{\text{fiss}}^{\text{total}} [\text{b}]$ other work
H	$1.52 \pm 0.10$	$1.47 \pm 0.07$ [BoB78] $1.48 \pm 0.06$ [VaA81]
C	$1.30 \pm 0.03$	$1.13 \pm 0.08$ [RuB96]
$(\text{CH}_2)_n$	$4.35 \pm 0.10$	
Cu	$1.89 \pm 0.06$	$1.86 \pm 0.11$ [RuB96]
Pb	$3.84 \pm 0.14$	$3.75 \pm 0.38$ [PoB94]

**Table 5.3:** Measured total fission cross sections for the reaction of  $^{238}\text{U}$  at 1 A GeV on different targets. The second column shows the results of this work and the third column the results of other references.

The measured total fission cross sections for all the targets and the corresponding absolute errors are listed in table 5.3 in comparison with the values obtained in independent work. In general, our results are in very good agreement with the results found in other measurements. Besides, except for the H target, the precision of our cross sections is higher than in former experiments. Our result for the H target corroborates the results of Bochagov et al. [BoB78] and of Vaishnene et al. [VaA81]. Moreover, adding the fragmentation cross section of  $^{238}\text{U}$  (1 A GeV) + p measured in [Tai00] (including estimated cross sections for a few unobserved channels), which is approximately 0.45 b with an uncertainty of about 15%, to the total fission cross section, a total reaction cross section of  $1.97 \pm 0.14$  b follows in very good agreement with the prediction of Karol's model [Kar75, Bro94] of 1.96 b.

<sup>4</sup> Prokofiev estimates that the uncertainty of this measurement is of 10% instead of 5%.

## 5.2. Partial fission cross sections

In the previous section we have shown how the total fission cross sections are determined by combining the information of the two MUSICs and the double IC. However, the double IC still provides very valuable information because it allows reconstructing the charge of the fissioning nuclei, which is given by the sum of the charges of the two fission fragments  $Z_1+Z_2$ . In this section it will be shown that different fissioning nuclei spanning over a broad charge interval contribute to the total fission cross sections. In particular, we will give quantitative values for the partial fission cross sections of the reaction of  $^{238}\text{U}$  at 1 A GeV on  $(\text{CH}_2)_n$ . Before presenting these results, we will report on the charge calibration of the energy-loss signals of the double IC and on the effect of the secondary reactions of the fission fragments on the partial fission cross sections.

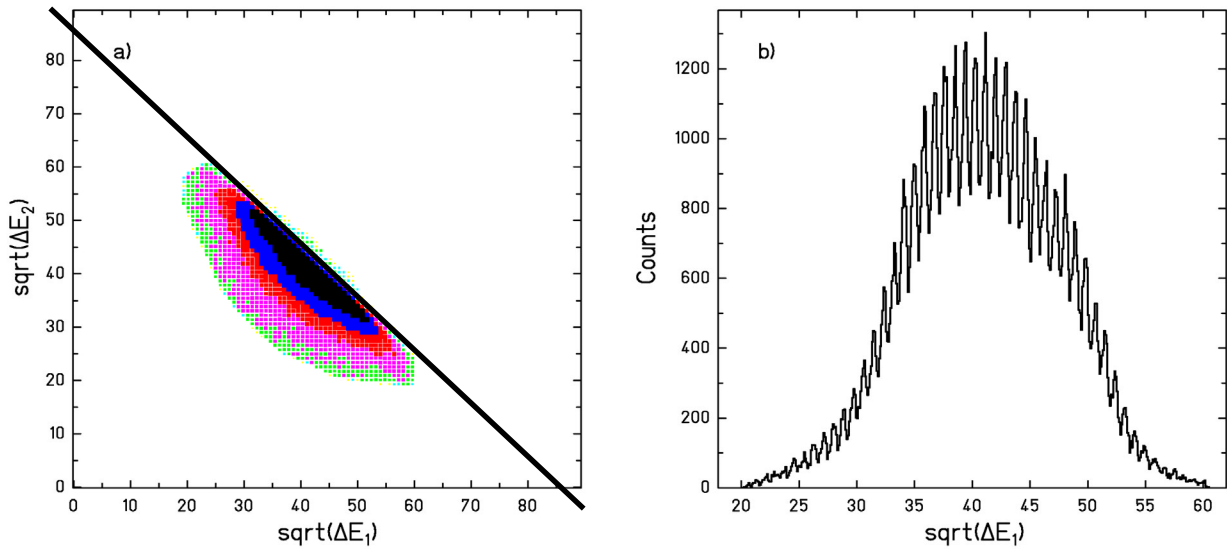


**Figure 5.9:** a) Square root of the signal amplitudes registered in the lower part of the double IC  $\sqrt{\Delta E_2}$  as a function of the square root of the signal amplitudes registered in the upper part  $\sqrt{\Delta E_1}$  for the fission events defined by the window of figure 5.2. The full line represents those combinations of  $Z_1$  and  $Z_2$  whose sum gives 92. b) Projection of part a) onto the  $x$ -axis.

### 5.2.1. Charge calibration

Given the measured ADC channel  $E_j$  of the energy-loss signal, the corresponding charge  $Z_j$  is given by the relation:

$$Z_j = \sqrt{a_j(E_j - b_j)} = \sqrt{a_j \Delta E_j} \quad (5.22)$$

where  $j = 1, 2$  refer to the upper part and the lower part of the double IC, respectively,  $a_j$  and  $b_j$  are the calibration parameters, and  $\Delta E_j$  is the ADC channel of the energy-loss signal after the subtraction of the offset  $b_j$ . While the offset values,  $b_j$ , are determined with a pulse generator, the values of  $a_j$  have to be deduced from the measured data. A reference point that allows assigning a charge to the energy-loss signals  $\Delta E_j$  can be found in figure 5.9. Figure 5.9a) represents the

square root of the energy-loss signals registered in the lower part of the double IC  $\sqrt{\Delta E_2}$  as a function of the square root of the energy-loss signals registered in the upper part  $\sqrt{\Delta E_1}$  for the fission events defined by the window of figure 5.3. This figure shows a sharp edge indicated by the full straight line. This line corresponds to those fission events for which  $Z_1+Z_2$  is equal to 92, the charge of the uranium projectile. The prolongation of this line until it cuts the  $x$  and  $y$ -axes determines the position of charge 92 on each axis and thus defines the values of  $a_1$  and  $a_2$ . Figure 5.9b) represents the projection of figure 5.9a) onto the  $x$ -axis. According to the reference point given by the full line of figure 5.9a), it is possible to assess the element numbers to the centers of the peaks of figure 5.9b). By performing a parabolic fit to the curve representing the square value of the center of these peaks as a function of the assigned charge, we slightly improve the values of the calibration parameters  $a_1$  and  $b_1$  of equation 5.22. The same procedure is used to refine the calibration parameters  $a_2$  and  $b_2$  of the lower part of the double IC.

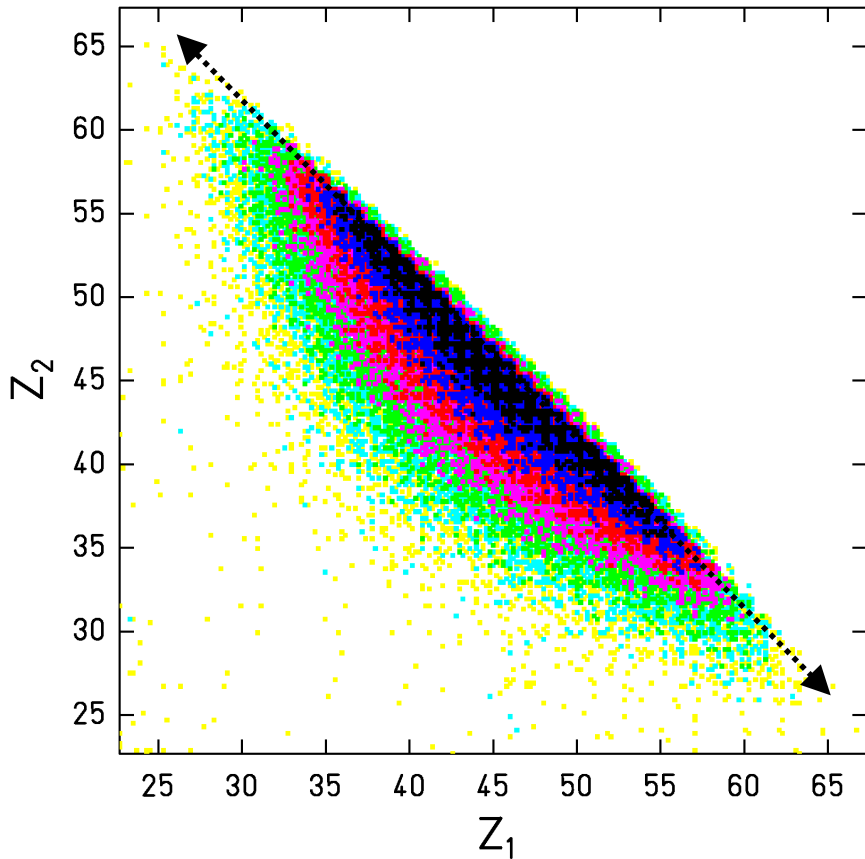


**Figure 5.10:** Nuclear charge of the fission fragment going through the lower part of the double IC as a function of the nuclear charge of the fragment passing through the upper part of the double IC for the reaction  $^{238}\text{U}$  (1 GeV) +  $(\text{CH}_2)_n$ . The dotted line represents the fission events with  $Z_1+Z_2 = 92$ .

After the charge calibration was done, the fission peak shown in figure 5.2 of section 5.1 transformed into the spectrum of figure 5.10. We can clearly distinguish the diagonal lines that correspond to fission events for which the sum of the charges  $Z_1+Z_2$  gives a fixed number. Each of these lines represents the possible combinations of charge splits associated to a fissioning element. From these considerations we conclude that fissioning elements ranging from charge 93 to approximately charge 70 contribute to the total fission cross section of  $^{238}\text{U}$  at 1 A GeV on  $(\text{CH}_2)_n$ . The yield of each fissioning element can be better observed if we represent the number of fission events as a function of  $Z_1+Z_2$ , this is shown in figure 5.11a). We performed a least-squares Gaussian fit to the individual peaks of this spectrum. Representing the areas of the Gaussians as a function of their centers, we obtained the curve of figure 5.11b).

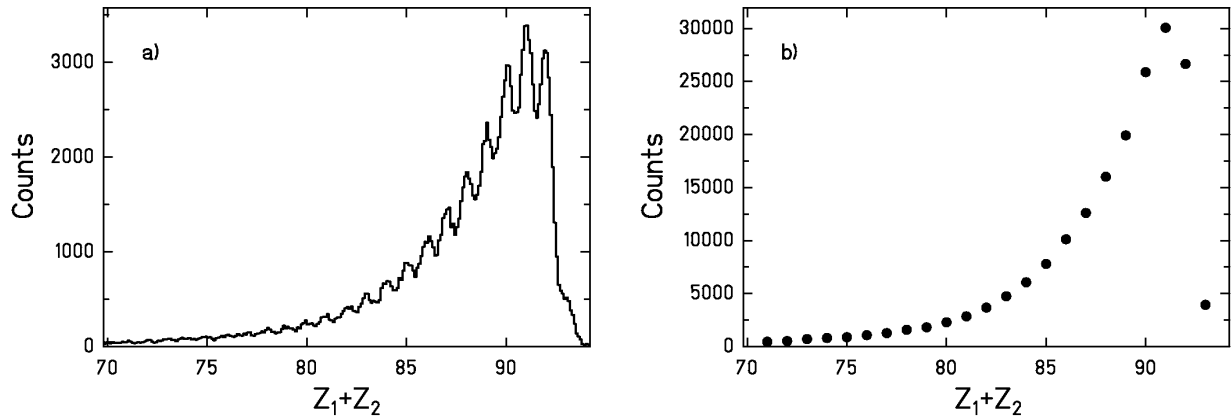


**Figure 5.11:** Number of fission events as a function of the sum of the nuclear charges of the two fission fragments  $Z_1+Z_2$ . a) Raw data after the charge calibration. b) Result of representing the areas of the Gaussian fits to the peaks of part a) as a function of the centers of the Gaussians. The statistical errors of the data points are smaller than the symbols used.

### 5.2.2. Secondary reactions

If a fission residue loses several protons due to fragmentation reactions within the path between the target and the entrance of the double IC, the corresponding fission event will be correlated to a lighter fissioning nucleus  $Z_1+Z_2$  than it actually corresponds to. Hence, before transforming the yields of figure 5.11b) into cross sections, we have to consider that the shape of this spectrum is affected by the secondary reactions of the fission residues on their way to the double IC. As a result of these secondary reactions the yields related to the heaviest fissioning nuclei are underestimated and the yields related to the lightest fissioning nuclei are overestimated. To correct for these effects we have to reconstruct the original charge distribution of the fission residues right after their production in the target. This is done following an iterative process:

- (a) We consider that the experimental spectrum of figure 5.11b), which we will call  $Y^{\text{exp}}$ , represents the real spectrum before the fission residues suffer any further interaction. Then we evaluate how this spectrum changes when considering the secondary reactions of the fission fragments until they reach the double IC. The resulting spectrum will be called  $Y_1^{\text{sec}}$ .

- (b) We assume that the difference  $Y_1^{\text{sec}} - Y^{\text{exp}}$  gives a good estimation of the effects caused by secondary reactions. If this assumption is correct, the spectrum  $Y_1^{\text{corr}}$  that results from the operation

$$Y_1^{\text{corr}} = Y^{\text{exp}} - (Y_1^{\text{sec}} - Y^{\text{exp}}) \quad (5.23)$$

should represent the real spectrum before being modified by secondary reactions.

- (c) To confirm that the correction has been properly done, an evaluation of the changes of  $Y_1^{\text{corr}}$  due to secondary reactions has to lead to a spectrum  $Y_2^{\text{sec}}$  that coincides with  $Y^{\text{exp}}$ . If they do not coincide, we do a second iteration

$$Y_2^{\text{corr}} = Y_1^{\text{corr}} - (Y_2^{\text{sec}} - Y^{\text{exp}}) \quad (5.24)$$

and so on, until  $Y_i^{\text{sec}}$  coincides with  $Y^{\text{exp}}$ .

The determination of the spectrum  $Y_1^{\text{sec}}$  defined in step (a) is actually a two-dimensional problem since for every value of  $Z_1 + Z_2$  there are many different combinations of charge splits, and each fission fragment should be treated independently. Thus, we have to calculate how an initial distribution of fission events as the one shown in figure 5.10 changes due to secondary fragmentation reactions in the different layers of matter. When an initial pair of fragments  $Z_1^i$ ,  $Z_2^i$  undergoes fragmentation reactions, the residues can populate all combinations of  $Z_1$  and  $Z_2$  below the initial values. Hence, the number of fission events  $N(Z_1^f, Z_2^f)$  that arrive to the double IC with charges  $Z_1^f$  and  $Z_2^f$  is given by:

$$N(Z_1^f, Z_2^f) = \sum_{Z_1 > Z_1^f} \sum_{Z_2 > Z_2^f} P(Z_1^f, Z_1^i) \cdot P(Z_2^f, Z_2^i) \cdot N(Z_1^i, Z_2^i) \quad (5.25)$$

where  $N(Z_1^i, Z_2^i)$  is the initial number of fission events with fragments of charges  $Z_1^i$ ,  $Z_2^i$  and  $P(Z_1^f, Z_1^i)$  ( $P(Z_2^f, Z_2^i)$ ) is the probability that an initial fission fragment of charge  $Z_1^i$  ( $Z_2^i$ ) arrives to the upper part of the double IC with charge  $Z_1^f$  ( $Z_2^f$ ).

The survival probability for an initial fission fragment  $Z_1^i$  is given by:

$$P(Z_1^i, Z_1^i) = 1 - P_{\text{tot}} + \sum_{A_{\text{min}}^f}^{A_{\text{max}}^f} P(A^f, Z_1^i, A^i, Z_1^i) \quad (5.26)$$

where the total nuclear reaction probability  $P_{\text{tot}}$  is determined using the model of Benesh et al. [BeC89]. The last term of equation (5.26) gives the probability that only neutrons are removed.

The probabilities for charge changing appearing in equation (5.25) and the probability for neutron removal of equation (5.26) are obtained by applying the semi-empirical code EPAX [SüB00]. EPAX relies on the fact that the production cross sections of the residues resulting from heavy-ion collisions with a specific projectile follow a fixed pattern that just needs to be scaled according to the total reaction cross section for a particular target material. However, such consideration is not valid for the H<sub>2</sub> of the (CH<sub>2</sub>)<sub>n</sub>-target because fragmentation reactions in H<sub>2</sub> cannot be reproduced by EPAX. Therefore, for the case of the H<sub>2</sub> layer these probabilities are calculated separately according to a fast simplified version of the CASCABLA code [CuV97, JuJ98] (see appendix of reference [EnW01]).

To determine the final distribution  $Z_1^f, Z_2^f$  after traversing the whole path from the middle of the target to the entrance of the double IC we proceeded in two steps. First we determined the distribution  $(Z_1^f, Z_2^f)_H$  after traversing the H<sub>2</sub> layer of the (CH<sub>2</sub>)<sub>n</sub> target by means of equations (5.25) and (5.26) using CASCABLA. Then the result  $(Z_1^f, Z_2^f)_H$  was used as the input distribution  $Z_1^i, Z_2^i$  and via EPAX we determined the effects of the secondary reactions from the carbon layer of the target to the entrance of the double IC. Instead of treating each layer separately, we considered a nitrogen target whose thickness leads to the same total reaction probability as the whole group of layers.

In figure 5.12a) a comparison of spectra  $Y_1^{\text{sec}}$  (dashed-line) and  $Y^{\text{exp}}$  (full line) is depicted. One sees how secondary reactions cause a depopulation of the largest values of  $Z_1+Z_2$  and an increase of the lighter ones. For the present data, the process described in steps (a), (b) and (c) converges after one iteration. Consequently, spectrum  $Y_1^{\text{corr}}$  introduced in step (b) defines the corrected version of  $Y^{\text{exp}}$ .  $Y_1^{\text{corr}}$  (full dots) and  $Y^{\text{exp}}$  (empty dots) are represented in figure 5.12b).

According to equation (5.23), the error of  $Y_1^{\text{corr}}$  is given by

$$\Delta Y_1^{\text{corr}}(Z_1+Z_2) = \sqrt{(\Delta Y^{\text{exp}}(Z_1+Z_2))^2 + (\Delta N^{\text{sec}}(Z_1+Z_2))^2} \quad (5.27)$$

where  $\Delta Y^{\text{exp}}(Z_1+Z_2)$  is the error of the Gaussian fits and  $\Delta N^{\text{sec}}(Z_1+Z_2)$  is the error associated to the correction for secondary reactions given by the difference between  $Y_1^{\text{sec}}$  and  $Y^{\text{exp}}$ . The correction  $N^{\text{sec}}(Z_1+Z_2)$  has two components:

$$N^{\text{sec}}(Z_1+Z_2) = N_{\text{pop}}(Z_1+Z_2) - N_{\text{depop}}(Z_1+Z_2) \quad (5.28)$$

$N_{\text{pop}}$  represents the population of the channel  $Z_1+Z_2$  due to the secondary reactions of other fission products with larger nuclear charges (equation 5.25) and  $N_{\text{depop}}$  represents the depopulation of channel  $Z_1+Z_2$  caused by the secondary reactions of the partners  $Z_1$  and  $Z_2$  (equation 5.26). The uncertainty related to  $N_{\text{pop}}$  is given by the uncertainty of EPAX or CASCABLA that we estimate is of about 20%. The uncertainty related to  $N_{\text{depop}}$  is mainly given by the determination of  $P_{\text{tot}}$  according to the model of Benesh et al. [BeC89] whose uncertainty is estimated to be of 5%. In view of these ideas we estimate a relative uncertainty for  $N^{\text{sec}}$  of:

$$\frac{\Delta N_{\text{sec}}(Z_1 + Z_2)}{Y_1^{\text{corr}}} = \frac{1}{Y_1^{\text{corr}}} (0.2 \cdot N_{\text{pop}}(Z_1 + Z_2) + 0.05 \cdot N_{\text{depop}}(Z_1 + Z_2)) \quad (5.29)$$

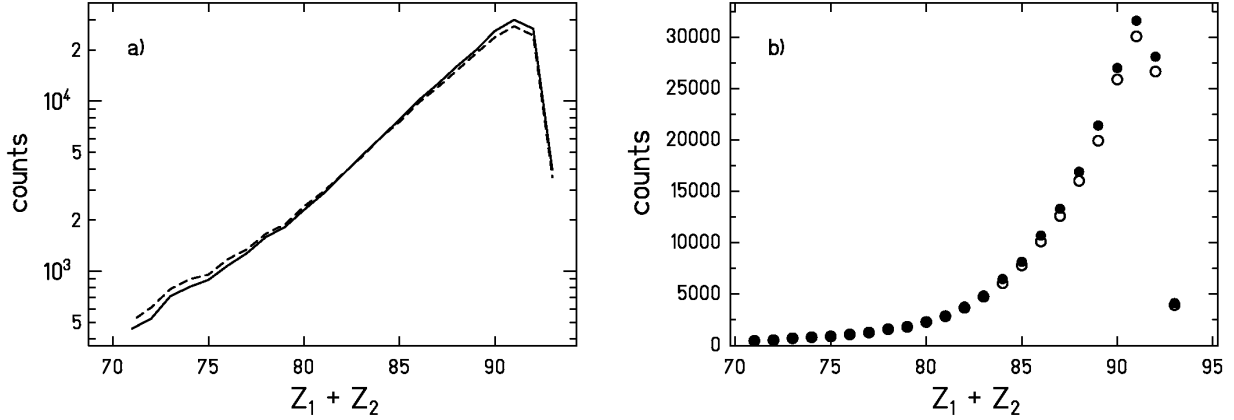


**Figure 5.12:** a)  $Y^{\text{exp}}$  (full-line) in comparison with  $Y_1^{\text{sec}}$  (dashed-line). b) Experimental data  $Y^{\text{exp}}$  (empty dots) in comparison with the data corrected for secondary reactions  $Y_1^{\text{corr}}$  (full dots). For both curves the error bars are smaller than the symbols.

According to the yields represented by the full dots in figure 5.12b), the average fissioning element produced in the reaction of  $^{238}\text{U}$  at 1 A GeV on a  $(\text{CH}_2)_n$  target is  $\langle Z_1 + Z_2 \rangle \approx 88.1$ . In [ScB98], the fragmentation fission reaction of  $^{238}\text{U}$  at 750 A MeV on Pb was studied leading to mean fissioning nucleus of charge  $\langle Z_1 + Z_2 \rangle \approx 86$ . The difference between both results might be explained by the fact that the protons of the  $(\text{CH}_2)_n$  target lead to a higher production of fragmentation residues in the vicinity of the projectile. This shifts the average charge of the fissioning element to higher values.

### 5.2.3. Results

In the whole procedure until we arrived to the spectrum  $Y_1^{\text{corr}}$ , we considered only the fission events included in the fission window defined in figure 5.2. It has been shown in section 5.1 that the fission events moving close to the horizontal plane that contains the beam are not included in this window. However, these events are distributed homogeneously along the whole  $Z_1 + Z_2$  range. Therefore, we can correct for these losses normalizing the spectrum  $Y_1^{\text{corr}}$  to the total fission cross section determined in section 5.1. The results  $\sigma_f(Z_1 + Z_2)$  are depicted in figure 5.13 and listed in table 5.4. If we assume that the spectrum of figure 5.13 continues to lower values of  $Z_1 + Z_2$  with the same logarithmic slope, then this spectrum shows approximately 99% of the total fission cross section. For this reason, in the normalization procedure we included also the missing 1% with  $Z_1 + Z_2 < 71$  that does not appear in figure 5.12b).

In addition to the uncertainties of the individual partial yields due to the counting statistics and the uncertainties of the corrections for secondary reactions, the uncertainty of the total fission

cross section has to be added to the final uncertainties of the partial fission cross sections  $\Delta\sigma(Z_1+Z_2)$ .

Figure 5.13 shows how the cross sections decrease with the charge of the fissioning nucleus. Several effects define this trend. On the one hand, the fission barriers increase with decreasing charge of the fissioning nucleus. On the other hand, the light fissioning nuclei are the result of central collisions, which are less probable. Nevertheless, as was explained in section 4.3, the partial fission cross sections are expected to depend on dissipation as well. A quantitative analysis of this dependence is presented in the next chapter.

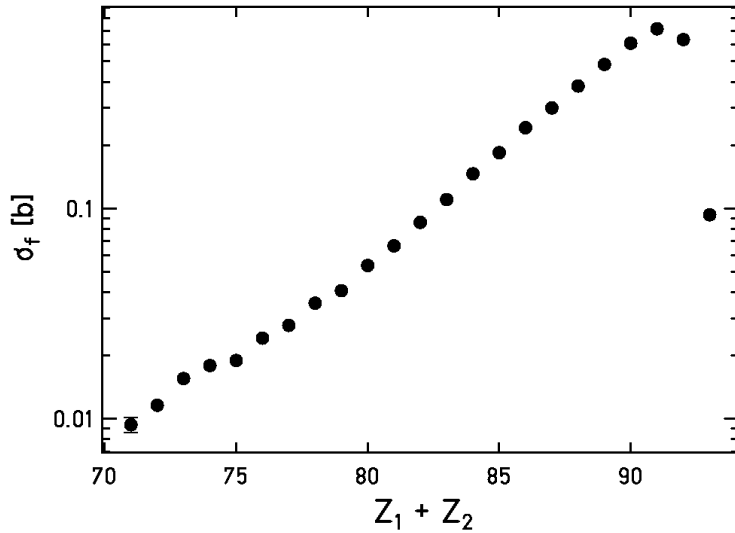


**Figure 5.13:** Partial fission cross sections for the reaction of  $^{238}\text{U}$  at 1 A GeV on  $(\text{CH}_2)_n$ . The  $x$ -axis represents the sum of the nuclear charges of the fission fragments.

Among the partial fission cross sections listed in table 5.4, the case of  $Z_1+Z_2=93$  is of special interest. Fissioning nuclei of charge 93 are formed due to charge-exchange (or charge pick up) reactions [BeD00, SüR95]. Rubehn et al. [RBa96] measured the cross sections for charge pick-up and subsequent fission of  $^{238}\text{U}$  projectiles at 1 A GeV on different targets. Using the result for the C target from this reference and recalling that:

$$\sigma_{\Delta Z+1}(H) = \frac{1}{2} [\sigma_{\Delta Z+1}(\text{CH}_2) - \sigma_{\Delta Z+1}(\text{C})] \quad (5.30)$$

This work adds the value for the hydrogen target with  $28 \pm 5$  mb. As shown in figure 5.14, this result is in good agreement with the overall target-mass dependence found in [RBa96]. Due to the high fissility of  $^{238}\text{Np}$  and the lighter neptunium isotopes, one might assume that nearly the full cross section for charge pick up of  $^{238}\text{U}$  can be found in the fission channel. At least our value gives a lower estimate of the total charge pick up cross section that can be compared to systematics.

$Z_1+Z_2$	$\sigma_f [b]$	$\Delta\sigma_f [b]$
71	0.009	0.001
72	0.012	0.001
73	0.016	0.001
74	0.018	0.001
75	0.019	0.001
76	0.024	0.001
77	0.028	0.001
78	0.035	0.002
79	0.041	0.002
80	0.054	0.002
81	0.066	0.002
82	0.086	0.003
83	0.110	0.003
84	0.146	0.004
85	0.184	0.005
86	0.242	0.005
87	0.300	0.006
88	0.382	0.009
89	0.483	0.010
90	0.610	0.012
91	0.714	0.013
92	0.635	0.012
93	0.093	0.003

**Table 5.4:** Values of the partial fission cross sections for the reaction of  $^{238}\text{U}$  at 1 A GeV on  $(\text{CH}_2)_n$ .

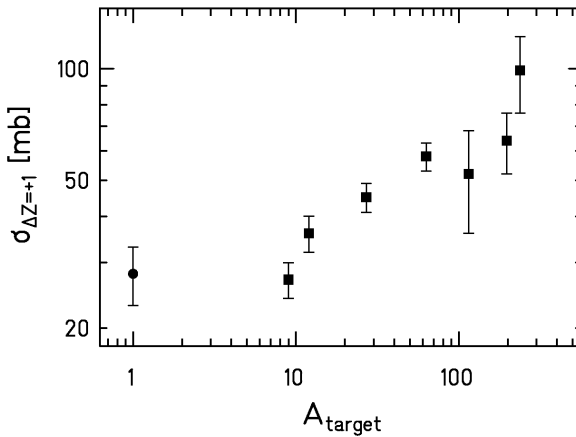


**Figure 5.14:** Cross sections for charge pickup and subsequent fission of  $^{238}\text{U}$  projectiles at 1 A GeV as a function of the target mass. The squares represent the measured data from reference [RBa96] and the dot represents the cross section for H determined in this work.

### 5.3. Widths of the charge distributions of the fission fragments

The charge distributions of the fission fragments for a fixed fissioning element  $Z_1+Z_2$  produced in the reaction of  $^{238}\text{U}$  at 1 A GeV on  $(\text{CH}_2)_n$  can be obtained by projecting the diagonal lines of figure 5.10 to either the  $x$  or the  $y$ -axis. Figure 5.15 shows two examples, the case of  $Z_1+Z_2 = 90$ , in part a) and the case  $Z_1+Z_2 = 92$ , in part b). The asymmetric charge distribution of the fissioning nucleus with charge 92 is characteristic of the contribution of low-energy fission. Here, the excitation energy is induced by the electromagnetic interaction with the target nuclei and by elastic scattering or very peripheral nuclear collisions where only few neutrons are abraded. For lighter fissioning nuclei, the impact parameter becomes smaller and the induced excitation energy increases. Hence, the influence of the shell effects is increasingly attenuated and the charge distributions become symmetric. In fact, as shown in figure 5.15a), shell effects are almost vanished already for  $Z_1+Z_2 = 90$ . As explained in section 4.3, when shell effects are washed out, the width of the charge distribution scales with the temperature at the saddle point. Therefore in our analysis of the widths we will only consider symmetric charge distributions. To determine them, we perform Gaussian fits to the charge distributions based on the method of the maximum likelihood, assuming the data to be Poisson distributed. The result of the fit for the case of  $Z_1+Z_2=90$  is shown by the full line of figure 5.15a).

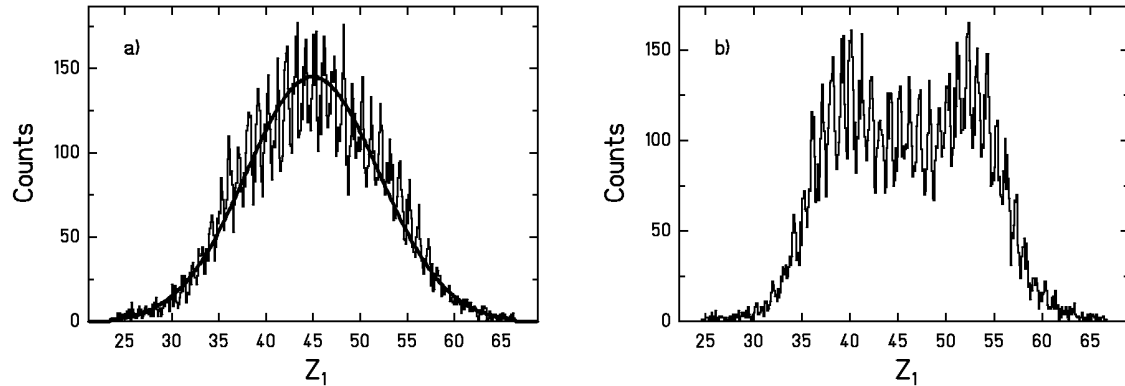


**Figure 5.15:** Fission-fragment element distribution. a) For the fissioning nucleus  $Z_1+Z_2 = 90$ , the full line is the result of the Gaussian fit. b) For the fissioning nucleus  $Z_1+Z_2 = 92$ .

The influence of the charge resolution  $\Delta Z$  of the double IC, which has a value of approximately  $\pm 0.26$  units (standard deviation), on the measured widths  $W_{\text{measured}}$  has been corrected for:

$$W_{\text{corr}} = \sqrt{(W_{\text{measured}})^2 - (\Delta Z)^2} \quad (5.31)$$

Although this represents only a tiny effect. The standard deviations of the charge distributions are represented in figure 5.16 as a function of  $Z_1+Z_2$ . The error bars represent the uncertainties of the fits.

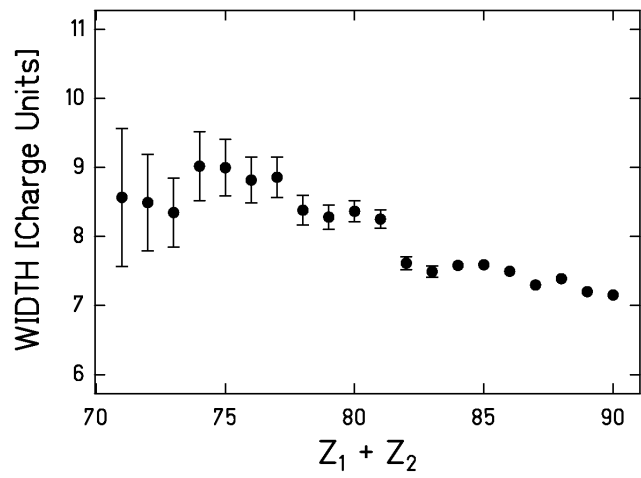


**Figure 5.16:** Standard deviations of the charge distributions as a function of the sum charge of the fission fragments  $Z_1+Z_2$  for the reaction of  $^{238}\text{U}$  at 1 A GeV on  $(\text{CH}_2)_n$ .



# Chapter 6: Interpretation of the experimental data

To deduce quantitative results on dissipation at small deformation, the experimental observables introduced in chapters 4 and 5 need to be compared with a nuclear-reaction code. In this chapter we will firstly describe the model used, paying special attention to the modelling of dissipation effects in fission. Secondly, the comparison of the experimental data with the calculations will be illustrated and finally, the results will be discussed.

## 6.1. The abrasion-ablation model

The nuclear-reaction code used is an extended version of the abrasion-ablation Monte-Carlo code ABRALBA [GaS91, JuJ98]. This code consists of three stages. In the first stage the characteristics of the projectile residue right after the fragmentation are described according to the geometrical abrasion model. The second stage accounts for the simultaneous emission of nucleons and clusters (simultaneous break-up) that takes place due to thermal instabilities when the temperature of the projectile spectator exceeds 5.5 MeV [Ric02, ScR02]. After the break-up, the ablation stage models the sequential deexcitation of the system through an evaporation cascade. In the following subsections we briefly describe the main features of each stage.

### 6.1.1. Abrasion stage

The abrasion model [BoS73] is well suited for describing the properties of the projectile fragment after peripheral collisions. The basic idea of this model is that at relativistic energies ( $> 100$  A MeV) the relative velocity of the reaction partners is large compared to the Fermi velocity of the nucleons in the potential well. In addition, the associated wavelength of the projectile is of the order of the size of the nucleons. Thus, in the overlap zone between the projectile and the target many nucleon-nucleon collisions take place, while the nucleons in the not-overlapping region are only little disturbed by the abrasion.

Depending on the impact parameter, a distribution of projectile fragments with different masses and charges are formed due to the abrasion process. The mass loss can be determined geometrically integrating the overlapping volume. For a given mass loss, the  $N/Z$  distribution is determined assuming that every nucleon removed has a statistical chance to be a neutron or a proton as determined by the neutron-to-proton ratio of the precursor nucleus. The result is a hypergeometrical distribution centered at the  $N/Z$  ratio of the projectile. The angular-momentum distribution [JoI97] of the projectile fragments is given in analogy to Goldhaber's description for the linear-momentum distribution of the projectile residues. According to this idea, the angular-momentum distribution is defined by the angular momenta of the nucleons removed. In the same way, the excitation-energy distribution of the projectile residues is given by the sum of the energies of the holes in the single-particle scheme of the initial nucleus which are formed due to the removal of nucleons. Including final-state interactions derived from measured isotopic production cross sections [ScB93], an average excitation energy of 27 MeV per nucleon abraded is induced. This value is in agreement with predictions for peripheral collisions based on BUU calculations [Hub91].

### 6.1.2. Simultaneous break-up

Mid-peripheral heavy-ion collisions allow producing nuclei with excitation energies that are far beyond the onset of multifragmentation [PoT00]. Nuclear dynamics in this range of excitation energies is the subject of current research. As presented in reference [Ric02, ScR02], the analysis of the isotopic distributions of heavy projectile fragments from the reactions of a  $^{238}\text{U}$  beam in a lead target and a titanium target gave some evidence that the initial temperature of the last stage of the reaction, the evaporation cascade, is limited to a universal upper value of approximately 5.5 MeV. The interpretation of this effect relies on the onset of a simultaneous break-up process for systems whose temperature after the abrasion is larger than 5.5 MeV. In ABRALBA, the simultaneous break-up stage has been modelled in a quite rough way that, however, shows a very good agreement with the experimental data. If the temperature after abrasion exceeds the freeze-out temperature of 5.5 MeV, the additional energy is used for the formation of clusters and the simultaneous emission of these clusters and several nucleons. The number of protons and neutrons emitted is assumed to conserve the  $N$ -over- $Z$  ratio of the projectile spectator, and an amount of about 20 MeV per nuclear mass unit emitted is released. This last quantity is still under investigation. Nevertheless, its effect on the results is very small. The break-up stage is assumed to be very fast, and thus the fission collective degree of freedom is not excited. After the spontaneous emission, the piece left of the projectile spectator undergoes the sequential decay.

### 6.1.3. Ablation stage

We assume that either after the abrasion or after the simultaneous break-up the intrinsic degrees of freedom of the projectile residue are in thermal equilibrium. The ablation stage describes the sequential deexcitation of the projectile fragment by particle evaporation and/or fission. The decay widths for particle emission are obtained from the statistical model; for instance, the neutron width is given by:

$$\Gamma_n = \frac{1}{2\pi\rho(E)} \frac{4m_n R^2}{\hbar^2} T_r^2 \rho_r(E - S_n) \quad (6.1)$$

$\rho(E)$  is the level density of the compound nucleus,  $S_n$  is the neutron separation energy,  $m_n$  is the neutron mass,  $R$  is the nuclear radius,  $\rho_r(E)$  is the level density of the daughter nucleus after neutron emission and  $T_r$  is the temperature of the daughter nucleus after neutron emission. The proton width  $\Gamma_p$  follows an analogue formula as the neutron width of equation (6.1) but the level density of the daughter nucleus  $\rho_r(E - Sp - B_p^{\text{eff}})$  is shifted by the effective Coulomb-barrier.

As discussed in chapter 2, dissipation causes an initial suppression of the fission width, afterwards the fission width grows and finally reaches the asymptotic value given by the product of the Kramers factor (equation (2.9) of section 2.3) and the fission width  $\Gamma_f^{BW}$ , which is determined according to the transition-state model [BoW39], see also [Mor74]:

$$\Gamma_f^{BW} = \frac{1}{2\pi\rho(E)} T_{sad} \rho_{sad}(E - B_f) \quad (6.2)$$

The level density of the fissioning nucleus at saddle is  $\rho_{sad}(E)$ , and the level density of the compound nucleus is  $\rho(E)$ . The temperature of the nucleus at saddle is  $T_{sad}$ , and the fission barrier

is  $B_f$ . Besides the treatment of the dissipation effects that will be described in the next section, the most critical ingredients that define the fission width are the ratio of the level-density parameters  $a/a_n$ , and the fission barriers  $B_f$ . The ratio  $a/a_n$  is calculated considering volume and surface dependencies as proposed in reference [IgI75] according to the expression:

$$a = \alpha_v A + \alpha_s A^{2/3} B_s + \alpha_k A^{1/3} B_k \quad (6.3)$$

where  $\alpha_v$ ,  $\alpha_s$  and  $\alpha_k$  are the coefficients of the volume, surface and curvature components of the single-particle level densities, respectively, with the values  $\alpha_v = 0.073 \text{ MeV}^{-1}$ ,  $\alpha_s = 0.095 \text{ MeV}^{-1}$  and  $\alpha_k = 0 \text{ MeV}^{-1}$ .  $B_s$  and  $B_k$  are the ratios of the surface of the deformed nucleus and the integrated curvature of the nucleus, respectively, related to the corresponding values of a spherical nucleus. Their values are taken from reference [MyS74]. The angular-momentum dependent fission barriers are taken from the finite-range liquid-drop model predictions of Sierk [Sie86]. As demonstrated in reference [BeA02], a recent experimental determination of these parameters by K. X. Jing and co-workers [JiP01], based on the measurement of cumulative fission probabilities of neighbouring isotopes, is in very good agreement with these theoretical predictions.

## 6.2. Modelling of the effects of dissipation in fission

Provided the initial conditions of the excited nucleus fulfil the requirements of the model of Grangé and Weidenmüller [GrJ83] illustrated in section 2.3, investigating the effects of dissipation in the deexcitation process of such a nucleus implies modelling the time-dependent onset of the flux over the fission barrier that is expressed by a time-dependent fission decay width  $\Gamma_f(t)$ . This is a rather complicated task, and most of the model calculations contain one of the following approximations for  $\Gamma_f(t)$ :

- A step function that sets in at time  $\tau_f$ :  $\Gamma_f(t) = \begin{cases} 0, & t < \tau_f \\ \Gamma_f^k, & t \geq \tau_f \end{cases}$  (6.4)

- An exponential in-growth function:  $\Gamma_f(t) = \Gamma_f^k \cdot \{1 - \exp(-t/\tau)\}$  (6.5)

where  $\tau = \tau_f/2.3$ ,  $\tau_f$  is the transient time and  $\Gamma_f^K$  is the Bohr-Wheeler fission width of equation (6.2), multiplied by the Kramers factor  $K$  of equation (2.9). The ablation stage of ABRABLA has been modified to implement the in-growth functions given by equations (6.4) and (6.5), avoiding several further approximations applied in previous formulations [BuH91, RaM91, BaB93, IgK95]. A detailed description on how these two functions have been incorporated can be found in Appendixes A1.1 and A1.2. The questions, how well each approximation does reproduce the  $\Gamma_f(t)$  that results from solving the FPE, how accurate is their implementation in the theoretical codes and how the approximations influence the final result will be addressed in this section.

### 6.2.1. Critical view on the exponential like in-growth function

The exponential-like in-growth function, equation (6.5), is one of the most commonly used approximations for the time-dependent fission width  $\Gamma_f(t)$ . However, this representation does not

reproduce the behaviour of  $\Gamma_f(t)$  predicted when solving the FPE. This will become clear after the following considerations. In reference [GrJ83] the time-dependent fission width is defined as

$$\Gamma_f(t) = \hbar \lambda_f = \hbar \frac{\int v W(x=x_b, v, t) dv}{\int_{-\infty}^{x_b} \int_{-\infty}^{+\infty} W(x, v, t) dv dx} \quad (6.6)$$

Here  $\lambda_f$  is the fission rate,  $x_b$  is the deformation at the barrier,  $v$  is the velocity ( $v = \frac{dx}{dt}$ ) and  $W$  is the probability distribution. The denominator measures the part of the probability distribution still caught inside the fission barrier. Due to the flux over the fission barrier, the value gradually decreases.

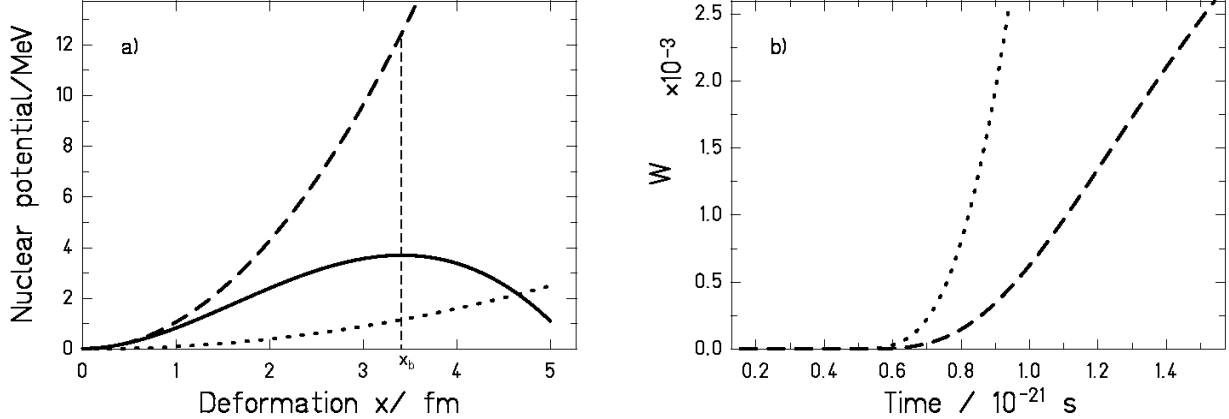


**Figure 6.1:** a) Nuclear potential as a function of deformation, the minimum at zero deformation corresponds to the ground state. The full line represents the nuclear potential chosen in reference [BhG86] ( $U = 8.61 \cdot 10^{-3}(x-3.41)^2 \cdot [(x-23.098)(x+1.59)] + 3.7$ ) for a nucleus with mass  $A = 248$ . Using the reduced mass  $A/4$  [BhG86] leads to the ground-state frequency  $\omega_1 = 1.83 \cdot 10^{21} \text{ s}^{-1}$  in the harmonic approximation, and the maximum reproduces the fission barrier at deformation  $x_b$  with a frequency  $\omega_o = 1.65 \cdot 10^{21} \text{ s}^{-1}$  of the inverted parabolic potential. The dashed line is a parabola with the same ground-state frequency  $\omega_1 = 1.83 \cdot 10^{21} \text{ s}^{-1}$ , and the dotted line is a parabola with the strongly reduced ground-state frequency  $\omega_1 = 0.55 \cdot 10^{21} \text{ s}^{-1}$  for the same nucleus. b) Probability  $W(x=x_b, t)$  defined in equation (6.7) evaluated at the deformation  $x_b$  as a function of time for the two parabolic potentials plotted on the left. The other parameters used in both calculations are also chosen as in reference [BhG86], i.e.,  $\beta = 5 \cdot 10^{21} \text{ s}^{-1}$ ,  $T = 3 \text{ MeV}$ ,  $A = 248$  and reduced mass  $A/4$ . The dashed line is the solution of the FPE when the nuclear potential is approximated by the dashed line on figure 6.1a). The dotted line is the solution of the FPE when using the potential represented by the dotted line on figure 6.1a).

According to the initial conditions assumed, at the beginning of the sequential deexcitation process, the probability distribution can be represented by a very narrow Gaussian centred at the ground-state deformation (see below). As was already discussed by Grangé and Weidenmüller, part of the intrinsic excitation energy is first transferred to the fission collective degree of

freedom. After a certain time that depends on the value of  $\beta$ , this energy saturates, and the probability distribution broadens, populating the deformation space and eventually reaching the fission-barrier deformation  $x_b$ . We explicitly investigate the time evolution of the probability  $W(x = x_b, t)$  at the barrier deformation  $x_b$  in figure 6.1. Where  $W(x = x_b, t)$  is defined as

$$W(x = x_b, t) = \int_{-\infty}^{+\infty} W(x = x_b, v, t) dv \quad (6.7)$$

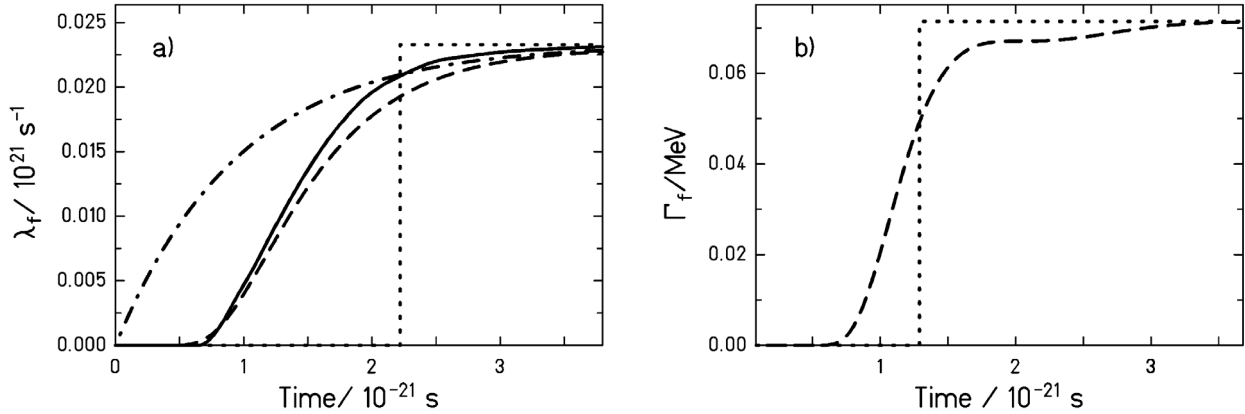


**Figure 6.2:** a) Fission rate  $\lambda_f(t) = \Gamma_f(t)/\hbar$  as a function of time for  $\beta = 5 \cdot 10^{21} \text{ s}^{-1}$ ,  $T = 3 \text{ MeV}$  and  $A = 248$ . The full line is the numerical solution of the FPE taken from reference [BhG86]. The nuclear potential used in this calculation is represented by the full line on figure 6.1a). The dashed line is calculated using equation (6.21) with  $W^{par}(x = x_b, t)$  taken from equations (6.8) and (6.9). The dotted line corresponds to  $\lambda_f(t)$  given by the step function according to equation (6.4), and the dashed-dotted line corresponds to  $\lambda_f(t)$  given by the exponential-like function described by equation (6.5), both calculated with parameters leading to the same transient time as the full calculation. b) Fission width as a function of time for  $\beta = 2 \cdot 10^{21} \text{ s}^{-1}$ , the rest of the parameters are as in part a). The dashed line is calculated using equation (6.21) with  $W^{par}(x = x_b, t)$  taken from equations (6.8) and (6.9). The dotted line corresponds to  $\Gamma_f(t)$  given by equation (6.4).

First, we evaluate the probability distribution  $W(x = x_b, t)$  at the deformation  $x_b$  as a function of time by solving the FPE [Cha43] when the nuclear potential is approximated by the parabola represented by the dashed line of figure 6.1a). The deformation  $x_b$  is defined as well in figure 6.1a). The solution of  $W(x = x_b, t)$  is shown by the dashed line in figure 6.1b). Although this solution of the FPE is obtained for the parabolic potential, the total suppression of the probability distribution at the fission barrier for the initial part of the deexcitation process also results for a more realistic potential. In fact, this feature is independent of the shape of the nuclear potential. This is confirmed by the dotted line of figure 6.1b) that depicts the solution of the FPE for  $W(x = x_b, t)$  with the very shallow parabolic potential represented by the dotted curve on figure 6.1a). One might have expected that a flat potential would lead to an instantaneous spread of the probability distribution up to the saddle deformation. However, the dotted line of figure 6.1b) shows that the probability distribution at  $x_b$  starts differing from zero only after some time. Indeed, the probability  $W(x = x_b, t)$  remains essentially zero up to  $t \approx 0.6 \cdot 10^{-21} \text{ s}$  in both cases, for the shallow and for the deep parabola. According to equation (6.6), the fission width will vanish

when the probability  $W(x = x_b, t)$  vanishes. Hence, independently of the nuclear potential,  $\Gamma_f(t)$  should be zero and have a zero slope at the initial time. This can be observed as well in figure 6.2a), where the numerical solution of the FPE obtained in reference [BhG86] for the fission rate  $\lambda_f(t) = \Gamma_f(t)/\hbar$  is compared with the exponential in-growth function and the step function. This picture shows that the exponential function starts with a very steep slope contradicting the previous requirement of complete suppression at the initial time. On the other hand, the step function reproduces the hindrance of fission at the beginning of the process but it overestimates its duration. In our opinion, this fact could be improved by opening the fission channel by the step function at the time in which the fission probability of the exact solution has reached around 50% of its stationary value or even lower, instead of the standard value of 90%, introduced in reference [BhG86] (section 2.3). Indeed, we will see later that the onset of the fission width is of particular importance.

It is worthwhile to have a closer look on the case of a parabolic potential, where an analytic solution of the Fokker-Planck equation is available. The solution of the Fokker-Planck equation for  $W(x = x_b, t)$  with a nuclear potential approximated by a parabola [Cha43], assuming zero mean deformation and zero mean velocity as initial conditions, is given by the function

$$W^{par}(x = x_b, t) = \frac{1}{\sqrt{2\pi}\sigma} \cdot \exp\left(-\frac{x_b^2}{2\sigma^2}\right) \quad (6.8)$$

where  $\sigma^2$  is a time-dependent function of the form:

$$\sigma^2 = \frac{kT}{\mu\omega_1^2} \left\{ 1 - \exp(-\beta \cdot t) \cdot \left[ \frac{2\beta^2}{\beta_1^2} \sinh^2\left(\frac{1}{2}\beta_1 t\right) + \frac{\beta}{\beta_1} \sinh(\beta_1 t) + 1 \right] \right\} \quad (6.9)$$

where  $k$  is Boltzmann's constant,  $T$  is the nuclear temperature,  $\mu$  is the reduced mass associated to the deformation degree of freedom,  $\omega_1$  describes the curvature of the potential at the ground state and  $\beta_1 = (\beta^2 - 4\omega_1^2)^{1/2}$ . One should notice that, due to the classical nature of the FPE equation, the initial behaviour predicted by this solution should not be considered since for  $t = 0$  equation (6.9) leads to  $\sigma = 0$ . We know from quantum mechanics that for a harmonic oscillator in the ground state, the initial probability distribution as a function of the position and the momentum coordinate has a finite width. In addition, statistical fluctuations yield as well a non-zero initial width contradicting equation (6.9). The treatment of the initial width of the probability distribution is described in detail in the next section. Nevertheless, this fact does not modify our critics to equation (6.5) because, as will be shown later, its only effect is to reduce slightly the time the probability distribution  $W$  needs to reach the barrier deformation  $x_b$  (for example, for the case illustrated in figure 6.2 this time is  $\approx 0.15 \cdot 10^{-21}$  s). The former effect is already included in the calculations shown in figures 6.1b) and 6.2.

The physical meaning of function (6.9) can be better understood when we consider large times and  $\beta$  in the overdamped regime ( $\beta \gg 2\omega_1$ ). Under these conditions, we can neglect the terms  $\exp(-\beta_1 t)$ , and  $\beta_1$  can be approximated by  $\beta_1 \approx \beta - 2\omega_1^2/\beta$ . With this, expression (6.9) turns to:

$$\sigma^2 \approx \frac{kT}{\mu\omega_1^2} \left\{ 1 - \frac{1}{2} \left[ \frac{\beta^2}{\beta_1^2} + \frac{\beta}{\beta_1} \right] \cdot \exp \left( -\frac{2\omega_1^2}{\beta} \cdot t \right) \right\} \quad (6.10)$$

whereby the negative values at small times should be replaced by zero. Using the further approximation  $\beta_1 \approx \beta$  in the preexponential factor, we obtain

$$\sigma^2 \approx \frac{kT}{\mu\omega_1^2} \left\{ 1 - \exp \left( -\frac{2\omega_1^2}{\beta} \cdot t \right) \right\} \quad (6.11)$$

Actually, equation (6.12) is already quantitatively very similar to (6.9) for  $\beta \geq 5 \cdot 10^{21} \text{ s}^{-1}$ . Equation (6.12) shows that the process of the population of the deformation space can be described by a probability distribution with the shape of a Gaussian whose second moment exponentially approaches the asymptotic value. This fact might have misled some authors to introduce an exponential like in-growth function to picture the variation of the fission width with time. We would like to stress here that it is the second moment of the probability distribution that approximately grows like  $1 - \exp(-t/\tau)$  and not the fission width itself.

### 6.2.2. New analytical description for $\Gamma_f(t)$

In view of the conclusions drawn in the previous section, to obtain reliable information on the value of the dissipation coefficient  $\beta$  it appears necessary to develop a more realistic description of the in-growth function governing the onset of the fission process. We present here an analytical approximation for  $\Gamma_f(t)$ . It is based on the fact that the time evolution of the fission decay width is mainly determined by the time evolution of the amplitude of the probability distribution at the barrier deformation  $W(x = x_b, t)$  defined by equation (6.7).

In the overdamped regime, an analytical approximation has been proposed previously [BhG86]. In this regime  $W(x, v, t)$  equilibrates in velocity very fast. Under these conditions, the FPE transforms into the Smoluchowski equation [Ris89].

$$\frac{\partial}{\partial t} W(x, t) = \beta^{-1} \frac{\partial}{\partial x} \left[ \mu^{-1} \frac{dU}{dx} W(x, t) \right] + \varepsilon \beta^{-2} \frac{\partial^2}{\partial x^2} W(x, t) \quad (6.12)$$

where  $\mu$  is the reduced mass,  $U(x)$  is the nuclear potential and  $\varepsilon = \beta kT/\mu$  is the diffusion constant. The analytical approximate solution to this equation for a realistic potential presented in reference [BhG86] is valid for  $t > \beta/2\omega_1^2$ . However, for short times, where the dissipation has a decisive effect on the deexcitation process, this solution does not fulfil the requirement to vanish for a certain time. For this reason, we propose the following more appropriate alternative to this formulation.

In the following we will describe various steps to derive a very convenient expression for the fission decay width, whose definition is given by equation (6.6). We start by defining the normalised probability distribution  $W_n(x = x_b, v, t)$  for any fixed value of  $x_b$  as:

$$W_n(x = x_b, v, t) = \frac{W(x = x_b, v, t)}{\int_{-\infty}^{x_b} \int_{-\infty}^{+\infty} W(x, v, t) dv dx} \quad (6.13)$$

Considering equation (6.13), the fission width of equation (6.6), can be reformulated as follows:

$$\Gamma_f(t) = \hbar \int_{-\infty}^{+\infty} v W_n(x = x_b, v, t) dv \quad (6.14)$$

In the stationary case we get:

$$\Gamma_f(t \rightarrow \infty) = \hbar \int_{-\infty}^{+\infty} v W_n(x = x_b, v, t \rightarrow \infty) dv = \Gamma_f^K \quad (6.15)$$

Finally, combining equations (6.14) and (6.15) we can reformulate the time-dependent fission width defined by equation (6.6) as:

$$\Gamma_f(t) = \frac{\int_{-\infty}^{+\infty} v W_n(x = x_b, v, t) dv}{\int_{-\infty}^{+\infty} v W_n(x = x_b, v, t \rightarrow \infty) dv} \Gamma_f^K \quad (6.16)$$

At this point we introduce the two approximations that lead to a new description for the time-dependent fission width. The first approximation is to consider that:

$$W_n(x = x_b, v, t) \approx C(t) \cdot W_n(x = x_b, v, t \rightarrow \infty) \quad (6.17)$$

where  $C(t)$  is a value that only depends on time. This assumption implies that the shape of the probability distribution at the barrier deformation as a function of the velocity  $v$  is constant and only its height varies with time. This statement is valid in the overdamped motion were the equilibrium in velocity is established very rapidly. We think however, that expression (6.17) is still applicable outside the overdamped regime because, since  $x_b$  is far away from the initial deformation, the time needed for the probability distribution  $W$  to reach the fission barrier is large enough for the velocity to equilibrate. Thus, by the time when  $W_n(x = x_b, v, t)$  starts to differ from zero, the probability distribution as a function of the velocity coordinate has already attained the asymptotic shape  $W_n(x = x_b, v, t \rightarrow \infty)$ . Integrating equation (6.17) over the whole velocity interval we have:

$$C(t) = \frac{\int_{-\infty}^{+\infty} W_n(x = x_b, v, t) dv}{\int_{-\infty}^{+\infty} W_n(x, v, t \rightarrow \infty) dv} = \frac{W_n(x = x_b, t)}{W_n(x = x_b, t \rightarrow \infty)} \quad (6.18)$$

Introducing equation (6.17) in equation (6.16) and using equation (6.18) leads to:

$$\Gamma_f(t) \approx \frac{W_n(x = x_b, t)}{W_n(x = x_b, t \rightarrow \infty)} \Gamma_f^K \quad (6.19)$$

The second approximation consists on expressing the shape of the in-growth function at the fission barrier  $W_n(x = x_b, t)$  by equations (6.8) and (6.9), derived for the parabolic potential:

$$\Gamma_f(t) = \hbar \lambda_f \approx \frac{W^{par}(x = x_b, t)}{W^{par}(x = x_b, t \rightarrow \infty)} \cdot \Gamma_f^K \quad (6.20)$$

Note, that one may replace the normalised probability  $W_n$  by the unnormalised quantity  $W$  in equation (6.20), because in the case of the parabolic potential the probability distribution is confined.

Implementing equations (6.8) and (6.9) in equation (6.20) results in an analytical expression for  $\Gamma_f(t)$ . As initial condition of the problem we have chosen the zero-point motion at the ground-state deformation, which is adequate to the reactions we consider. The zero-point motion is taken into account by shifting the time scale by a certain amount  $t_0$ : For the under-damped case ( $\beta < 2\omega_l$ ), the deformation and the momentum coordinate saturate at about the same time. Therefore, the time shift needed for the probability distribution to reach the width of the zero-point motion in deformation space is equal to the time that the average energy of the collective degree of freedom needs to reach the value  $\frac{1}{2}\hbar\omega_l$  associated to the zero-point motion:

$$t_0^{under} = \frac{1}{\beta} \ln \left( \frac{2T}{2T - \hbar\omega_l} \right) \quad (6.21)$$

In the over-damped regime ( $\beta \geq 2\omega_l$ ), the momentum coordinate saturates very fast, while the population of the deformation space is a diffusion process. Neglecting the influence of the potential on the diffusion process, which is anyhow small in the range of the zero-point motion, the solution of the Fokker-Planck equation gives the following time evolution for the variance of the probability distribution in the deformation coordinate [Cha43]:

$$\sigma_x^2(t) = \frac{2T}{\mu\beta} t \quad (6.22)$$

Replacing in equation (6.22)  $\sigma_x^2(t)$  by the value of the variance associated to the zero-point motion  $\frac{\hbar}{2\mu\omega_l}$  it results:

$$t_0^{over} = \frac{\hbar\beta}{4\omega_l T} \quad (6.23)$$

The analytical expression that results from combining equation (6.20) with equations (6.8) and (6.9) represents a very adequate description of  $\Gamma_f(t)$  as can be seen in figure 6.2a), where this function (dashed line) is compared to the numerical calculation (full line). Moreover, reference [JuS02] demonstrates that this approximation quite well reproduces the exact solution of the FPE for the critical damping and the underdamped regime, as well. For a given value of  $\beta$  and  $T$ , the time behaviour of the exact solution of the FPE is mainly governed by two parameters: the frequency  $\omega_l$  at the ground state and the barrier deformation  $x_b$ . The formulation we present here uses realistic values of  $\omega_l$  and  $x_b$  in the harmonic approximation, whereas the absolute height is taken from Kramers stationary solution for the realistic potential shape (full line in figure 6.1a). This explains the good agreement of this formulation with the numerical calculation. An additional justification for the use of the probability distribution that results from approximating the nuclear potential by a parabola is that, as will be demonstrated later, the most important effect of dissipation is given by the initial suppression of the fission width. Figure 6.2 shows that this suppression is very well reproduced by the new analytical description. The approximation for  $\Gamma_f(t)$  represented by equation (6.20) is suited to be used in complex nuclear-reaction codes, where solving the Fokker-Planck equation numerically would introduce a not affordable additional computing time. Appendix A.3 illustrates how this new approximation for  $\Gamma_f(t)$  has been incorporated in ABRABLA.

### 6.3. Comparison of the experimental data with model calculations

To illustrate how the deduced value of the reduced dissipation coefficient  $\beta$  depends on the description used for the time-dependent fission width, we will consider the total nuclear fission cross section of the reaction of  $^{238}\text{U}$  at  $1\cdot4$  GeV on lead. The nuclear fission cross section has been obtained subtracting from the experimental total fission cross section determined in section 5.1 the electromagnetic contribution given by Rubehn et al. [RuB96]. In table 6.1 the experimental value of this cross section is compared with the values obtained from several ABRABLA calculations performed with various options. Different shapes of the time-dependent fission width and different values of  $\beta$  were used. In addition, for part of the calculations the break-up stage of the model calculation was not included. Though this is unphysical, it serves to distinguish between the effects of dissipation and the effects of the break-up process on fission at high excitation energies. In this section we will only consider the calculations performed including break-up to describe the intermediate stage between the abrasion and the statistical evaporation at initial temperatures larger than 5.5 MeV. As the values of the third row of table 6.1 show, the transition-state model [BoW39] clearly overestimates the experimental data. In fact, the experimental cross sections are only reproduced when dissipative effects are included in the calculation. However, the choice of the in-growth function for  $\Gamma_f(t)$  according to equations (6.4) or (6.5) has a strong influence on the dissipation coefficient deduced. While the calculation with the description given by equation (6.4) (step function) reproduces the data with a value of  $\beta = 2 \cdot 10^{21} \text{ s}^{-1}$ , the same value of  $\beta$  with equation (6.5) (exponential like in-growth) overestimates the cross sections. The reason is that, in the case of the exponential like function, fission is already possible with a considerable probability at the very beginning of the deexcitation process. To reproduce the data when the exponential-like in-growth function is used, a larger value of the reduced dissipation coefficient  $\beta = 4 \cdot 10^{21} \text{ s}^{-1}$  is required that diminishes the asymptotic value of the fission width and enlarges the transient time. As expected, when this value of  $\beta$  is used with the step function, the cross sections are underestimated. The last row of table 6.1 illustrates that, to explain the experimental cross section with the highly realistic description of the fission width

based on the analytical solution of the FPE introduced in section 6.2.2, a value of  $\beta = 2 \cdot 10^{21} \text{ s}^{-1}$  is required in agreement with the step function.

Experimental Data	$2.16 \pm 0.14 \text{ b}$	
Calculation	No Break-up	Break-up
Transition-State Model	5.61 b	3.33 b
$\Gamma_f(t) \text{ step}$ $\beta = 2 \cdot 10^{21} \text{ s}^{-1}$	2.17 b	2.00 b
$\Gamma_f(t) \text{ step}$ $\beta = 4 \cdot 10^{21} \text{ s}^{-1}$	1.58 b	1.54 b
$\Gamma_f(t) \sim 1 - \exp(-t/\tau)$ $\beta = 2 \cdot 10^{21} \text{ s}^{-1}$	4.98 b	2.52 b
$\Gamma_f(t) \sim 1 - \exp(-t/\tau)$ $\beta = 4 \cdot 10^{21} \text{ s}^{-1}$	4.40 b	2.04 b
$\Gamma_f(t) \text{ FPE}$ $\beta = 2 \cdot 10^{21} \text{ s}^{-1}$	2.55 b	2.09 b

**Table 6.1:** Experimental total nuclear fission cross-sections of  $^{238}\text{U}(1 \text{ A GeV})$  on lead compared with different calculations performed with the code ABRABLA. Each calculation has been performed twice. In one case, the simultaneous break-up stage is not included in the calculation, so that no limit for the initial temperature of the evaporation cascade is imposed. In the other case, the break-up model imposes an upper limit of 5.5 MeV to the initial temperature of the evaporation cascade. A first set of calculations was performed with the transition-state model [BoW39]. The other calculations were performed with different descriptions of  $\Gamma_f(t)$  and different values of  $\beta$ . The last calculation was performed with  $\Gamma_f(t)$  as the analytical solution of the FPE given by equation (6.20) with  $W^{par}(x = x_b, t)$  taken from equations (6.8) and (6.9).

As discussed in section 6.2.1, there exist solid theoretical arguments why the exponential like in-growth function of equation (6.5) does not reproduce correctly the increase of the fission width as a function of time. It is to expect that this function is not able to describe properly the experimental data. However, table 6.1 shows that the total nuclear fission cross sections of  $^{238}\text{U}$  (1 GeV) + Pb can be reproduced well by all the descriptions for  $\Gamma_f(t)$  provided that the appropriate value of  $\beta$  is used. This means that we need additional observables that allow tagging the fission events according to the excitation energy. For the largest excitation energies, the exponential in-growth function should differ from the measured data. This selection according to the excitation energy can be achieved by considering the charge sum of the fission fragments  $Z_1+Z_2$ . We already discussed in section 4.3 that the excitation energy of the systems before entering the sequential decay is likely to increase with decreasing  $Z_1+Z_2$ . However, one has to consider as well that very excited prefragments undergo a simultaneous break-up that sets a limit of 5.5 MeV to the temperature of the fissioning nucleus. Thus, one could suspect that for the lightest fissioning nuclei the excitation energy remains constant or even decreases. To clarify the situation we performed a calculation with ABRABLA that gives the excitation energy of the

system right before entering the ablation stage as a function of  $Z_1+Z_2$ . The result for the carbon<sup>5</sup> target is displayed in figure 6.3. It can be seen that, initially, the excitation energy increases with decreasing  $Z_1+Z_2$ , from  $Z_1+Z_2 \approx 78$  to  $Z_1+Z_2 \approx 73$  it remains more or less constant with a mean value of approximately 550 MeV and finally it slowly decreases. Thus, in spite of the simultaneous break-up, the lowest values of  $Z_1+Z_2$  are related to excitation energies that are high enough for the statistical decay time to be considerably shorter than the transient time  $\tau_f$ .

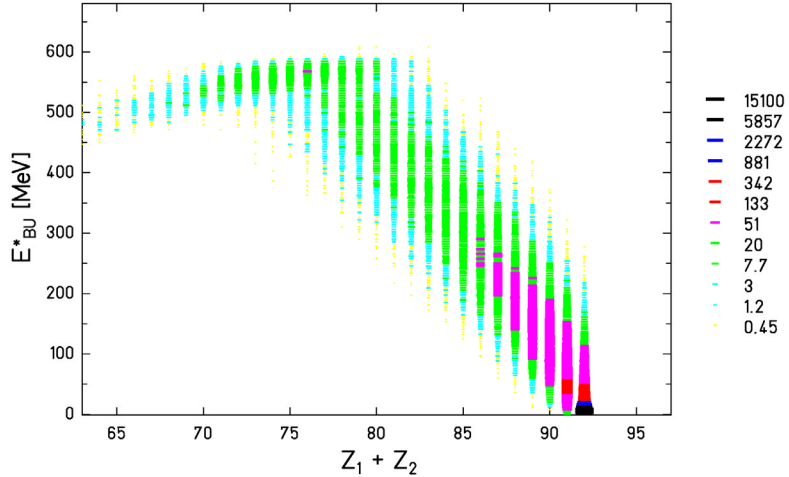


**Figure 6.3:** Calculation performed with ABRABLA representing the excitation energy of the prefragment right before entering the ablation stage as a function of the sum charge of the fission fragments. The reaction considered is  $^{238}\text{U}$  (1 AGeV) + C.

Figure 6.4 shows the experimental partial fission cross sections and the widths of the charge distributions for the reaction  $^{238}\text{U}$  (1 A GeV) +  $(\text{CH}_2)_n$ . The experimental data (full dots) are compared with three ABRABLA calculations. In these calculations, the contribution given by the hydrogen part of the  $(\text{CH}_2)_n$  target has been determined according to a fast simplified version of CASCABLA [CuV97, JuJ98, EnW01]. The dashed line is the result of using the exponential-like function and  $\beta = 4 \cdot 10^{21} \text{ s}^{-1}$ , the dotted line is performed with the step function (equation (6.4)) and  $\beta = 2 \cdot 10^{21} \text{ s}^{-1}$ , and the full line corresponds to a calculation with the analytical expression for  $\Gamma_f(t)$  introduced in section 6.2.2 and  $\beta = 2 \cdot 10^{21} \text{ s}^{-1}$ . For both observables, the calculation performed with the fission width derived from the analytical solution of the FPE and the calculation that employs the step function almost coincide over the whole  $Z_1+Z_2$  interval. Moreover, in the case of figure 6.4a), the three calculations agree quite well with each other and with the experimental data for the highest values of  $Z_1+Z_2$  and start to differ for the lowest values of  $Z_1+Z_2$ . In this part of the spectrum, the exponential-like in-growth function overestimates the experimental partial fission cross sections, while the two other functions underestimate them. A slight reduction of the fission barriers [CaS83] at high excitation energies could eventually account for this deviation. It is not possible to decide from figure 6.4a) which function  $\Gamma_f(t)$  gives the best description of the measured data. However, in contrast to the partial fission cross sections, the comparison of the different calculations with the experimental widths of the charge distributions of the fission fragments depicted in figure 6.4b) indicates a significant disagreement

<sup>5</sup> For the case of the  $(\text{CH}_2)_n$  target, we have to add the effect of the hydrogen part that leads mostly to heavy residues and for which the excitation energy induced per removed nucleon is not 27 MeV as in carbon but approximately 50 MeV. Consequently, the spectrum of the correlation between  $Z_1+Z_2$  and excitation energy for the  $(\text{CH}_2)_n$  target should be somewhat broader (in the  $E^*$  axis) for the largest values of  $Z_1+Z_2$  than the one displayed in figure 6.3.

between the calculation done with the exponential-like description and the measured data. The overprediction of the widths when applying the exponential-like function suggests that this description yields too large excitation energies at saddle. Finally, figure 6.4a) shows that the model calculations clearly overestimate the partial fission cross sections for  $Z_1+Z_2 = 91$  and  $92$ . This disagreement can be due to the combination of several effects. One is the fact that the ABRABLA code overestimates the electromagnetic-induced component of the total fission cross section. Nevertheless, the discrepancy between the calculations and the experimental data in figure 6.4a) cannot be all due to this effect. An additional explanation could be the failure of the Abrasion model in reproducing very peripheral collisions. This strongly depends on the description of the nuclear density distribution used. It has been found that the present description of the abrasion model works well for heavier targets like Cu and Pb but no study has been performed yet on lighter nuclei like Carbon. Finally, another possible reason could be a wrong treatment of the fission probability of nuclei with small fission barriers and a second minimum. For such cases the Bohr-Wheeler model used in ABRABLA is too simple. In any case, all these effects are not critical for our purposes because our conclusions are derived from the fission of light nuclei where they have no influence.

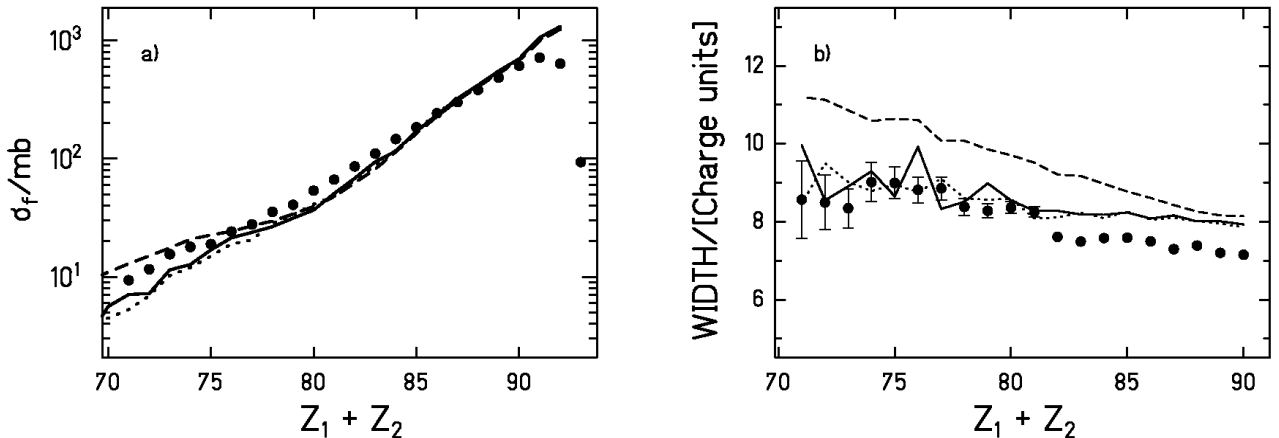


**Figure 6.4:** Experimental partial fission cross sections (full dots part a) and widths of the charge distributions of the fission fragments (full dots part b) obtained for the reaction  $^{238}\text{U}$  (1 A GeV) +  $(\text{CH}_2)_n$  in comparison with various ABRABLA calculations. The dashed lines are calculations performed with the exponential in-growth function (equation (6.5)) and  $\beta = 4 \cdot 10^{21} \text{s}^{-1}$ , the dotted lines are calculations carried out with the step function (equation (6.4)) and  $\beta = 2 \cdot 10^{21} \text{s}^{-1}$ , and the full lines are the result of using equation (6.20) with  $W^{par}(x = x_b, t)$  taken from equations (6.8) and (6.9) and  $\beta = 2 \cdot 10^{21} \text{s}^{-1}$ .

Let us examine now the sensitivity of the experimental observables to the value of the reduced dissipation coefficient  $\beta$ . Due to the above discussed outcomes, the subsequent calculations are performed with the fission width  $\Gamma_f(t)$  that follows from the analytical solution of the FPE introduced in section 6.2.2. In figure 6.5 the same two observables of figure 6.4 are compared with the transition-state model (dashed line) and with several calculations obtained for various values of  $\beta$  representing the three different dissipation regimes. As expected, both observables are visibly overrated by the transition-state model confirming their sensitivity to dissipation. For the partial fission cross sections (figure 6.5a) as well as for the widths of the charge distributions (figure 6.5b), the best description is given by the full line that corresponds to  $\beta = 2 \cdot 10^{21} \text{s}^{-1}$ . Such

value of  $\beta$  is equivalent to the shortest transient time  $\tau_f$ , the critical damping. This means that, for the systems studied, the coupling between the collective and the intrinsic degrees of freedom leads to the fastest possible spread of the probability distribution in the deformation space. Any other value of  $\beta$  above or below the critical damping will result in lower cross sections and narrower distributions because the dynamical delay increases, see figure 2.3 of chapter 2. This is indeed what the dotted lines ( $\beta = 0.5 \cdot 10^{21} \text{ s}^{-1}$ ) and the dashed-dotted lines ( $\beta = 5 \cdot 10^{21} \text{ s}^{-1}$ ) of figure 6.5 tell us.

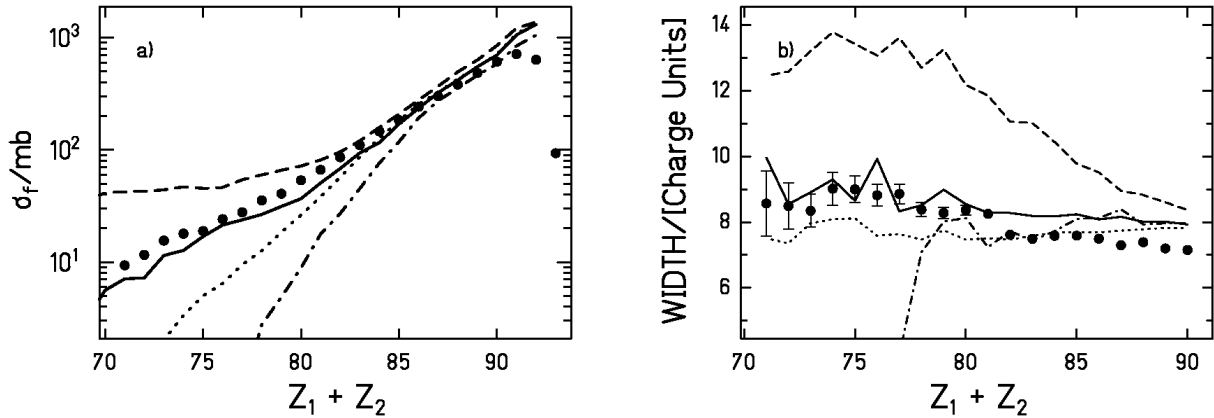


**Figure 6.5:** Experimental partial fission cross sections (full dots part a) and widths of the charge distributions of the fission fragments (full dots part b) obtained for the reaction  $^{238}\text{U}$  (1 A GeV) +  $(\text{CH}_2)_n$  in comparison with various ABRABLA calculations. The dashed lines are calculations according to the transition-state model. The rest of the calculations are performed using equation (6.20) with  $W^{par}(x = x_b, t)$  taken from equations (6.8) and (6.9). The full lines are performed with  $\beta = 2 \cdot 10^{21} \text{ s}^{-1}$ , the dotted lines with  $\beta = 0.5 \cdot 10^{21} \text{ s}^{-1}$  and the dashed-dotted lines with  $\beta = 5 \cdot 10^{21} \text{ s}^{-1}$ .

The dependence of the total nuclear fission cross sections on the charge of the target is portrayed by the full dots in figure 6.6 together with several ABRABLA calculations. The nuclear fission cross sections are obtained subtracting the electromagnetic component as calculated in reference [RuB96] from the total fission cross sections determined in the previous chapter. Since the total reaction probability increases with the mass of the target, one would expect that the fission cross sections grow with the charge of the target. However, figure 6.6 shows that the nuclear fission cross section for carbon is smaller than the one for hydrogen. As before, the calculation based on the transition-state model (dashed line) overestimates the cross sections and does not reproduce the minimum of the cross section for  $Z_{target} = 6$ . Although none of the calculations that include dissipation provide a good quantitative description of all the cross sections, the existence of this minimum is only reproduced when dissipation is considered. We think that the failure to reproduce the target dependence of the cross sections is due to a malfunction of the abrasion model that was commented before and that was already observed by Rubehn et al. [RuB96]. Nevertheless, the fact that the minimum of the cross section is found for the carbon target and not for the hydrogen has its explanation in dissipation. The fragmentation of  $^{238}\text{U}$  at 1 A GeV on hydrogen leads principally to the production of heavy projectile-like residues with low excitation energies and low fission barriers. These nuclei are not sensitive to the dynamical delay induced by dissipation and most of them fission. On the other hand, when the  $^{238}\text{U}$  projectiles at 1 A GeV react with a carbon target, the number of heavy projectile-like products decreases and the residue

distribution extends to lighter nuclei with higher excitation energies and higher fission barriers. If there would be no dynamical delay, a great part of these nuclei would fission, and the total fission cross section would increase with respect to the hydrogen case. However, if dissipation is considered, the statistical decay time of these lighter nuclei is shorter than the dynamical delay and fission is suppressed leading to lower cross sections.

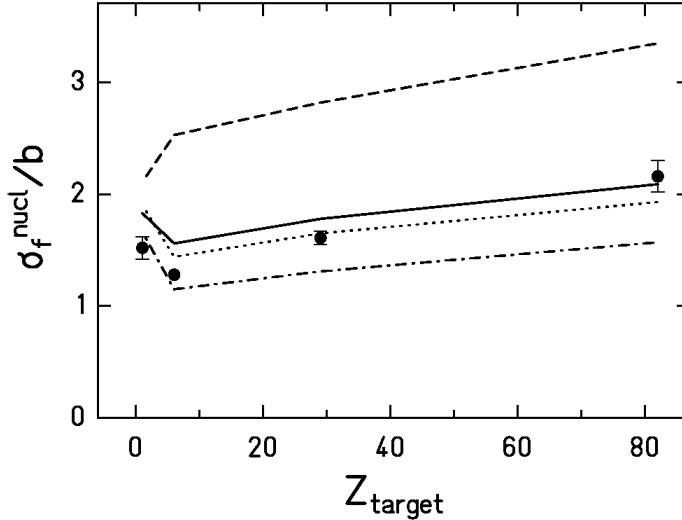


**Figure 6.6:** Total nuclear fission cross sections of  $^{238}\text{U}$  (1 A GeV) as a function of the target charge. The experimental data are represented by the full dots. The dashed line is a calculation according to the transition-state model. The rest of the calculations are performed using equation (6.20) with  $W(x = x_b, t)$  taken from equations (6.8) and (6.9). The full line corresponds to  $\beta = 2 \cdot 10^{21} \text{ s}^{-1}$ , the dotted line corresponds to  $\beta = 0.5 \cdot 10^{21} \text{ s}^{-1}$  and the dashed-dotted line to  $\beta = 5 \cdot 10^{21} \text{ s}^{-1}$ .

## 6.4. Discussion

It is very illustrative to compare how the excitation energy with which the nucleus crosses the saddle point changes in the model calculation when using the different approximations for describing  $\Gamma_f(t)$ . Figure 6.7 depicts the excitation energy of the nucleus at the saddle point against the initial excitation energy of the prefragment right after the abrasion process for the fission events produced in the reaction of  $^{238}\text{U}$  at 1 A GeV in a lead target. The pictures in the left-hand side column of figure 6.7 correspond to the unrealistic case, where there is no upper limit for the initial temperature of the sequential decay. Calculation 6.7a) corresponds to the step-function description with  $\beta = 2 \cdot 10^{21} \text{ s}^{-1}$ , calculation 6.7b) to the exponential-like description with  $\beta = 4 \cdot 10^{21} \text{ s}^{-1}$ , and 6.7c) to the analytical solution of the FPE with a parabolic nuclear potential and  $\beta = 2 \cdot 10^{21} \text{ s}^{-1}$ . The same set of calculations but including the break-up stage is shown in the right-hand side column of figure 6.7. By comparing both sides of figure 6.7, one immediately recognizes that the effect of the break-up process on the calculation performed with the exponential-like description for  $\Gamma_f(t)$  is much more drastic than for the two other calculations. The too early onset of fission introduced by the exponential-like in-growth function implies that fission at high excitation energies is not suppressed by dissipation. Fission reaches to such high excitation energies, that it is rather constricted by the break-up mechanism. On the contrary, the calculations performed with the step function and with the analytical solution of the FPE

illustrate that dissipation considerably inhibits the fission decay channel for excitation energies at fission above 350 MeV and, therefore, the effect of the break-up process is significantly smaller. Figure 6.2b) shows that for the analytical solution of the FPE the fission probability sets in earlier than for the step function, leading to a larger amount of fissioning systems with initial excitation energies  $E_0^*$  beyond 800 MeV, as can be seen comparing figures 6.7a) and 6.7c). As a result, the break-up stage has a stronger effect in this case than in the case of the step function.

The influence of the simultaneous break-up on the deexcitation process can also be observed from the cross sections of table 6.1. When the exponential-like description of  $\Gamma_f(t)$  is used, the calculated cross sections differ considerably, depending on whether the break-up stage is included or not in the calculation. In contrast, the calculated cross sections obtained by applying the analytical solution of the FPE do not present such a remarkable difference, and the ones calculated using the step function are hardly affected by this feature.

The 45-degree straight lines depicted on the six spectra of figure 6.7 correspond to the upper limit for the excitation energy at fission. Both, the calculation performed with the step function on figure 6.7a) and the calculation with the analytical solution of the FPE on figure 6.7c) show that this line starts to be depopulated at initial excitation energies of approximately 150 MeV, indicating that from these excitation energies on the transient time is longer than the decay time for particle emission. That means that prefragments with initial excitation energies higher than approximately 150 MeV can only fission after cooling down by particle evaporation.

The previous discussion has shown that, although the step function described by equation (6.4) appears to be a rather crude approximation, it better describes the effects of dissipation on the fission decay width than the exponential-like function of equation (6.5). It also leads to a strong suppression of fission at high excitation energies in quite good agreement with the more realistic description of the fission width given by the analytical solution of the FPE for a parabolic nuclear potential. However, due to the possible existence of fission events at very high excitation energies (especially in the case of the exponential-like description of  $\Gamma_f(t)$ ) any conclusion on dissipation would strongly depend on the thermal stability of nuclei against break-up. When the step function is used, the experimental data selected are reproduced with a reduced dissipation coefficient of  $\beta = 2 \cdot 10^{21} \text{ s}^{-1}$ . The same value of  $\beta = 2 \cdot 10^{21} \text{ s}^{-1}$  is obtained when the more realistic description of  $\Gamma_f(t)$  based on the analytic solution of the FPE is applied. From figure 6.2b) one would expect that the analytical solution of the FPE requires a larger value of  $\beta$  to describe the experimental data than the step function, but as was explained before, the break-up mechanism suppresses the additional fission events at high excitation energies and leads to very similar fission cross-sections.

Our investigation does not allow a direct conclusion on the temperature dependence of the dissipation coefficient  $\beta$ , but it reveals the difficulty in deducing such an effect. The different distributions of excitation energies at fission found in the calculations shown in figure 6.7 prove that this analysis strongly depends on the in-growth function assumed for  $\Gamma_f(t)$ . For instance, the inhibition of fission at high excitation energies obtained with the analytical solution and the step function could be achieved with the exponential-like in-growth function as well by setting very high values of  $\beta$  at high temperatures. Therefore, it cannot be excluded that the indications for strong increase of nuclear viscosity with increasing temperature drawn in several publications [HoB95, RuK98] might be attributed to the unrealistic exponential-like in-growth function used in the analysis.

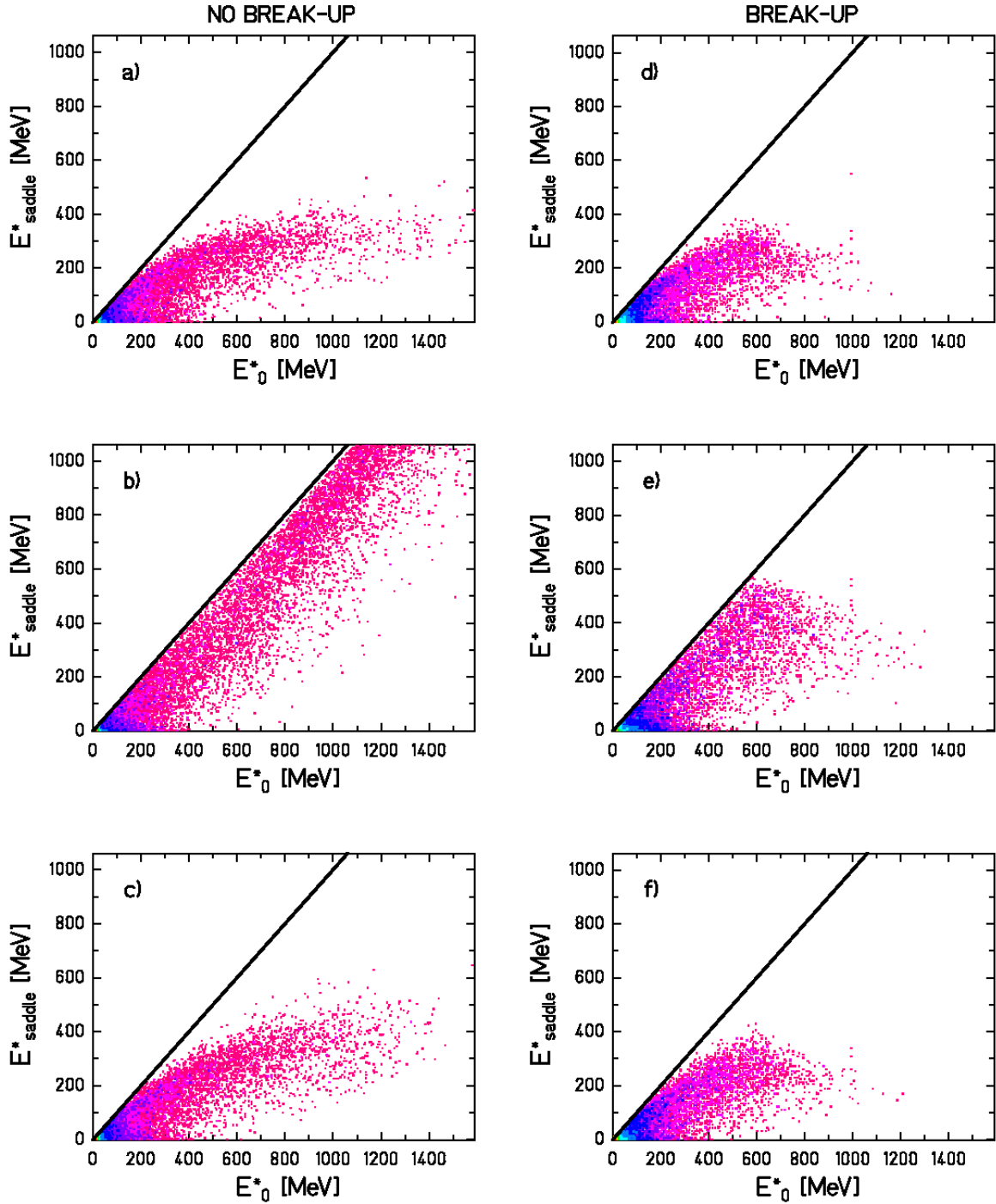


**Figure 6.7:** Calculations performed with ABRABLA representing the excitation energy at fission versus the excitation energy of the prefragment right after the abrasion for the fission events obtained in the reaction of 1 A GeV  $^{238}\text{U}$  on a lead target. The calculations a), b) and c) on the left-hand side are performed without including the break-up stage. The calculations d), e) and f) on the right-hand side are performed including the break-up stage. Calculations a) and d) are performed with  $\Gamma_f(t)$  as a step function and  $\beta = 2 \cdot 10^{21} \text{ s}^{-1}$ . Calculations b) and e) are done with  $\Gamma_f(t) \propto (1 - e^{-t/\tau})$  and  $\beta = 4 \cdot 10^{21} \text{ s}^{-1}$ . Calculations c) and f) are carried out with equation (6.20) taking  $W^{\text{par}}(x = x_b, t)$  from equations (6.8) and (6.9) and  $\beta = 2 \cdot 10^{21} \text{ s}^{-1}$ . In all cases we have used  $\hbar\omega_1 = 1 \text{ MeV}$ . The straight lines represent the upper limit for the excitation energy at fission.

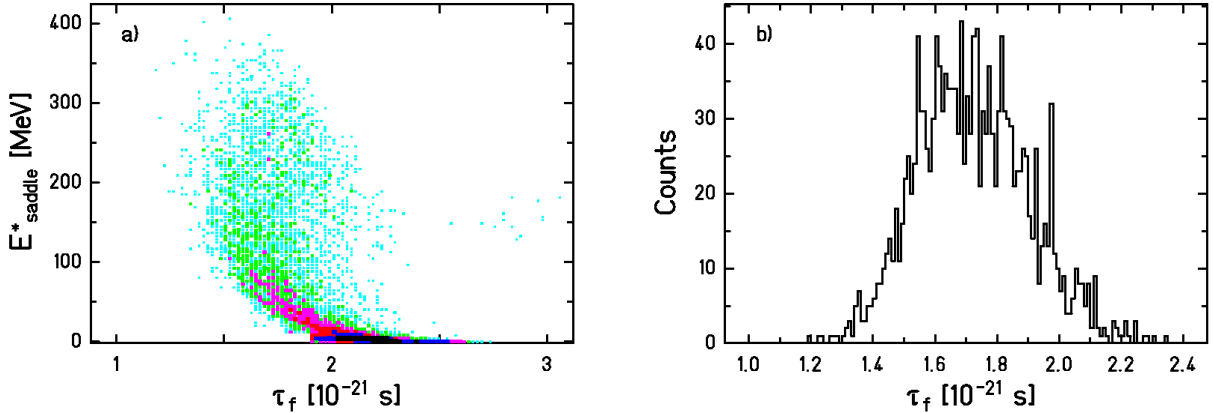


**Figure 6.8:** a) Excitation energy at fission as a function of the transient time  $\tau_f$  calculated according to equation (2.11) of chapter 2 for the reaction  $^{238}\text{U}$  (1 A GeV) + Pb. b) Distribution of transient times corresponding to the fission events with excitation energies at saddle larger than 150 MeV. The calculation has been performed including the break-up stage and using equation (6.20) for  $\Gamma_f(t)$  with  $W^{\text{par}}(x = x_b, t)$  as given by equations (6.8) and (6.9).

The nuclei that contribute to the fission cross section extend over a broad range of masses, charges and excitation energies at the saddle point. Hence, according to equation (2.11) of chapter 2 the deduced value of  $\beta = 2 \cdot 10^{21} \text{ s}^{-1}$  corresponds to a distribution of transient times  $\tau_f$ . In figure 6.8a) the excitation energy of the fissioning nuclei is represented as a function of the transient time  $\tau_f$  determined according to equation (2.11) assuming  $\hbar\omega_1 = 1 \text{ MeV}$  [RaM91]. As discussed below, the description that reproduces our experimental data implies that transient effects are observed only in those nuclei with excitation energies larger than approximately 150 MeV. Therefore, we can only consider the transient time of nuclei with excitation energies at fission above this threshold. Selecting the nuclei with  $E^*_{\text{saddle}} > 150 \text{ MeV}$ , we obtain the distribution of transient times shown in figure 6.8b). A mean value of the transient time of  $\tau \approx (1.7 \pm 0.4) \cdot 10^{-21} \text{ s}$  can be extracted from this curve.

In figure 6.9 the dependence of the mean value of the transient time  $\langle \tau_f \rangle$  (dashed line) with the excitation energy at fission is compared with the same dependence of the average statistical time that the system needs to reach the fission barrier  $\langle \tau_{\text{sta}} \rangle$  (full line). The latter results from the sum of the mean decay time associated to the " $n$ " evaporation steps that occur before fission takes place:

$$\langle \tau_{\text{sta}} \rangle = \sum_i^n \tau_i \quad (6.24)$$

where

$$\frac{1}{\tau^i} = \frac{\Gamma_n^i}{\hbar} + \frac{\Gamma_p^i}{\hbar} + \frac{\Gamma_\alpha^i}{\hbar} + \frac{\Gamma_f^i(t)}{\hbar} \quad (6.25)$$

with  $\Gamma_n$ ,  $\Gamma_p$ ,  $\Gamma_\alpha$  the decay widths for neutron, proton, and alpha emission, respectively.  $\Gamma_f(t)$  is the value of the fission width at the corresponding step. Figure 6.9 shows that, while the transient time depends very weakly on the excitation energy, the statistical time  $\langle\tau_{sta}\rangle$  decreases strongly with the excitation energy. For low excitation energies the statistical time is several orders of magnitude larger than the transient time. At excitation energies above 225 MeV the transient time starts to be larger than the statistical time  $\langle\tau_{sta}\rangle$ .

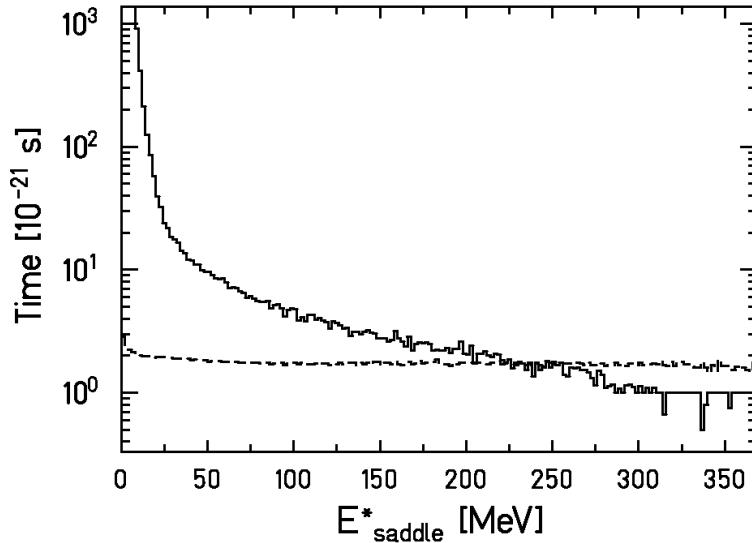


**Figure 6.9:** Calculation representing the average statistical time  $\langle\tau_{sta}\rangle$  for the system to cross the saddle point (full line) as a function of the excitation energy at saddle in comparison with the average transient time  $\langle\tau\rangle$  (dashed line) as a function of the excitation energy at saddle. The calculation corresponds to the reaction  $^{238}\text{U}$  (1 A GeV) + Pb with  $\beta = 2 \cdot 10^{21} \text{ s}^{-1}$ . It includes the break-up stage and  $\Gamma_f(t)$  follows equation (6.20) with  $W^{par}(x = x_b, t)$  as given by equations (6.8) and (6.9).

According to figure 6.3, the break-up process [Ric02, ScR02] limits the maximum value of the excitation energy at the beginning of the evaporation cascade to about 550 MeV. However, the description of  $\Gamma_f(t)$  that reproduces the data is influenced by transient effects only for excitation energies at the fission barrier within the interval  $150 \text{ MeV} < E^*_{\text{saddle}} < 350 \text{ MeV}$ . Out of this excitation energy range, our experimental data are not sensitive to the strength of  $\beta$  since at excitation energies above 350 MeV, fission is almost completely inhibited. Therefore, an eventual increase of the dissipation coefficient for excitation energies larger than 350 MeV would not be observable. At excitation energies below 150 MeV, the statistical decay times are appreciably longer than the dynamical time scale, represented by the transient time, as long as the value of  $\beta$  remains in a certain range defined by  $\tau_f \ll \tau_{sta}$ , making the experimental observables rather insensitive to the transient time. The Kramers factor implies a reduction of the fission width that should have some effect on the measured data at these low excitation energies. Nevertheless, the observation of such effect is much more difficult than the observation of the total suppression of fission by the transient time because it requires a very accurate knowledge of the level density.

As explained already in chapter 3, both the fission cross sections and the widths of the charge distributions of the fission residues are only sensitive to dissipation in the small deformation range from the ground state to the saddle point. The value of  $\beta = 2 \cdot 10^{21} \text{ s}^{-1}$  obtained from our analysis coincides with the value found in reference [BeA02], where total fission cross sections as well as the widths of the charge distributions and velocities of the fission residues from the reaction Au (800·*A* MeV) + p are analysed with the step-function description of  $I_f(t)$ . Other work [HuB00, MoJ95, JiP01], sensitive to the same deformation range, is consistent as well with our values of  $\beta$  and  $\tau_f$ , although often only upper limits for the transient time or the dissipation coefficient could be deduced. Our result for  $\tau_f$  entails that for nuclei with excitation energies lower than 100 MeV the transient time is still a too tiny effect to have observable influence on the fission decay width. Experiments need to populate higher excitation energies in order to be sensitive to dissipation effects on the way to the saddle point.

The quantitative value deduced for the dissipation coefficient remains model dependent to a certain degree. Nevertheless, variations of the most critical model parameters by reasonable amount: excitation energy of the prefragments by 30%, freeze-out temperature by 20 % and excitation-energy reduction per mass loss in the break-up stage by a factor of two led to variations of the deduced transient time well inside the uncertainty range given. The influence of the ratio of the level density parameters  $a_f/a_n$  has been studied in detail in reference [JuH01] showing that the value of  $a_f/a_n$  that better fits our data is the one predicted by Ignatyuk et al [IgI75]. Although the calculations presented in reference [JuH01] do not include the break-up stage, recent calculations show that the conclusions on  $a_f/a_n$  derived in reference [JuH01] are still valid when the break-up process is considered.

## Chapter 7: Conclusion

In the present work, an experimental method suited for the study of dissipation at small deformation has been introduced. According to this approach, fission is induced by peripheral heavy-ion collisions at relativistic energies. The fissioning nuclei produced have small shape distortions and low angular momenta [Jol97]. These initial conditions allow for applying the theoretical model of Grangé and Weidenmüller [GrJ83]. Moreover, the excitation energy induced by the fragmentation of the projectile is very high. This enables to be sensitive to the transient time, which represents a small effect within the small deformation regime. The experimental set-up for fission studies used allowed for determining different observables sensitive to the strength of dissipation from the ground state to the saddle point: The target-charge dependence of the total fission cross sections of  $^{238}\text{U}$  at 1 A GeV, and the partial fission cross sections and the width of the partial charge distributions of the fission fragments for the reaction  $^{238}\text{U}$  at 1 A GeV on  $(\text{CH}_2)_n$ . The sensitivity to dissipation of the two latter observables was investigated for the first time.

Since all our conclusions on dissipation are based on the comparison with a theoretical model, an intense study of the modelling of dissipation effects in nuclear-reaction codes was performed. In particular, we analysed the two most widely used approximations for the time dependence of the fission decay width, a step function and an exponential-like in-growth function. Solid theoretical arguments have been presented that shed severe doubts on the validity of the exponential in-growth function. The steep onset of the fission decay width immanent to this description contradicts the initial suppression of fission that is expected theoretically due to dissipation effects. Since these two approximations seemed to be very crude, we developed a highly realistic description based on the analytical solution of the FPE when the nuclear potential is approximated by a parabola [Cha43]. This new approximation not only reproduces very well the exact solution of the FPE in the overdamped regime but it also gives a rather good description of the time-dependent fission width in the underdamped regime [JuS02].

The experimental observables were compared with an updated version of the Monte-Carlo code ABRABLA [GaS91, JuJ98] where the three different descriptions for the time-dependent fission width mentioned above are included. A comparison of the model calculations with the nuclear fission cross sections of  $^{238}\text{U}$  at 1 A GeV on Pb showed that the deduced dissipation coefficient  $\beta$  depends strongly on whether the step function, the exponential-like in-growth function or the analytical approximation is used. Consequently, in order to interpret any result on the magnitude of  $\beta$ , the description used for the time dependence of the fission width must be specified. Moreover, when comparing with the new observables, it was found that the exponential-like approximation clearly overestimates the width of the charge distributions of the fission fragments. The reason for this discrepancy is the no-suppression of fission at very high excitation energies associated to the exponential-like description. On the contrary, the step-function approximation and the highly realistic description showed a quite similar behaviour in very good agreement with the new experimental observables. This indicates that the inhibition of the fission decay width during the initial time span is needed to account for dissipation effects in a proper way.

Assuming the validity of the analytical solution of the FPE, the transition-state model [BoW39] and several calculations for various values of  $\beta$  performed with ABRABLA were contrasted with the experimental observables. This analysis clearly demonstrated the influence of dissipation on the way to the fission barrier. Neither the charge-target dependence of the total nuclear fission cross sections, nor the partial cross sections and the widths of the charge distributions could be described by the transition-state model. Although the shape of the target dependence could not be quantitatively reproduced with the present version of the abrasion model, the minimum of the cross section at  $Z_{\text{target}} = 6$  could only be explained including dissipation. The best description of the partial fission cross sections and the widths of the charge distributions of the fission fragments was found for  $\beta = 2 \cdot 10^{21} \text{ s}^{-1}$ . This value of  $\beta$  corresponds to the critical damping and leads to the lowest possible transient time with a value of  $\tau_f \approx (1.7 \pm 0.4) \cdot 10^{-21}$ . This result is in agreement with other work [HuB00, MoJ95, JiP01] sensitive to the same deformation range.

The experimental observables are well reproduced assuming that  $\beta$  remains constant with the temperature. It is difficult to draw any conclusion on the temperature dependence of the dissipation coefficient from our measurements because the interval of excitation energies where this dependence can be tested is limited. First, recent experimental results [ScR02] indicate that the maximum excitation energy with which the systems enter the sequential decay where particle evaporation and fission compete is limited to a value of approximately 550 MeV. Additionally, our observables are insensitive to transient effects at excitation energies below 150 MeV and above 350 MeV. For excitation energies lower than 150 MeV the statistical decay time is anyhow significantly larger than the transient time, and for excitation energies larger than 350 MeV the critical damping already suppresses fission completely.

## Appendix: Treatment of fission as a dissipative process in ABRABLA

In this appendix we document in detail how dissipation is described in the evaporation part of the Monte-Carlo code ABRABLA [GaS91, JuJ98]. The main evaporation channels we consider are neutron, proton and alpha-particle emission. Each of these decay modes is represented by a partial decay width  $\Gamma_\nu$ , which is related to the partial lifetime  $\tau_\nu = \hbar / \Gamma_\nu$ . In the following, we distinguish only between two decay channels, particle evaporation, which groups neutron, proton and alpha-particle emission, and fission. The particle-decay mode is represented by the decay width

$$\Gamma_p = \sum_\nu \Gamma_\nu \quad (\text{A1})$$

and the corresponding partial particle decay time  $\tau_p$  is defined by

$$\frac{1}{\tau_p} = \sum \frac{1}{\tau_\nu} \quad (\text{A2})$$

While the particle-decay widths do not explicitly depend on time, dissipation effects lead to a time-dependent fission width  $\Gamma_f(t)$ . Therefore, at the beginning of each step of the deexcitation cascade one has to consider the time elapsed during the previous stages. Physically this means that, while particles are emitted, the probability distribution in deformation space becomes broader, and at each step of the deexcitation cascade the distribution “remembers” its current width. Accordingly, in every step  $n$  we have to evaluate the fission width  $\Gamma_f(t)$  with a time variable whose initial value increases with each step as

$$t_{sum}^n = \sum_i^{n-1} \tau_i \quad (\text{A3})$$

Here  $\tau_i$  represents the average decay time at the corresponding step and includes the mean particle decay time  $\tau_p$  and the mean decay time for fission  $\tau_{fission}$ . If this feature is not taken into account, fission would set in at a time that is larger than the transient time  $\tau_f$ .

For describing the shape of  $\Gamma_f(t)$  we incorporated in the code the two approximations represented by equations (6.4) and (6.5) described in section 6.2 and the more sophisticated case given by equations (6.20), (6.8) and (6.9) of section 6.2.2. In all cases the stationary value of the fission width is

$$\Gamma_f^{K,n} = \Gamma_f^{BW,n} \cdot K \quad (\text{A4})$$

where  $\Gamma_f^{BW,n}$  is the fission width given by the transition-state model [BoW39] at the step  $n$  and  $K$  is the Kramers factor already introduced in equation (2.9) of section 2.3. Detailed formulations of the three cases are given below.

## A.1. Description of $\Gamma_f(t)$ by a step function

As shown in section 6.2, the fission width can be described by a step function that sets in to the stationary value given by equation (A4) at the transient time  $\tau_f$ . Let  $I_0$  be the number of nuclei available at the beginning of a certain step  $n$ . For the time interval  $t_{sum}^n < t < \tau_f$ , particle emission is the only deexcitation channel available and the number of nuclei that decay in that step  $n$  is

$$I_0 \cdot (1 - \exp(-(\tau_f - t_{sum}^n) / \tau_p^n)) \quad (\text{A5})$$

The upper index  $n$  indicates that these quantities differ from step to step. For  $t \geq \tau_f$ , fission is also possible, and the additional number of nuclei that decay by particle emission at the same step is

$$I_0 \cdot \exp(-(\tau_f - t_{sum}^n) / \tau_p^n) \cdot \frac{\Gamma_p^n}{\Gamma_p^n + \Gamma_f^{K,n}} \quad (\text{A6})$$

where the quantity  $I_0 \cdot \exp(-(\tau_f - t_{sum}^n) / \tau_p^n)$  represents the nuclei that survived particle emission before  $\tau_f$ . Similarly, the number of nuclei that fission after  $\tau_f$  is

$$I_0 \cdot \exp(-(\tau_f - t_{sum}^n) / \tau_p^n) \cdot \frac{\Gamma_f^{K,n}}{\Gamma_p^n + \Gamma_f^{K,n}} \quad (\text{A7})$$

The total probability for particle evaporation at a step  $n$  can be obtained by normalizing the total number of decays to the initial number of nuclei  $I_0$  leading to the expression

$$P_p^n = (1 - \exp(-(\tau_f - t_{sum}^n) / \tau_p^n)) + \exp(-(\tau_f - t_{sum}^n) / \tau_p^n) \cdot \frac{\Gamma_p^n}{\Gamma_p^n + \Gamma_f^{K,n}} \quad (\text{A8})$$

and the total probability for fission is

$$P_f^n = \exp(-(\tau_f - t_{sum}^n) / \tau_p^n) \cdot \frac{\Gamma_f^{K,n}}{\Gamma_p^n + \Gamma_f^{K,n}} \quad (\text{A9})$$

This formulation is similar but more consistent than the approach proposed previously in [RaM91] and [IgK95].

## A.2. Description of $\Gamma_f(t)$ by an exponential in-growth function

Another possibility to describe the time dependence of the fission width  $\Gamma_f(t)$  is an exponential in-growth function, equation (6.5) of section 6.2. In this case, the procedure is different than in the previous one because  $\Gamma_f(t)$  increases continuously with time.

The decay rate at a step  $n$  can be written as:

$$\left(\frac{dI}{dt}\right)_n = -\left[\frac{\Gamma_p^n}{\hbar} + \frac{\Gamma_f^n(t)}{\hbar}\right] \cdot I^n(t) = -\left[\frac{\Gamma_p^n}{\hbar} + \frac{\Gamma_f^{K,n}}{\hbar} (1 - \exp(-\frac{t+t_{sum}^n}{\tau}))\right] \cdot I^n(t) \quad (\text{A10})$$

By integrating equation (A10) we obtain an analytical expression for  $I^n(t)$

$$I^n(t) = I_0 \cdot \exp\left(-\frac{\Gamma_p^n + \Gamma_f^{K,n}}{\hbar} t\right) \cdot \left[ \exp\left(-\frac{\Gamma_f^{K,n} \cdot \tau}{\hbar} \cdot \exp(-\frac{t+t_{sum}^n}{\tau})\right) \right] \quad (\text{A11})$$

Substituting equation (A11) in (A10) we obtain an analytical expression for the decay rate  $(dI(t)/dt)_n$  of the nucleus that includes all possible particle decay channels and the already mentioned time dependence of  $\Gamma_f$ . After evaluating  $(dI(t)/dt)_n$  for the corresponding step, we sample from  $(dI(t)/dt)_n$  the decay time and finally calculate the value of  $\Gamma_f(t)$  at that decay time. The decay channel is then determined by a Monte-Carlo selection with the weights  $\Gamma_f(t)/\Gamma_{\text{total}}$  for fission and  $\Gamma_v/\Gamma_{\text{total}}$  for the emission of the particle  $v$ .

## A.3. Description of $\Gamma_f(t)$ by the analytical solution of the FPE for a parabolic nuclear potential

As shown by the dashed line in figure 6.2a) of section 6.2.1, the analytical solution of the FPE when the nuclear potential is approximated by a parabola gives a much more realistic description of the time dependence of the fission rate  $\lambda_f(t)$  than the step function and the exponential-like in-growth function. This analytical expression for the fission rate can be obtained by using equation (6.20) and taking  $W(x = x_b, t)$  from equations (6.8) and (6.9). Actually, the method [Tai00] we use to include this description of  $\Gamma_f(t)$  in the evaporation code is applicable for any function representing  $\Gamma_f(t)$ .

We first divide the time interval  $0 < t < 1.5 \cdot \tau_f$  (for  $t = 1.5 \cdot \tau_f$  the fission width has already reached its stationary value) in small subintervals of length  $L = 1.5 \cdot \tau_f / 50$ . If we are inside a certain step  $n$  of the deexcitation cascade, we define the value of the fission decay width as the quantity

$$\Gamma_{f,i}^n = \frac{\Gamma_f^n(t_{sum}^n + i \cdot L) + \Gamma_f^n(t_{sum}^n + (i+1) \cdot L)}{2} \quad (\text{A12})$$

with  $i = 0$  at the beginning of each step. This value of the fission decay width is used to evaluate the decay probability inside this small subinterval  $i$

$$P_{decay}^i = 1 - \exp\left(-\frac{L}{\tau^i}\right) \quad (\text{A13})$$

with

$$\frac{1}{\tau^i} = \frac{\Gamma_p^n}{\hbar} + \frac{\Gamma_{f,i}^n}{\hbar} \quad (\text{A14})$$

By means of a Monte-Carlo selection we establish whether the nucleus decays inside this time subinterval  $i$  or not. If no decay takes place, we evaluate again expression (A12) for the next subinterval  $i+1$  and so on, until the nucleus decays. The decay channel is then determined by a further Monte-Carlo selection with the weights  $\Gamma_p^n$  and  $\Gamma_{f,i}^n$ .

As shown by equations (6.8) and (6.9) of section 6.2.1, in this case we have an additional dependence of  $\Gamma_f(t)$  on the deformation at the fission barrier  $x_b$ , on the reduced mass  $\mu$  and on the frequency of the system at the ground state  $\omega_1$ . Considering that

$$\mu\omega_1^2 = 2K_1 \quad (\text{A15})$$

where  $K_1$  is the stiffness of the parabolic nuclear potential, the implementation of this description in the evaporation code requires determining the saddle point deformation  $x_b$  and the stiffness  $K_1$  of the different nuclei that are produced during the deexcitation cascade. For the saddle point deformation  $x_b$  we use the expression taken from [HaM88]

$$x_b = \frac{7}{3}y - \frac{938}{765}y^2 + 9.499768y^3 - 8.050944y^4 \quad (\text{A16})$$

where  $y = 1-\alpha$  and  $\alpha$  is the fissility parameter. For the stiffness  $K_1$ , we use the liquid-drop-model predictions of reference [MyS66]

$$K_1 = \left[ 7.1776 \left( 1 - 1.7826 \left( \frac{A-2Z}{A} \right)^2 \right) A^{2/3} - 0.1464 \frac{Z^2}{A^{1/3}} \right] \text{MeV} \quad (\text{A17})$$

Finally, we should remark that for the three descriptions considered, when calculating  $t_{sum}^n$ , we express the particle decay time and the fission decay time by the average decay times  $\tau_p$  and  $\tau_{fission}$  instead of sampling these quantities from a statistical decay-time distribution. In spite of this approximation, our treatment of the decay cascade is more realistic than previous formulations. For example, in reference [BaB93] several analytical expressions for the probabilities of the diverse decay channels are given considering the step function and the exponential in-growth function to describe the form of  $\Gamma_f(t)$ . However, this is done under the simplifying assumption that the total decay widths are unchanged from one step to the next in the decay cascade. In [BuH91] the exponential-like in-growth function is used, but the total decay time at each step of the cascade is considered to be ruled uniquely by the neutron-decay life time at that step, while the influence on the life time introduced by the other possible decay channels is not considered.

# Resumen

## 1. Motivación y objetivos

De acuerdo con el modelo de Bohr y Weehler [BoW39], el proceso de desexcitación de un núcleo pesado puede describirse desde un punto de vista puramente estadístico, donde la probabilidad de los diversos canales de desexcitación viene dada fundamentalmente por la densidad de niveles de energía existentes en el espacio de fases. Sin embargo el progreso de las técnicas experimentales ha permitido comprobar que este modelo es insuficiente. Esta discrepancia entre el modelo estadístico y los datos experimentales [GaB81, HiH81] viene dada porque la ocupación de los estados accesibles del espacio de fases y el consiguiente establecimiento del equilibrio termodinámico no ocurre espontáneamente como se asume en el modelo estadístico sino que conlleva un tiempo, es decir, el proceso de desexcitación de un núcleo pesado requiere una descripción dinámica. Debido a la gran cantidad de grados de libertad no existe por el momento ninguna teoría a nivel puramente microscópico que explique este proceso de desexcitación. Por esta razón, la mayoría de los modelos existentes son teorías de transporte [Wei80], es decir, teorías que tratan de describir el proceso de desexcitación usando un número reducido de variables. En estas teorías se hace una distinción entre grados de libertad colectivos o macroscópicos y grados de libertad intrínsecos o microscópicos, los últimos son tratados como un baño térmico. Esta idea nos recuerda a las teorías que describen el movimiento browniano de una partícula de polen en un fluido donde el grado de libertad colectivo es la posición o la velocidad de la partícula de polen y los movimientos de las moléculas del fluido constituyen los grados de libertad intrínsecos. En el núcleo, los grados de libertad intrínsecos son los estados individuales de los nucleones y los grados de libertad colectivos corresponden al movimiento coordinado del conjunto o de parte de los nucleones, a saber, vibraciones, rotaciones y todo tipo de deformaciones. La aplicación de las teorías de transporte al núcleo refleja una cuestión de auto consistencia ya que en este caso los grados de libertad colectivos están formados por los grados de libertad intrínsecos. Estos dos tipos de grados de libertad pueden interaccionar entre si intercambiando energía. El proceso por el cual se transfiere energía entre los grados de libertad intrínsecos y los grados de libertad colectivos se denomina disipación. La disipación está cuantificada por el coeficiente reducido de disipación  $\beta$  definido como

$$\frac{dE_{coll}}{dt} = \beta [E_{coll}^{eq} - E_{coll}] \quad (1.1)$$

donde  $E_{coll}$  es la energía media del grado de libertad colectivo a un tiempo  $t$  y  $E_{coll}^{eq}$  es la energía media del grado de libertad colectivo en el equilibrio térmico. Por tanto, la ecuación (1.1) implica que el coeficiente reducido de disipación mide la tasa relativa con la que varía la energía de un grado de libertad colectivo. En otras palabras, la disipación determina cuanto tiempo necesita un grado de libertad colectivo para alcanzar el equilibrio.

El proceso de fisión es el ejemplo más claro de movimiento colectivo a gran escala. Por esta razón, el proceso de fisión se presenta como un candidato ideal para estudiar la evolución dinámica de un grado de libertad colectivo y su interacción con el baño térmico que constituyen el conjunto de los nucleones. Durante las últimas tres décadas se han realizado numerosos estudios tanto experimentales como teóricos sobre el proceso de fisión para determinar el valor del coeficiente

reducido de disipación  $\beta$  y su dependencia con la temperatura y la deformación. Sin embargo este tema sigue siendo objeto de intensos debates. Existen un gran número de teorías de transporte que intentan determinar el coeficiente reducido de disipación. Algunas de las más relevantes son la teoría de transporte cuántica de Hofmann et al. [Hof97], la *Dissipative Diabatic Dynamics* (Dinámica Diabática Disipativa, DDD) de Nörenberg [Nör83] y la *Wall and window formula* (formula de la pared y la ventana) de Swiatecki et al. [BIB78]. La teoría de Hofmann establece que  $\beta$  aumenta con la temperatura siguiendo la expresión

$$\beta(T) \approx \frac{0.6 \cdot T^2}{1 + T^2/40} \quad (1.2)$$

donde  $T$  se mide en MeV y  $\beta$  en MeV/h. Esta misma teoría predice para  $^{234}\text{Th}$  una leve dependencia de  $\beta$  con la deformación. Por otro lado, la teoría DDD de Nörenberg aplicada a un gas de fermiones que interactúan [Nör81] predice que  $\beta$  es proporcional a  $1/T^2$  adoptando un valor de  $40 \cdot 10^{21} \text{s}^{-1}$  [HiR92] para  $T = 2.5$  MeV. Finalmente, según el más fenomenológico de los tres formalismos, la *wall and window formula*,  $\beta$  es independiente de la temperatura y aumenta con la deformación alcanzando valores máximos de  $\beta = 22 \cdot 10^{21} \text{s}^{-1}$ . Desde el punto de vista experimental la situación es igualmente complicada. En nuestra opinión, la divergencia entre las diversas técnicas experimentales tiene orígenes diversos. Por un lado, las técnicas experimentales usadas hasta ahora son limitadas y resulta difícil determinar observables sensibles a la magnitud de la disipación. Por otro lado, muchos observables han sido interpretados con modelos que no se ajustan a las condiciones experimentales y que contienen aproximaciones inapropiadas con el fin de acortar el tiempo de cálculo. Además, en ocasiones los resultados obtenidos por técnicas experimentales diferentes no son comparables.

Existe una relación entre los observables que se miden experimentalmente y la zona de deformación a la que son sensibles. Así por ejemplo, la energía cinética de los fragmentos de fisión nos informa de la disipación en la región en la que el núcleo está muy deformado, entre la barrera de fisión y el punto de escisión. La multiplicidad de las partículas emitidas es sensible a la disipación en todo el rango de deformaciones, desde el estado fundamental hasta el punto de escisión. Por el contrario, las secciones eficaces de fisión y de los residuos de evaporación están influenciadas por la disipación en la zona de pequeñas deformaciones entre el estado fundamental y la barrera de fisión. Recientes resultados experimentales parecen mostrar un cierto consenso en lo que respecta a la dependencia de  $\beta$  con la deformación. Estos resultados indican claros efectos del retraso dinámico inducido por la disipación en la zona de amplia deformación. Sin embargo en la zona donde el núcleo no está aún muy deformado no se han encontrado señales claras de disipación. Hay grupos que obtienen claros efectos con valores de  $\beta = 4 \cdot 10^{21} \text{s}^{-1}$  [ShD00] y  $\beta = 6 \cdot 10^{21} \text{s}^{-1}$  [DiS01], mientras otros grupos observan efectos muy débiles con [JiP01, LoG01] y finalmente otros trabajos [HuB00, Dio01] sostienen que sus medidas pueden ser interpretadas aplicando el modelo estadístico, contradiciendo así la existencia de disipación.

El objetivo de este trabajo es precisamente estudiar la disipación en el rango de pequeñas deformaciones. Nuestra contribución tiene varios aspectos. Por la parte experimental hemos aplicado un método muy apropiado para la investigación de la disipación. En este método la fisión es inducida a partir de colisiones periféricas con iones pesados a energías relativistas. La deformación del núcleo resultante tras la colisión es prácticamente la del estado fundamental y su momento angular es muy bajo ( $\Delta I < 20 \hbar$ ) [Jol97]. Estas condiciones son muy difíciles de conseguir

por los métodos experimentales más convencionales y representan importantes ventajas pues simplifican considerablemente la descripción teórica del proceso. Además, con este método se accede a energías de excitación muy altas lo cual permite observar los efectos de disipación en núcleos poco deformados, ya que a estas energías el tiempo de decaimiento por emisión de partículas predicho por el modelo estadístico es menor que el retraso dinámico inducido por la disipación. No obstante, es preciso tener en cuenta recientes resultados experimentales [Ric02, ScR02] los cuales indican que a temperaturas mayores que aproximadamente 5 MeV surgen inestabilidades térmicas que finalmente derivan en multifragmentación. Las consecuencias de este tipo de procesos se discutirán mas adelante. El montaje experimental usado, especialmente concebido para el estudio de reacciones de fisión en cinemática inversa, nos ha permitido introducir dos nuevos observables sensibles a la disipación en la región de deformaciones pequeñas. La interpretación de los observables en términos del coeficiente de disipación requiere el uso de modelos teóricos. Por esta razón, hemos hecho un intenso análisis de las aproximaciones más comúnmente usadas para reproducir los efectos de la disipación en el proceso de fisión. Dada la insuficiencia de estas aproximaciones, hemos desarrollado una descripción de estos efectos considerablemente más realista.

## 2. Experimento y resultados

Para poder estudiar reacciones de fragmentación se necesita un haz intenso de iones pesados a energías relativistas. Este tipo de haces existe en el GSI donde se aceleran iones de  $^{238}\text{U}$  hasta energías de 1 GeV por nucleón, permitiendo realizar estudios de reacciones nucleares en cinemática inversa. Después de ser acelerado, el haz de uranio fue conducido al montaje experimental donde se detectaron los fragmentos de fisión emitidos tras la interacción del haz con un blanco. Comparado con los experimentos en cinemática normal, la técnica de la cinemática inversa facilita considerablemente la detección y la identificación de los fragmentos de fisión, ya que los fragmentos de fisión están focalizados hacia delante y debido a su alta velocidad, su carga nuclear puede ser medida con gran precisión. Los instrumentos claves de nuestro montaje experimental eran dos cámaras de ionización situadas delante y detrás del blanco, y una cámara de ionización doble. Las dos cámaras permitieron seleccionar únicamente aquellos sucesos de fisión interesantes, que son los que tienen lugar en el blanco. A partir de la cámara de ionización doble se pudo determinar la carga nuclear de los dos fragmentos de fisión. Combinando la información dada por la cámara de ionización situada detrás del blanco y la información dada por la cámara de ionización doble, se obtuvo una eficiencia de aproximadamente un 97% para la detección de los sucesos de fisión. Con este montaje se determinaron las secciones eficaces totales de fisión  $\sigma_f$  de  $^{238}\text{U}$  a 1 GeV por nucleón en blancos de C,  $(\text{CH}_2)_n$ , Cu y Pb. Puesto que se cumple que

$$\sigma_f(\text{CH}_2) = \sigma_f(\text{C}) + 2\sigma_f(\text{H}) \quad (2.1)$$

nos fue posible deducir la sección eficaz total de fisión en hidrógeno. Esta sección eficaz es de gran importancia para el diseño de reactores híbridos [NiD01] y fuentes de neutrones [Bau01]. Como se observa en la tabla 2.1, los resultados concuerdan bien con los datos ya existentes para las mismas reacciones. Es más, en la mayor parte de los casos, la precisión de las secciones eficaces determinadas en este trabajo es mayor que la de los datos ya publicados.

En el caso de la reacción  $^{238}\text{U}$  (1 A GeV) +  $(\text{CH}_2)_n$  se determinaron dos nuevos observables: las secciones eficaces de fisión en función de la suma de las cargas de los fragmentos de fisión  $\sigma_f(Z_1+Z_2)$  y la anchura de las distribuciones de carga de los fragmentos de fisión. A las primeras las

denominaremos de ahora en adelante secciones eficaces parciales de fisión. Ambos observables son también sensibles a la disipación entre el estado fundamental y la barrera de fisión. Puesto que los fragmentos de fisión son ricos en neutrones y su energía de excitación no es muy alta, la probabilidad de que éstos emitan protones es muy baja. Por lo tanto, la suma de las cargas nucleares de los fragmentos de fisión  $Z_1+Z_2$  es prácticamente igual a la carga del núcleo que fisiona. A su vez, la carga del núcleo que fisiona representa una medida del parámetro de impacto de la colisión y por tanto de la energía de excitación inducida. Cuanto menor es la carga del núcleo que fisiona mayor es la energía de excitación inducida. A altas energías de excitación, es decir, para los valores de  $Z_1+Z_2$  más bajos, el retraso inducido por la disipación se hace perceptible y como consiguiente, es de esperar que las secciones eficaces parciales  $\sigma_f(Z_1+Z_2)$  sean menores que los valores que predice el modelo estadístico. Por otro lado, empíricamente [Rui97, MuS98] se ha establecido que existe una relación lineal entre la varianza de la distribución de carga  $\sigma_Z^2$  de los fragmentos de fisión y la temperatura del núcleo en la barrera de fisión. Por tanto si se estudia la varianza  $\sigma_Z^2$  en función de  $Z_1+Z_2$ , la existencia de una supresión de la fisión causada por la disipación implicaría que el núcleo evapora partículas antes de fisionar y, consiguientemente, para los valores más bajos de  $Z_1+Z_2$  la temperatura de fisión sería más baja que la temperatura de acuerdo con el modelo estadístico. En otras palabras, si existe la disipación, las varianzas de las distribuciones de carga asociadas con los valores más bajos de  $Z_1+Z_2$  serán menores que las varianzas que resultan del modelo estadístico.

Blanco	$\sigma_{fis}^{total}$ [b]	$\sigma_{fis}^{total}$ [b] otros resultados
H	$1.52 \pm 0.10$	$1.47 \pm 0.07$ [BoB78] $1.48 \pm 0.06$ [VaA81]
C	$1.30 \pm 0.03$	$1.13 \pm 0.08$ [RuB96]
$(CH_2)_n$	$4.35 \pm 0.10$	
Cu	$1.89 \pm 0.06$	$1.86 \pm 0.11$ [RuB96]
Pb	$3.84 \pm 0.14$	$3.75 \pm 0.38$ [PoB94]

**Tabla 2.1:** Secciones eficaces totales de fisión correspondientes a la reacción de  $^{238}\text{U}$  a 1 GeV por nucleón en distintos blancos. La primera columna refleja los resultados de este trabajo y la segunda los resultados de otras publicaciones.

Este nuevo método experimental permite producir núcleos pesados con deformaciones, momentos angulares y energías de excitación tales que permiten aplicar el modelo de Grangé y Weidenmüller [GrJ83] para describir el proceso de fisión. El modelo de Grangé y Weidenmüller está basado en la idea inicial de Kramers [Kra40] de considerar el proceso de fisión de forma análoga al movimiento browniano. Así, la fisión puede entenderse como la evolución de uno o varios grados de libertad colectivos de fisión en el baño térmico formado por el conjunto de los nucleones. Tal proceso está descrito por la ecuación de Fokker-Planck [Ris89] donde el coeficiente reducido de disipación  $\beta$  aparece como un parámetro.

Grangé y Weidenmüller [GrJ83] resolvieron numéricamente la ecuación de Fokker-Planck bajo unas condiciones iniciales que coinciden con las condiciones iniciales inducidas por nuestro método experimental. De sus cálculos resultó que el proceso de fisión está descrito por una anchura de fisión dependiente del tiempo  $\Gamma_f(t)$ . Es decir, que mientras que desde el punto de vista puramente estadístico de Bohr y Wheeler [BoW39] la anchura de fisión es constante en el tiempo, si se consideran los efectos introducidos por la disipación, la anchura de fisión está suprimida al inicio

del proceso, después de un tiempo aumenta y finalmente alcanza un valor estacionario que es menor que el valor constante que se obtiene de aplicar el modelo estadístico. La dependencia temporal de la anchura de fisión se describe normalmente a partir del tiempo de tránsito  $\tau_f$  que fue definido en [BhG86] como el tiempo necesario para que la anchura de fisión alcance 90% del valor asintótico.

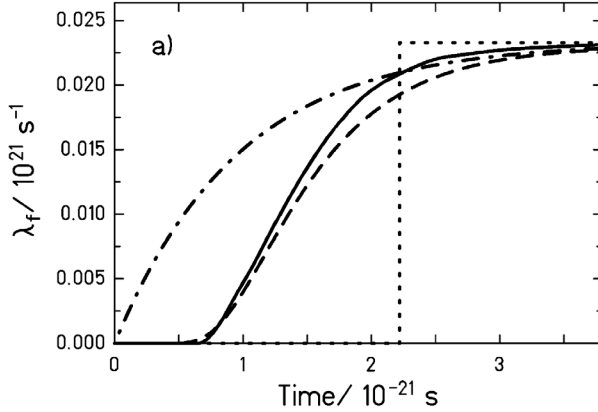


**Figura 2.1:** Tasa de fisión  $\lambda_f(t) = \Gamma_f(t)/\hbar$  en función del tiempo con  $\beta = 5 \cdot 10^{21} \text{ s}^{-1}$ ,  $T = 3 \text{ MeV}$  y  $A = 248$ . La línea continua representa el resultado de la solución numérica de la ecuación de Fokker-Planck tomada de la referencia [BhG86]. La línea a trazos es la aproximación introducida en este trabajo, obtenida a partir de la solución analítica de la ecuación de Fokker-Planck para un potencial nuclear parabólico [Cha43]. La línea a puntos corresponde a la función escalón y la línea a trazos y puntos a la función de crecimiento exponencial.

Tanto el valor estacionario como el tiempo de tránsito dependen de  $\beta$ . Por consiguiente, un modelo teórico fiable debe contener una descripción realista de la dependencia de la evolución temporal de la anchura de fisión. Sin embargo, no es fácil introducir estos efectos en los códigos teóricos usuales por lo cual en la mayoría de los casos se emplean aproximaciones para describir  $\Gamma_f(t)$ . Las dos más usadas son una función escalón que pasa a ser distinta de cero cuando se ha alcanzado el tiempo de tránsito  $\tau_f$  y una función basada en un crecimiento exponencial. Dada la crudeza de estas aproximaciones, hemos desarrollado una aproximación mucho más realista de  $\Gamma_f(t)$  basada en la solución analítica de la ecuación de Fokker-Planck para un potencial nuclear que se approxima con una parábola [Cha43]. La figura 2.1 muestra las diversas aproximaciones de la tasa de fisión  $\lambda_f(t) = \Gamma_f(t)/\hbar$  en comparación con la función que resulta de la solución numérica de la ecuación de Fokker-Planck [BhG86] representada por la línea continua. La línea a trazos es la aproximación introducida en este trabajo, la línea a puntos corresponde a la función escalón y la línea a trazos y puntos a la función de crecimiento exponencial. A parte de la reducción del valor asintótico de la anchura de fisión, el efecto más importante introducido por la disipación es la supresión inicial de la tasa de fisión  $\lambda_f(t) = \Gamma_f(t)/\hbar$ . Nuestra expresión analítica reproduce muy bien este efecto mientras que la función exponencial no reproduce dicha supresión y, es más, presenta una pendiente máxima para los tiempos pequeños. Por esta razón, creemos que esta aproximación no reproduce los efectos de la disipación adecuadamente.

La interpretación de los observables ha sido llevada a cabo mediante una versión actualizada del código ABRALBA [GaS91, JuJ98], un código Monte-Carlo basado en los modelos de abrasión y estadístico. Las tres aproximaciones de la evolución temporal de la anchura de fisión  $\Gamma_f(t)$

representadas en la figura 2.1 han sido implementadas en este código. Comparando los datos experimentales con las diversas descripciones hemos podido investigar hasta qué punto los resultados sobre disipación se ven afectados por las aproximaciones usadas para describir  $\Gamma_f(t)$ . El valor de  $\beta$  necesario para reproducir la sección eficaz total de fisión de la reacción  $^{238}\text{U}(1 \text{ A GeV}) + \text{Pb}$  depende fuertemente de la descripción que se use para  $\Gamma_f(t)$ . Mientras que la función escalón y la función basada en la solución analítica de la ecuación de Fokker-Planck requieren un valor de  $\beta = 2 \cdot 10^{21} \text{s}^{-1}$ , la función de tipo exponencial requiere un valor  $\beta = 4 \cdot 10^{21} \text{s}^{-1}$ .

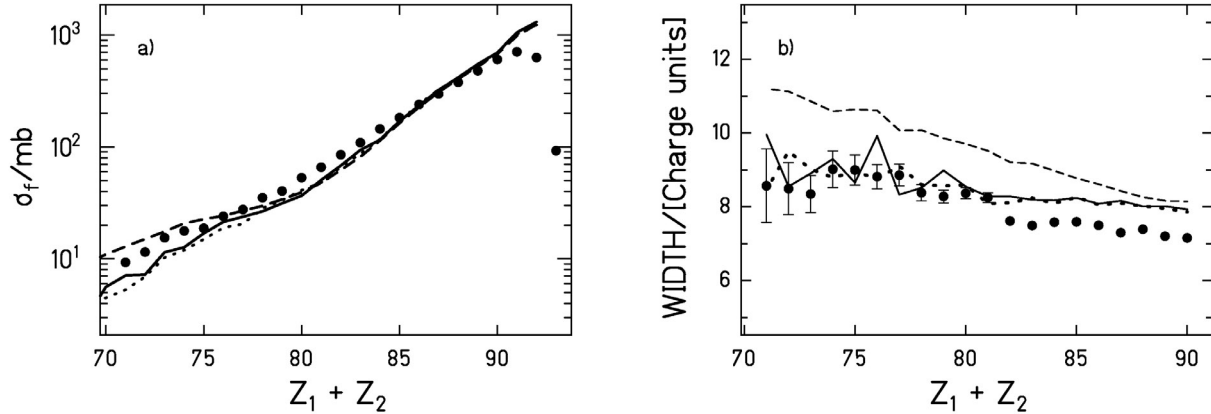


**Figura 2.2:** Secciones eficaces parciales de fisión (puntos negros parte a) y anchuras de las distribuciones de carga de los fragmentos de fisión (puntos negros parte b) correspondientes a la reacción  $^{238}\text{U} (1 \text{ A GeV}) + (\text{CH}_2)_n$  en función de la suma de las cargas nucleares de los dos fragmentos de fisión. Los datos experimentales se muestran en comparación con varios cálculos realizados con ABRALBA. Las líneas a trazos corresponden a cálculos realizados usando la aproximación de tipo exponencial y  $\beta = 4 \cdot 10^{21} \text{s}^{-1}$ . Las líneas a puntos corresponden a cálculos basados en la función escalón y  $\beta = 2 \cdot 10^{21} \text{s}^{-1}$  y las líneas continuas resultan de aplicar la aproximación dada por la solución analítica de la ecuación de Fokker-Planck y  $\beta = 2 \cdot 10^{21} \text{s}^{-1}$ .

Las secciones eficaces parciales de fisión y las anchuras de las distribuciones de carga se encuentran representadas en las figuras 2.2a) y 2.2b), respectivamente. Las líneas representan los resultados de diversos cálculos realizados aplicando las distintas aproximaciones para la función  $\Gamma_f(t)$ . La línea a trazos corresponde a la aproximación de tipo exponencial con  $\beta = 4 \cdot 10^{21} \text{s}^{-1}$ , la línea a puntos a la aproximación dada por la función escalón con  $\beta = 2 \cdot 10^{21} \text{s}^{-1}$  y la línea continua a la solución analítica de la ecuación de Fokker-Planck con  $\beta = 2 \cdot 10^{21} \text{s}^{-1}$ . La figura 2.2a) muestra que todas las descripciones reproducen igualmente bien las secciones eficaces parciales de fisión. En cambio, la figura 2.2b) muestra que la aproximación exponencial sobreestima las anchuras de las distribuciones de carga. La razón se debe a que esta aproximación implica que la fisión no se encuentra inhibida al inicio del proceso de desexcitación. Por tanto esta descripción sobreestima la temperatura con la que el núcleo fisiona y consecuentemente sobreestima también la anchura las distribuciones de carga. Este resultado confirma nuestra crítica inicial hacia esta aproximación.

Finalmente, para determinar la magnitud del coeficiente reducido de disipación  $\beta$  hemos comparado los dos nuevos observables con diversos cálculos realizados con ABRALBA para diferentes valores de  $\beta$ . Para ello hemos empleado la aproximación dada por la solución analítica de la ecuación de Fokker-Planck que hemos desarrollado en este trabajo. Los resultados están representados en la

figura 2.3. El modelo estadístico representado por la línea a trazos sobreestima claramente tanto las secciones eficaces parciales como las anchuras de las distribuciones de carga. Para describir estos nuevos observables es preciso incluir los efectos de la disipación. La mejor descripción de los datos experimentales se obtiene con  $\beta = 2 \cdot 10^{-21} \text{ s}^{-1}$ . Este valor de  $\beta$  corresponde a una anchura de fisión para la cual el tiempo necesario para adquirir el valor asintótico es mínimo. Es decir, que, en efecto, el grado de libertad colectivo experimenta una cierta disipación en su evolución hacia el equilibrio y por tanto necesita un cierto tiempo para poblar el espacio de fases. No obstante, el tiempo de tránsito correspondiente es el mínimo tiempo posible. En otras palabras, el grado de libertad colectivo experimenta un amortiguamiento crítico y no sobre amortiguado.

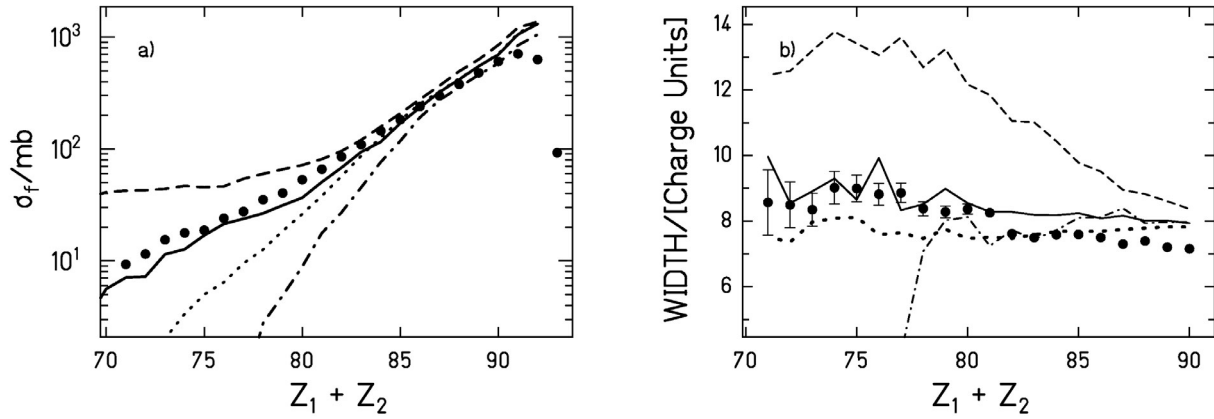


**Figura 2.3:** Secciones eficaces parciales de fisión (puntos negros parte a) y anchuras de las distribuciones de carga de los fragmentos de fisión (puntos negros parte b) correspondientes a la reacción  $^{238}\text{U}$  (1 A GeV) +  $(\text{CH}_2)_n$  en función de la suma de las cargas nucleares de los dos fragmentos de fisión. Los datos experimentales se muestran en comparación con varios cálculos realizados con ABRABLA. La línea a trazos ha sido obtenida aplicando el modelo estadístico sin incluir la disipación. El resto de los cálculos ha sido realizado aplicando la aproximación derivada de la solución analítica de la ecuación de Fokker-Planck. La línea continua ha sido calculada con  $\beta = 2 \cdot 10^{-21} \text{ s}^{-1}$ , la línea a puntos con  $\beta = 0.5 \cdot 10^{-21} \text{ s}^{-1}$  y la línea a trazos y puntos con  $\beta = 5 \cdot 10^{-21} \text{ s}^{-1}$ .

La relación entre el tiempo de tránsito  $\tau_f$  y  $\beta$  viene dada por la ecuación de Fokker-Planck [BhG86]. Al valor de  $\beta = 2 \cdot 10^{-21} \text{ s}^{-1}$  le corresponde una distribución de tiempos de tránsito cuyo valor medio es  $\tau_f \approx (1.7 \pm 0.4) \cdot 10^{-21} \text{ s}$ . Este resultado es compatible con otros trabajos [HuB00, MoJ95, JiP01, LoG01] sensibles al mismo rango de deformaciones. En nuestro análisis hemos asumido que  $\beta$  permanece constante con la temperatura. Es difícil establecer un juicio sobre la dependencia de  $\beta$  con la temperatura a partir de nuestros datos ya que el intervalo de temperaturas donde se puede investigar esta dependencia está limitado. Por un lado, de acuerdo con resultados experimentales recientes [Ric02, ScR02], existen indicaciones de que la energía máxima con la que un núcleo puede fisionar está limitada a un valor de unos 550 MeV. Pero además, nuestros observables son insensibles a los efectos del tiempo de tránsito para energías de excitación por debajo de 150 MeV y por encima de 350 MeV. Para energías de excitación por debajo de 150 MeV y siempre que  $\beta$  esté dentro de un rango determinado de valores, el tiempo de decaimiento estadístico es considerablemente mayor que el tiempo de tránsito inducido por la disipación. Para energías mayores que 350 MeV el amortiguamiento crítico es suficiente para inhibir completamente la fisión. Esto quiere decir que tanto si  $\beta$  aumenta como si decrece con la temperatura, el tiempo de

tránsito será mayor que en el caso del amortiguamiento crítico y lo único que se seguirá observando experimentalmente es la completa inhibición de la fisión para energías de excitación mayores que 350 MeV.

### 3. Conclusión

Hemos aplicado un método experimental muy adecuado para el estudio de la disipación en el rango de deformaciones pequeñas donde la fisión es inducida por colisiones periféricas con iones pesados a energías relativistas. A parte de medir la sección eficaz total de fisión del  $^{238}\text{U}$  a 1 GeV por nucleón en diversos blancos, hemos introducido dos nuevos observables sensibles a la magnitud de la disipación en este intervalo de deformación: las secciones eficaces parciales de fisión y las anchuras de las distribuciones de carga de los fragmentos de fisión.

Los datos experimentales han sido comparados con un código Monte-Carlo en el que hemos incluido diversas aproximaciones para la evolución temporal de la anchura de fisión. De la comparación con las secciones eficaces totales de fisión se deduce que los resultados dependen considerablemente de la aproximación que se use. El análisis de los dos nuevos observables muestra que una de las aproximaciones mas comúnmente usadas, expresada por un crecimiento de tipo exponencial, no reproduce bien los efectos de la disipación y por tanto no permite describir el conjunto de los observables de forma consistente. La aproximación que hemos introducido en este trabajo es mucho más realista que las aproximaciones que se han usado hasta ahora y permite una descripción muy satisfactoria de todos los observables. Asumiendo la validez de esta aproximación [JuS02], la comparación de los cálculos con los datos experimentales confirma la existencia de la disipación en núcleos poco deformados. No obstante, la disipación que se observa corresponde a un amortiguamiento crítico con  $\beta = 2 \cdot 10^{21} \text{s}^{-1}$ .

Los observables estudiados han sido descritos asumiendo que el coeficiente de disipación  $\beta$  no depende de la temperatura. No obstante, el estudio de la dependencia de  $\beta$  con la temperatura a partir de los observables que hemos presentado es posible sólo en el intervalo de energías de excitación por debajo de 350 MeV.

## Bibliography

- [AbR01] G. Abal, A. Romanelli, A. C. Sicardi-Schifino, R. Siri, and R. Donangelo, Nucl. Phys. A 683 (2001) 279
- [AIC01] V. P. Aleshin, M. Centelles, X. Vinas, and N. G. Nicolis, Nucl. Phys. A 679 (2001) 441
- [BaB93] B. Back, W. Bauer, and J. Harris, Proceedings of the 9th Winter Workshop on Nuclear Dynamics, Key West, Florida, USA, 30 January – 6 February 1993
- [Bad73] G. D. Badhwar, Nucl. Instr. Meth. 109 (1973) 119
- [Bau01] G. S. Bauer, Nucl. Instr. & Methods A 463 (2001) 505
- [BeA02] J. Benlliure, P. Armbruster, M. Bernas, A. Boudard, T. Enqvist, R. Legrain, S. Leray, F. Rejmund, K.-H. Schmidt, C. Stephan, L. Tassan-Got, and C. Volant, Nucl. Phys. A 700 (2002) 469
- [BeC89] C. J. Benesh, B. C. Cook, and J. P. Vary, Phys. Rev C 40 (1989) 1198
- [BeD00] C. A. Bertulani and D. S. Dolci, Nucl. Phys. A 674 (2000) 527
- [BhG86] K.-H. Bhatt, P. Grangé, and B. Hiller, Phys. Rev. C 33 (1986) 954
- [BIB78] J. Blocki, Y. Boneh, J. R. Nix, J. Randrup, M. Robel, A. J. Sierk, and W. J. Swiatecki, Ann. Phys. 113 (1978) 330
- [BoA98] B. Bouzid, M. Asghar, M. Djebara, and M. Medkour, J. Phys. G: Nucl. Part. Phys. 24 (1998) 1029-1037
- [BoB78] B. A. Bochagov, V. S. Bychenkov, V. D. Dmitriev, S. P. Maltsev, I. Obukhov, N. A. Perfilov, V. A. Udod, O. E. Shigaev, Yad. Fiz. 28 (1978) 572; (Sov. J. Nucl. Phys. 28 (1978) 291)
- [BoC02] A. Boudard, J. Cugnon, S. Leray, and C. Volant, submitted to Phys. Rev. C
- [BoS73] J. D. Bowman, W. J. Swiatecki and C. E. Tsang, Lawrence Berkeley Laboratory Report LBL-2908 (1973)
- [BoS92] D. Boilley, E. Suraud, Y. Abe, and S. Ayik, Proc. XXX Int. Winter Meeting on Nucl. Phys., Bormio, Ric. Sc. Ed Educ. Perm., suppl. No 91 (1992) 200
- [BoW39] N. Bohr and J. A. Wheeler, Phys. Rev. 56 (1939) 426
- [Bow98] C. D. Bowman, Ann. Rev. Nucl. Part. Sci. 48 (1998) 505
- [BrD72] M. Brack, J. Dagmar, A. S. Jensen, H. C. Pauli, V. M. Strutinsky, and C. Y. Wong, Rev. Mod. Phys. 44 (1972) 320
- [Bro94] Th. Brohm, PhD thesis, Technical University of Darmstadt, Germany, (1994)
- [BuH91] R. Butsch, D. J. Hofman, C. P. Montoya, P. Paul, and M. Thoennessen, Phys. Rev. C 44 (1991) 1515
- [CaS83] X. Campi and S. Stringari, Z. Phys. A. 309 (1983) 239
- [Cha43] S. Chandrasekhar, Rev. Mod. Phys. 15 (1943) 1

- [ChM88] R. J. Charity, N. A. McMahan, G. J. Wozniak, R. J. McDonald, L. G. Moretto, D. G. Sarantites, L. G. Sobotka, G. Guarino, A. Pantaleo, L. Fiore, A. Gobbi, and K. D. Hildenbrand, Nucl. Phys. A 483 (1988) 371
- [ChP01] G. Chaudhuri and S. Pal, Phys. Rev. C 63 (2001) 064603
- [ChP02] G. Chaudhuri and S. Pal, Phys. Rev. C 65 (2002) 054612
- [CuV97] J. Cugnon, C. Volant, and S. Vuillier, Nucl. Phys. A 620 (1997) 475
- [DaS76] K.T. R. Davies, A. J. Sierk, and J. R. Nix, Phys. Rev. C 13 (1976) 2385
- [Dio01] I. Diószegi, Phys. Rev. C 64 (2001) 019801
- [DiS01] I. Diószegi, N. P. Shaw, A. Bracco, F. Camera, S. Tettoni, M. Mattiuzzi, and P. Paul, Phys. Rev. C 63 (2001) 014611
- [EcK90] E-M. Eckert, A. Kühmichel, J. Pochodzalla, K. D. Hildenbrand, U. Lynen, W. F. J. Müller, H. J. Rabe, H. Sann, H. Stelzer, W. Trautmann, R. Trockel, R. Wada, A. Cerruti, P. Lhénoret, R. Lucas, C. Mazur, C. Ngô, M. Ribrag, E. Tomasi, A. Demeyer, and D. Guinet, Phys. Rev. Lett. 64 (1990) 2483
- [EmM96] D. O. Emerenko, B. Mellado, S. Yu. Platonov, O. V. Fotina, O. A. Yuminov, G. Giardina, G. F. Rappazzo, and F. Malaguti, Nucl. Part. Phys. 22 (1996) 1077
- [EnW01] T. Enqvist, W. Wlazlo, P. Armbruster, J. Benlliure, M. Bernas, A. Boudard, S. Czajkowski, R. Legrain, S. Leray, B. Mustapha, M. Pravikoff, F. Rejmund, K.-H. Schmidt, C. Stephan, J. Taieb, L. Tassan-Got, and C. Volant, Nucl. Phys. A 686 (2001) 481
- [Fel87] H. Feldmeier, GSI-87-14, Report, ISSN 0171-4546 (1987)
- [Fed87] H. Feldmeier, Rep. Prog. Phys. 50 (1987) 915
- [FGo93] P. Fröbrich and I. I. Gontchar, Nucl. Phys. A 563 (1993) 326
- [FrG93] P. Fröbrich, I. I. Gontchar, and N. D. Mavlitolov, Nucl. Phys. A 556 (1993) 281
- [GaB81] A. Gavron, J. R. Beene, R. L. Ferguson, F. E. Obenshain, F. Plasil, G. R. Young, G.A. Petitt, M. Jääskeläinen, D. G. Sarantites, and C. F. Maguire, Phys. Rev. Lett 47 (1981) 1255. Erratum: Phys. Rev. Lett. 48 (1982) 835
- [GaS91] J.-J. Gaimard and K.-H. Schmidt, Nucl. Phys. A 531 (1991) 709
- [GeA92] H. Geissel, P. Armbruster, K.-H. Behr, A. Bruenle, K. Burkard, M. Chen, H. Folger, B. Franczak, H. Keller, O. Klepper, B. Langenbeck, F. Nickel, E. Pfeng, M. Pfuetzner, E. Roeckl, K. Rykaczewsky, I. Schall, D. Schardt, C. Scheidenberger, K.-H. Schmidt, A. Schroeter, T. Schwab, K. Suemmerer, M. Weber, G. Muenzenberg, T. Brohm, H.-G. Clerc, M. Fauerbach, J.-J. Gaimard, A. Grawe, E. Hanelt, B. Knoedler, M. Steiner, B. Voss, J. Weckenmann, C. Ziegler, A. Magel, H. Wollnik, J.-P. Dufour, Y. Fujita, D. J. Vieira, and B. Sherrill, Nucl. Instrum. & Methods B70 (1992) 286
- [Gib75] W. M. Gibson, Annu. Rev. Nucl. Sci. 25 (1975) 465
- [GoB96] F. Goldenbaum, W. Bohne, J. Eades, T. v. Egidy, P. Figuera, H. Fuchs, J. Galin, Ye. S. Golubeva, K. Gulda, D. Hilscher, A. S. Iljinov, U. Jahnke, J. Jastrzebski, W. Kurcewicz, B. Lott, M. Morjean, G. Pausch, Peghaire, L. Pienkowski, D. Polster, S. Proschitski, B. Quednau, H. Rossner, S. Schmid, W. Schmid, and P. Ziem, Phys. Rev. Lett. 77 (1996) 1230

- [GoM99] F. Goldenbaum, M. Morjean, J. Galin, E. Lienard, B. Lott, A. Peghaire, Y. Perier, M. Chevallier, D. Dauvergne, R. Kirsch, J. C. Poizat, J. Remillieux, C. Cohen, A L'Hoir, G. Prevot, D. Schmaus, J. Dural, M. Toulemonde and D. Jacquet, Phys. Rev. Lett. 82 (1999) 5012
- [GoM02] I. Gontchar, M. Morjean, and S. Basnay, Europhys. Lett., 57 (2002) 355
- [GrC85] D. E. Greiner, H. Crawford, P. J. Lindstrom, J. M. Kidd, D. L. Olson, W. Schimmerling, and T. J. M. Symons, Phys. Rev. C 31 (1985) 416
- [GrJ83] P. Grangé, L. Jun-Qing, and H. A. Weidenmüller, Phys. Rev. C 27 (1983) 2063
- [Gro75] D. H. E. Gross, Nucl. Phys. A 240 (1975) 472
- [HaM88] R. W. Hasse and W. D. Myers, “Geometrical Relationships of Macroscopic Nuclear Physics” Springer-Verlag Berlin Heidelberg (1988) ISBN 3-540-17510-5
- [HeB96] M. Hesse, M. Bernas, P. Armbruster, T. Aumann, S. Czajkowski, Ph. Dessagne, C. Donzaud, H. Geissel, E. Hanelt, A. Heinz, C. Kozhuharov, Ch. Miehe, G. Muenzenberg, M. Pfuetzner, C. Roehl, K.-H. Schmidt, W. Schwab, C. Stephan, K. Sümerer, and L. Tassan-Got, Z. Phys. A 355 (1996) 69-75
- [HeS02] A. Heinz, K.-H. Schmidt, A. R. Junghans, P. Armbruster, J. Benlliure, C. Böckstiegel, H.-G. Clerc, A. Grewe, M. de Jong, J. Müller, M. Pfützner, S. Steinhäuser, B. Voss, submitted to Nucl. Phys. A
- [HiB99] D. J. Hinde, A. C. Berrian, M. Dasgupta, J. R. Leigh, J. C. Mein, C. R. Morton, and J. O. Newton, Phys. Rev. C 60 (1999) 054602
- [HiC84] D. J. Hinde, R. J. Charity, G. S. Foote, J. R. Leigh, J. O. Newton, S. Ogaza, and A. Chatterjee, Phys. Rev. Lett. 52 (1984) 986
- [HiG94] D. Hilscher, I. I. Gontchar, and H. Rossner, Yadernaya Fizika 57 (1994) 1255 (Physics of Atomic Nuclei 57 (1994) 1187)
- [HiH81] D. Hilscher, E. Holub, U. Jahnke, H. Orf, H. Rossner, Proc. of the 3rd Adriatic Europhysics Conference on the Dynamics of Heavy-Ion Collisions, Hvar, Croatia, Yugoslavia, May 25-30 (1981) 225
- [HiH92] D. J. Hinde, D. Hilscher, H. Rossner, B. Gebauer, M. Lehmann, and M. Wilpert, Phys. Rev. C45 (1992) 1229
- [HiR92] D. Hilscher and H. Rossner, Ann. Phys. Fr. 17 (1992) 471
- [HoB95] D. J. Hofman, B. B. Back, and P. Paul, Phys. Rev. C 51 (1995) 2597
- [Hof97] H. Hofmann Phys. Rep. 284 (1997) 137
- [Hof98] H. Hofmann, Proc. of the RIKEN Symposium on “Dynamics in Hot Nuclei”, Tokyo (1998)
- [HoH83] E. Holub, D. Hilscher, G. Ingold, U. Jahnke, H. Orf, and H. Rossner, Phys. Rev. C 28 (1983) 252
- [HoI94] P. Hofmann, A. S. Iljinov, Y. S. Kim, M. V. Mebel, H. Daniel, P. David, T. von Egidy, T. Haninger, F. J. Hartmann, J. Jastrebski, W. Kurzewicz, J. Lieb, H. Machner, H. S. Plendl, G. Riepe, B. Wright, and K. Ziock, Phys. Rev. C 49 (1994) 2555

- [**HoI01**] H. Hofmann, F. A. Ivanyuk, C. Rummel, and S. Yamaji, Phys. Rev. C 64 (2001) 054316-1
- [**Hub91**] J. C. Hubele, Ph. D. Thesis, University of Frankfurt, Germany (1991)
- [**HuB00**] S. K. Hui, C. R. Bhuinya, A. K. Ganguly, N. Madhavan, J. J. Das, P. Sugathan, D. O. Kataria, S. Murlithar, Lagy T. Baby, Vandana Tripathi, Akhil Jhingan, A. K. Sinha, P.V. Madhusudhana Rao, N. V. S. V. Prasad, A. M. Vinodkumar, R. Singh, M. Thoennessen, G. Gervais Phys. Rev. C 62 (2000) 054604, Comment: Phys. Rev. C 64 (2001) 019801, Reply: Phys. Rev. C 64 (2001) 019802
- [**IgI75**] A. V. Ignatyuk, M. G. Itkis, V. N. Okolovich, G. N. Smirenkin, and A. S. Tishin, Yad. Fiz. 21 (1975) 1185 (Sov. J. Nucl. Phys. 21 (1975) 612)
- [**IgK95**] A. V. Ignatyuk, G. A. Kudyaev, A. Junghans, M. de Jong, H.-G. Clerc, and K.-H. Schmidt, Nucl. Phys. A 593 (1995) 519
- [**JiP01**] K. X. Jing, L. Phair, L. G. Moretto, Th. Rubehn, L. Beaulieu, T. S. Fan, and G. J. Wozniak, Phys. Lett. B 518 (2001) 221
- [**JoI97**] M. de Jong, A. V. Ignatyuk, and K.-H. Schmidt, Nucl. Phys. A 613 (1997) 435
- [**JuJ98**] A. R. Junghans, M. de Jong, H.-G. Clerc, A. V. Ignatyuk, G. A. Kudyaev, and K.-H. Schmidt, Nucl. Phys. A 629 (1998) 635
- [**JuS02**] B. Jurado, K.-H. Schmidt, and J. Benlliure, submitted to Nucl. Phys. A
- [**KaA02**] A. V. Karpov, and G. D. Adeev, to be published
- [**KaN01**] A. V. Karpov, P. N. Nadtochy, D. V. Vanin, and G. D. Adeev, Phys. Rev. C 63 (2001) 054610
- [**Kar75**] P. J. Karol, Phys. Rev. C 11 (1975) 120
- [**KrF01**] H. J. Krappe and S. Fadeev, Nucl. Phys. A 690 (2001) 431
- [**KeK76**] A. K. Kerman and S. E. Koonin, Ann. Phys. 100 (1976) 332
- [**KiI96**] Y. S. Kim, A. S. Iljinov, M. V. Mebel, P. Hofmann, H. Daniel, T. von Egidy, T. Haninger, F. J. Hartmann, H. Machner, H. W. Plendl, G. Riepe, Phys. Rev. C 54 (1996) 2469
- [**Kra40**] H. A. Kramers, Physika VII 4 (1940) 284
- [**LoG01**] B. Lott, F. Goldenbaum, A. Böhm, W. Bohne, T. von Egidy, P. Figuera, J. Galin, D. Hilscher, U. Jahnke, J. Jastrzebski, M. Morjean, G. Pausch, A. Péghaire, L. Pienkowski, D. Polster, S. Proschitzki, B. Quednau, H. Rossner, S. Schmid, and W. Schmid, Phys. Rev. C 63 (2001) 034616
- [**MoJ95**] L. G. Moretto, K. X. Jing, R. Gatti, G. J. Wozniak, and R. P. Schmitt, Phys. Rev. Lett. 75 (1995) 4186
- [**Mor74**] L. G. Moretto, Proc. Of the third IAEA Symposium on the Physics and Chemistry of fission, Rochester, NY, 13-17 August 1973, IAEA Vienna (1974) , Vol. 1 p. 329
- [**Mül96**] J. Müller, Diploma Thesis, Technical University of Darmstadt, Germany (1996)
- [**MuS98**] S. I. Mulgin, K.-H. Schmidt, A. Grewe, and S. V. Zhdanov, Nucl. Phys. A 640 (1998) 375
- [**MyS66**] W. D. Myers and W. Swiatecki, Nucl. Phys. 81 (1966) 1

- [MyS74] W. D. Myers and W. J. Swiatecki, Ann. Phys. 84 (1974) 186
- [NiD01] H. Nifenecker, S. David, J. M. Loiseaux O. Meplan, Nucl. Instrum. Methods A 463 (2001) 428
- [NiS87] J. R. Nix and A. J. Sierk, Proc. Of the 6<sup>th</sup> Adriatic Conference in Nucl. Phys.: Frontiers of Heavy-Ion Physics, Dubrovnik, Yugoslavia (1987) ed. By N. Cindro et al., WorldScientific Singapore (1990) 333
- [Nör81] W. Nörenberg, Phys. Lett. 104 B (1981) 107
- [Nör83] W. Nörenberg, Nucl. Phys. A 409 (1983) 191c
- [PaT94] P. Paul and M. Thoennessen, Ann. Rev. Nucl. Part. Sci. 44 (1994) 65
- [PfG94] M. Pfuetzner, H. Geissel, G. Muenzenberg, F. Nickel, C. Scheidenberger, K.-H. Schmidt, K. Suemmerer, T. Brohm, B. Voss, and H. Bichsel, Nucl. Instr.& Methods B 86 (1994) 213
- [PIB95] H. van der Ploeg, J. C. S. Bacelar, I. Diószegi, G. van't Hof, and A. van der Woude, Phys. Rev. Lett. 75 (1995) 970
- [PoB94] S. Polikanov, W. Brüchle, H. Folger, E. Jäger, T. Krogulski, M. Schädel, E. Schimpf, G. Wirth, T. Aumann, J. V. Kratz, N. Stiel, and N. Trautmann, Z. Phys. A 350 (1994) 221
- [Pro01] A. V. Prokofiev, Nucl. Instr. & Methods A 463 (2001) 557
- [PoT00] J. Pochodzalla and W. Trautmann, preprint to appear in “Isospin Physics in Heavy-Ion Collisions at Intermediate Energies” Nova Science Publishers, Inc. (2000) <http://www.arxiv.org/abs/nucl-ex/0009016>
- [RaM91] E. M. Rastopchin, S. I. Mul'gin, Yu. B. Ostapenko, V. V. Pashkevich, M. I. Svirin, and G. N. Smirenkin, Yad. Fiz. 53 (1991) 1200 [Sov. J. Nucl. Phys. 53 (1991) 741]
- [ReH85] W. Reisdorf, F. P. Hessberger, K. D. Hildenbrand, S. Hofmann, G. Muenzenberg, K.-H. Schmidt, W. F. W. Schneider, K. Suemmerer, G. Wirth, J. V. Kratz, K. Schlitt, C.-C. Sahm, Nucl. Phys. A444 (1985) 154
- [ReI00] F. Rejmund, A. V. Ignatyuk, A. R. Junghans, and K.-H. Schmidt, Nucl. Phys. A 678 (2000) 215
- [Ric02] M. V. Ricciardi, Ph. D. Thesis, University of Frankfurt, Germany, in preparation
- [RiM98] D. Ridikas and W. Mittig, Nucl. Instrum. Methods A 418 (1998) 449
- [RiS80] P. Ring and P. Schuck, The Nuclear Many Body Problem, Springer, Berlin (1980)
- [Ris89] H. Risken, The Fokker-Planck Equation, Springer, Berlin (1989) ISBN 0-387-50498
- [RBa96] Th. Rubehn, R. Bassini, M. Begemann-Blaich, Th. Blaich, A. Ferrero, C. Gross, G. Imme, I. Iori, G. J. Kunde, W. D. Kunze, V. Lindenstruth, U. Lynen, T. Mohlenkamp, L. G. Moretto, W. F. J. Muller, B. Ocker, J. Pochodzalla, G. Raciti, S. Reito, H. Sann, A. Schuttauf, W. Seidel, V. Serfling, W. Trautmann, A. Trzcinski, G. Verde, A. Worner, E. Zude, and B. Zwieglinski, Phys. Rev. C 53 (1996) 993
- [RuB96] Th. Rubehn, R. Bassini, M. Begemann-Blaich, Th. Blaich, A. Ferrero, C. Groß, G. Immé, I. Iori, G. J. Kunde, W. D. Kunze, V. Lindenstruth, U. Lynen, T. Möhlenkamp, L. G. Moretto, W. F. J. Müller, B. Ocker, Pochodzalla, G. Raciti,

- S. Reito, H. Sann, A. Schüttauf, W. Seidel, V. Serfling, W. Trautmann, A. Trzcinski, G. Verde, A. Wörner, E. Zude, and B. Zwieginski, Phys. Rev. C 53 (1996) 3143
- [RuK98] V. A. Rubchenya, A. V. Kuznetsov, W. H. Trzaska, D. N. Vakhtin, A. A. Alexandrov, I. D. Alkhazov, J. Äystö, S. V. Khlebnikov, V. G. Lyapin, O. I. Osetrov, Yu. E. Penionzhkevich, Yu. V. Pyatkov, and G. P. Tiourin, Phys. Rev. C 58 (1998) 1587
- [RuI97] A.Ya. Rusanov, M. G. Itkis, and V. N. Okolovich, Yad. Fiz. 60 (1997) 773 (Phys. At. Nucl. 60 (1997) 683)
- [ScB93] K.-H. Schmidt, T. Brohm, H.-G. Clerc, M. Dornik, M. Fauerbach, H. Geissel, A. Grewe, E. Hanelt, A. Junghans, A. Magel, W. Morawek, G. Münzenberg, F. Nickel, M. Pfützner, C. Scheidenberger, K. Süümmerer, D. Vieira, B. Voss, and C. Ziegler, Phys. Lett. B 300 (1993) 313
- [ScB98] W. Schwab, M. Bernas, P. Armbruster, S. Czajkowski, Ph. Dessagne, C. Donzaud, H. Geissel, A. Heinz, C. Kozhuharov, C. Miehe, G. Muenzenberg, M. Pfuetzner, C. Stephan, K. Süümmerer, L. Tassan-Got, and B. Voss, Eur. Phys. J. A 2 (1998) 179
- [ScE97] W. Schmid, T. von Egidy, F. J. Hartmann, J. Hoffmann, S. Schmid, D. Hilscher, D. Polster, H. Rossner, A. S. Iljinov, M. V. Mebel, D. I. Ivanov, V. G. Nedorezov, A.S. Sudov, H. Machner, H. S. Plendl, J. Eades, and S. Neumaier, Phys. Rev. C 55 (1997) 2965
- [Sch77] G. Schütte, Z. Phys. A 283 (1977) 183
- [Sci99] Science Vol. 283, No. 5406 (1999) 1235
- [ScH84] W. U. Schröder and J. R. Huizenga, “Treatise on Heavy-Ion Science”, ed. D. A. Bromley, Vol. 2, Plenum Press New York and London (1984) 115
- [ScR02] K.-H. Schmidt, M. V. Ricciardi, A. Botvina, and T. Enqvist, Nucl. Phys. A 710 (2002) 157
- [ScS00] K.-H. Schmidt, S. Steinhaeuser, C. Boeckstiegel, A. Grewe, A. Heinz, A. R. Junghans, J. Benlliure, H.-G. Clerc, M. de Jong, J. Mueller, M. Pfuetzner, and B. Voss, Nucl. Phys. A 665 (2000) 221
- [Sha87] W. Q. Shen, J. Albinski, A. Gobbi, S. Gralla, K. D. Hildenbrand, N. Herrmann, J. Kuzminski, W. F. J. Müller, H. Stelzer, J. Tke, B. B. Back, S. Bjrnholm, and S. P. Srensen, Phys. Rev. C 36 (1987) 115
- [ShD00] N. P. Shaw, I. Diószegi, I. Mazumdar, A. Buda, C. R. Morton, J. Velkovska, J. R. Beene, D. W. Stracener, R. L. Varner, M. Thoennessen, and P. Paul, Phys. Rev. C 61 (2000) 044612
- [Sie86] A. J. Sierk, Phys. Rev. C 33 (1986) 2039
- [SoH98] G. A. Soulard, K. Hanold, W. Loveland, I. Lhenry, D. J. Morrissey, A. C. Veeck, and G. J. Wozniak, Phys. Rev. C 57 (1998) 3129
- [SüB00] K. Süümmerer and B. Blank, Phys. Rev. C, 61 (2000) 034607
- [SüR95] K. Süümmerer, J. Reinhold, M. Fauerbach, J. Friese, H. Geissel, H.-J. Körner, G. Münzenberg, R. Schneider, and K. Zeitelhack, Phys. Rev. C 52 (1995) 1106
- [Tai00] J. Taieb, Ph. D. Thesis, INP Orsay, France, (2000)
- [ThB93] M. Thoennessen and G. F. Bertsch, Phys. Rev. Lett. 71 (1993) 4303

- [ThC87] M. Thoennessen, D. R. Chakrabarty, M. G. Herman, R. Butsch, and P. Paul, Phys. Rev. Lett. 59 (1987) 2860
- [VaA81] L. A. Vaishnene, L. N. Andronenko, G. G. Kovshevny, A. A. Kotov, G. E. Solyakin, and W. Neubert, Z. Phys. A 302 (1981) 143
- [VaH73] R. Vandenbosch and J. R. Huizenga, Nuclear Fission, Academic Press, New York and London (1973) ISBN 0-12-710850-5
- [VaK99] D. V. Vanin, G. I. Kosenko, and G. D. Adeev, Phys. Rev. C 59 (1999) 2114
- [VeM99] J. Velkovska, C. R. Morton, R. L. McGrath, P. Chung, and I. Diószegi, Phys. Rev. C 59 (1999) 1506
- [Wei80] H. A. Weidenmüller, Progress in particle and Nuclear Physics, Pergamon, Oxford, Vol. 3 (1980) 49
- [WiS76] Wilkins and Steinberg, Phys. Rev. C 14 (1976) 1832
- [WiS96] J. Wilczynski, K. Siwek-Wilczynska, and H. W. Wilschut, Phys. Rev. C 54 (1996) 325



## Acknowledgements

This work relies on the help of several persons to whom I would like to express my gratitude in the following lines.

First of all, Dr. Karl-Heinz Schmidt, without whom this work would not have been possible. I thank him for the many things he taught me, for his enormous patience and for all the precious time he dedicated to me. He represents for me the genuine example of the scientist, guided by the curiosity and the will of understanding nature. I enjoyed very much his intuitive view of physics that he expressed with beautiful and original examples. In other words, he showed me that one can speak about physics “with the hands”.

I am as well indebted to Dr. José Benlliure. He established during my PhD the very important link to the University of Santiago de Compostela where this thesis was defended. The numerous and fruitful discussions with him have influenced this work in a decisive way.

Prof. Dr. Peter Armbruster, Dr. Dieter Hilscher, Dr. Laurent Tassan-Got and Dr. Aleksandra Kelic deserve also my gratitude for reading the first versions of this manuscript. Their remarks, questions and suggestions helped to improve significantly the quality of this work. I thank as well Dr. Fanny Rejmund, Dr. Timo Enqvist and the technicians of the Fragment Separator at GSI for their valuable contribution to the experimental part of this work.

I would also like to thank to M. Valentina Ricciardi, my friend, colleague and office mate for her support and for providing a team atmosphere in which I felt very comfortable. I say “*gracias*” as well to my friend Dániel for bringing me a piece of Andalucía to GSI. I would not have had the strength to accomplish this work without the encouragement of Medhi, who took care of me during the last months of this PhD.

Finally, I would like to thank to my parents for enabling me the possibility to study.

*“Oh, querido Pan y todos los otros dioses que aquí habitéis, concededme que llegue a ser bello por dentro, que todo lo que tengo por fuera se enlace en amistad con lo de dentro; y que considere rico al sabio... ¿Necesitamos alguna otra cosa Fredo? A mi me basta con lo que he pedido”.*

*Sócrates*